uOttawa

L'Université canadienne
Canada's university

FACULTÉ DES ÉTUDES SUPÉRIEURES ET POSTOCTORALES

uOttawa

L'Université canadienne
Canada's university

FACULTY OF GRADUATE AND POSDOCTORAL STUDIES

Roxana Ioana Flacau

AUTEUR DE LA THÈSE / AUTHOR OF THESIS

Ph.D. (Physics)

GRADE / DEGREE

Department of Physics

FACULTÉ, ÉCOLE, DÉPARTEMENT / FACULTY, SCHOOL, DEPARTMENT

Structural and Electron Density Changes in Dense Guest-host Systems: Analysis of X-ray Diffraction Data by the Rietveld and Maximum Entropy Methods

TITRE DE LA THÈSE / TITLE OF THESIS

Serge Desgreniers

DIRECTEUR (DIRECTRICE) DE LA THÈSE / THESIS SUPERVISOR

CO-DIRECTEUR (CO-DIRECTRICE) DE LA THÈSE / THESIS CO-SUPERVISOR

EXAMINATEURS (EXAMINATRICES) DE LA THÈSE / THESIS EXAMINERS

R. Hodgson

B. Torrie

P. Johns (absent)

Z. Stadnik

Gary W. Slater

Le Doyen de la Faculté des études supérieures et postdoctorales / Dean of the Faculty of Graduate and Postdoctoral Studies

Structural and Electron Density Changes in Dense Guest-Host Systems: Analysis of X-ray Diffraction Data by the Rietveld and Maximum Entropy Methods

By

Roxana Ioana Flacau

Thesis submitted to the Faculty of Graduate and Postdoctoral Studies
of the University of Ottawa in partial fulfillment
of the requirements for the degree of PhD. in Physics

Department of Physics
University of Ottawa
Canada

Your file Votre référence
ISBN: 978-0-494-34126-1
Our file Notre référence
ISBN: 978-0-494-34126-1

ABSTRACT

When studying the high-pressure structural behavior of crystalline materials, it is highly desirable to determine structural changes accurately, preferably at electron density levels. The Maximum Entropy Method (MEM) has already proven to be a very powerful tool for extracting the most probable charge density distributions directly from X-ray diffraction data.

This thesis presents high pressure X-ray diffraction studies on two distinct, but structurally similar, classes of guest-host materials: gas clathrate hydrates ($M_8(H_2O)_{46}$, with M= Kr, Xe) and silicon clathrate (Ba_8Si_{46}). In order to characterize the change of crystalline structure and electron distribution resulting from the increase of density due to the application of high pressure, we have used a recently developed approach wherein the classical Rietveld analysis is complemented iteratively with MEM calculations. It is found that charge density distributions derived from probability maps obtained by MEM provide further, in-depth insights into the structural changes induced by pressure in guest-host compounds.

Clathrate hydrates are inclusion compounds, in which guest atoms or molecules are trapped in cages formed by an ice-like host lattice of water molecules. In recent years, large deposits of methane hydrate (a clathrate hydrate) have been found on the oceanic floors, leading to a considerable interest in the physical properties of gas hydrates.

In the present study the crystalline structure I of xenon and krypton hydrates was investigated by powder X-ray diffraction at room temperature, over the pressure ranges for which these compounds are stable. Structure I, which has a cubic symmetry with *Pm3n* space group, is formed by two types of polyhedron, also referred to as small and large cages. The pressure dependence of the structural parameters was determined by applying a Rietveld analysis to the X-ray diffraction data. To further explore the effect of pressure on the guest atoms and the water molecule framework, we used the combined Rietveld/MEM method to derive the most probable charge density distributions at each pressure. Our results show that the charge density distribution of the encaged atoms

differs depending on the type of the host cage, small or large, at all pressures. Spherical density distributions were observed for the guest atoms in the small cages, while the atoms in the large cages showed longitudinal elongated electronic distributions. These findings are common to both Kr and Xe hydrates. Along with the observed cage deformations, this is a clear indication that the guest-host interaction differs significantly between the small and large cages at high pressures. A similar behavior has been previously reported in low-temperature studies of methane clathrate hydrate.

The combined Rietveld/MEM method was also successfully applied to explore the subtle changes in the electronic density distribution induced in Ba_8Si_{46} clathrate by the application of high pressure. This compound has been the object of extensive studies since its superconductivity has been discovered. Previous X-ray diffraction, near-edge X-ray absorption, and Raman spectroscopy studies have revealed two iso-structural phase transitions occurring at 5 and 17 GPa in Ba_8Si_{46}; their physical origin, however, was still not clearly understood. In our study, the most probable electron density distributions were calculated using the combined Rietveld/MEM method, with the goal to propose possible mechanisms for the two observed transitions. The examination of the electron density maps, and also electron density difference distributions, revealed that the low pressure transition is related to an enhanced charge transfer of Ba atoms to the Si framework, while the 17 GPa transition is a result of a sudden change in the electron density topology of the Si-Si bonds. As the pressure is increased, the electrons in the Si-Si bonds are displaced from the bonding region into the interstitial region, leading to a weakening of the Si-Si bonds, which explains the large volume reduction accompanying this transition.

Statement of Originality

Up to the present time, to the best of our knowledge, the study of dense Ba_8Si_{46} clathrate presented in this thesis is the first reported[1] successful attempt to detect and characterize pressure-induced structural phase transitions in dense materials by means of Rietveld/MEM analysis of X-ray diffraction data.

Also, no detailed experimental study of changes in structural parameters or electron distribution topology induced by pressure in dense sI clathrate hydrates has been reported in literature.

In addition, I am a co-author in another study[2], which is not presented in this thesis, reporting a new pressure-induced structural phase transition observed in CaH_2. My contribution to that study was to analyze the X-ray diffraction data by phase identification procedures and LeBail and Rietveld analysis.

[1] J. S. Tse, **R. Flacau**, S. Desgreniers, T. Iitaka, and J. Z. Jiang, accepted for publication *Physical Review B* (2007).

[2] J. S. Tse, D. D. Klug, S. Desgreniers, J. S. Smith, **R. Flacau**, Z. Liu, J. Hu, N. Chen and D. T. Jiang, *Physical Review B* **75**, 1 (2007).

Acknowledgements

In the first place I would especially like to thank my supervisors, Dr. Serge Desgreniers and Dr. John Tse, for their constant and invaluable guidance and help during my research work and writing my thesis. I was fortunate enough to work with this perfect combination of experimentalist and theoretician and their appeal for insight discussions and interpretation of the experimental data helped me move on and develop my skills as a researcher.

Former and actual colleges are acknowledged for the very pleasant working atmosphere. Special thanks to Jesse Smith for his friendship and advices.

I also want to thank to all the members of Physics Department for their instruction and help.

The financial support from the University of Ottawa is gratefully acknowledged.

Lots of thanks to my Romanian friends here in Ottawa who helped me on many occasions, for their support and encouragements.

I am grateful to my husband Catalin, who is always there for me, and my sweet daughter Ilinca for brighten my days and put up with long daycare hours.

This thesis is dedicated to my mother, Maria, and to the memory of my father, Nicolae.

Table of Contents

List of Figures

List of Tables

Introduction

Determining the structure of dense crystalline materials submitted to high compression represents a new frontier within the science of crystallography. It is considered essential for future development of condensed matter chemistry, physics, materials science, and biology under the extreme conditions, i.e., high pressure, combined with low and high temperatures [1-4]. A detailed structural characterization of crystalline phases should not be limited to finding the system symmetry and accurate atom positions in the unit cell, but should also extend to the determination of all the other topological properties of the associated charge density distribution. The Maximum Entropy Method (MEM) has proven to be a very powerful tool for extracting the most probable charge density distributions directly from X-ray diffraction data. The MEM was originally developed in the context of information and probability theory and. was introduced to address problems in crystallography by Collins in 1982 [5]. The first successful MEM analysis of X-ray diffraction data, carried out for the purpose of deriving accurate electron density distributions, was reported for the case of silicon by Sakata and Sato in 1990 [6]. Since then, numerous MEM studies of X-ray and neutron diffraction data have been carried out, revealing in-depth insights regarding the structural properties of various compounds: organo-metallic compounds [7-9], gas hydrates [10], transition metal oxides [11], and metals [12].

In this thesis, we present high pressure X-ray diffraction studies at room temperature on two distinct but similar classes of clathrate materials: gas clathrate hydrates [$M_8(H_2O)_{46}$, with M= Kr, Xe] and silicon clathrate (Ba_8Si_{46}). For a detailed characterization of the changes in the crystalline structures and electron distribution induced by pressure in these guest-host compounds, the combination of Rietveld and MEM analysis in a recently developed iterative method to reconstruct charge density distributions from X-ray diffraction data, the Rietveld/MEM [13] approach is used.

Gas hydrates form a special class of inclusion compounds in which hydrophobic guest atoms or molecules are trapped in ice-like, hydrogen-bonded, water molecule cages [14]. Those compounds, commonly found on Earth and in the outer Solar System, are

believed to play important roles in planetary processes [15]. In recent years, large accumulations of natural gas hydrates, e.g., methane hydrate, discovered in sediments on the oceanic floor and in arctic permafrost areas lead to an increasing interest in gas clathrate hydrates. On the one hand, the methane gas stored in these deposits may serve as an important future energy supply. On the other hand, uncontrolled release of methane from these deposits can significantly contribute to the greenhouse effect. This is also the case for another greenhouse gas, carbon dioxide, naturally forming a clathrate hydrate compound. For scientists, these guest-host compounds are especially interesting due to the fact that they are model systems suitable for the study of hydrophobic interactions, relevant for understanding of water-guest repulsive potentials relevant to biological problems (e.g., protein folding) [16].

Hydrates formed by natural gases were first reported by Sir Humphrey Davy in 1811, when he found that chlorine gas-water mixtures freeze more readily than pure water. In the 1950's von Stackelberg and co-workers identified two clathrate hydrate structures [17, 18], studied later in more detail by McMullan and Jeffrey [19, 20]. The clathrate hydrate crystal structures that were determined are two cubic structures, known as structure I and structure II. In 1987 the hexagonal clathrate structure H was discovered by Ripmeester and co-workers [21]. Its detailed crystallographic structure was determined only recently by a single diffraction study [22]. The three structure types differ in the number and geometry of cages in the unit cell.

Early on, most of the experimental investigations of crystalline structures and guest-host interactions focused on gas clathrate hydrates with relatively large guest molecules like ethylene oxide and tetrahydrofuran. There hydrates were easy to synthesize and large single crystals could be grown for experiments, however, the interpretation of the results was difficult due to the complicated geometry of the guest molecule. Rare gas clathrate hydrates are particularly suitable for the investigation of the guest-host interactions, due to the simplicity of the guest species; they are, however, more difficult to synthesize, especially in a single crystal form. That is why high-pressure X-ray and neutron diffraction, and Raman spectroscopy only recently clarified the pressure induced phase transformation sequence and pressure-temperature phase stability of Kr [23-26], Xe [23, 25-29], Ar [25, 29-32], Ne [25], and He [33, 34] hydrates. The

availability of high intensity X-ray beams from third generation synchrotron sources, allowing the investigation of microscopic samples, has been a crucial factor for the rapid progression of X-ray diffraction and inelastic X-ray scattering experiments carried out in a high pressure environment [35]. Those are important experimental techniques used for the study of structural and lattice dynamical properties of gas clathrate hydrates.

Structure I is a common phase for many gas clathrate hydrates, among which are Xe and Kr hydrates. The structural properties of this phase are well documented from low-temperature studies of methane hydrate [36, 37]; they will be further examined in this thesis. However, to our knowledge, no detailed studies of the changes in the structural parameters or electron density topology of structure I rare gas clathrate hydrates induced by pressure have been reported to date. Such study can significantly contribute to the understanding of repulsive interactions between the cage water molecules and guest atoms, and mechanisms leading to transition to a denser phase. Therefore, a central point of this thesis is to investigate the effect of pressure on the structural parameters and charge density distributions of sI Xe and Kr hydrates. For this purpose, high pressure powder X-ray diffraction experiments were carried out, at room temperature, using synchrotron radiation. The experimental data were analyzed in detail using the combined Rietveld/MEM method. Along with distortions in the geometry of cages, different thermal vibration behavior of the guest atoms, depending on their host lattice environment, are reported in dense sI gas clathrate hydrates for the first time.

Structures similar to those observed in gas clathrate hydrates are also adopted by other tetrahedrally-coordinated elements. In the presence of alkali metal atoms, group IV elements (Si, Ge, or Sn), form clathrates [38, 39]. Silicon clathrates were first synthesized by Cros *et. al.* in 1965 [40, 41]. These cage-type materials are formed by silicon fullerene-like polyhedra, which share their faces creating a three-dimensional Si-sp^3 covalent network. Cros *et. al.*'s report was followed by very few studies until the mid 1990's, when a growing interest in this class of materials was observed. The interest was motivated by the analogy with the fullerite-type compounds, which have a relatively high critical superconducting temperature. Presently, the renewed interest in the study of

group IV clathrates is driven by their potential applications as thermoelectrics [42, 43] and wide band gap semiconductor devices [44, 45].

The first report on the superconducting behavior of structure I Ba_8Si_{46} clathrate has motivated many studies of this compound and other related semiconductor clathrates [46-50]. X-ray diffraction studies [51, 52] of high-density Ba_8Si_{46} reported that a reversible iso-structural phase transition, characterized by a sudden reduction in the unit cell volume, occurs at 14-17 GPa. The change of the lattice parameter at the transition pressure is not accompanied by changes in the system symmetry or atom positions. This constitutes a very unusual phenomenon. Moreover, near-edge X-ray absorption [51] and Raman spectroscopy studies [53] have revealed an additional "transition" for Ba_8Si_{46} at about 5 GPa, undetected by the X-ray diffraction studies. The physical origin of the two "transitions", observed at 5 and 14-17 GPa, is still not clearly understood. In a study presented in this thesis, the most probable electron density distributions were extracted from the high pressure X-ray diffraction data using the combined Rietveld/MEM method, with the goal to propose possible mechanisms for those two transitions. As we expected, the systematic changes in the electron density distributions, as the pressure increased, are consistent with the previous experimental observations. This allowed us to report in the present work the first pressure-induced phase transition study based on the observation of charge density distributions derived by MEM from X-ray diffraction data.

This thesis is organized as follows: The theory of powder angular dispersive X-ray diffraction will be presented in Chapter I. The theoretical expressions, which are needed to analyze the X-ray diffraction experimental data, together with a description of the Rietveld analysis, will also be presented in Chapter I. In Chapter II, the Maximum Entropy Method, as used to reconstruct charge density distributions from X-ray diffraction data, will be introduced. Chapter III will focus on the description of the experimental setup of our high pressure X-ray diffraction experiments carried out using synchrotron radiation. Experimental results on Xe and Kr clathrate hydrates will be presented in Chapter IV. At first, the structural properties of the three most common phases of the gas clathrate hydrates will be introduced. Then, the sequence of phase transitions that Xe and Kr hydrates undergo with pressure will be shown and results from

the Rietveld refinement and MEM analysis will be reported and discussed. Chapter V will present results of a structural and dynamics study of dense Ba_8Si_{46} clathrate. First, results regarding the changes in the structural parameters induced by pressure, as obtained from the Rietveld analysis, will be shown. Then, changes in the electron density topology of dense Ba_8Si_{46}, calculated using Rietveld/MEM method will be presented and analyzed. The results from both gas clathrate hydrates and Si clathrate studies will be summarized and concluded in the "Summary and Outlook" section.

References

1. R. J. Hemley and N. W. Ashcroft, *Physics Today* **51**, 26 (1998).
2. R. M. Hazen, N. Boctor, J. A. Brandes, G. D. Cody, R. J. Hemley, A. Sharma, and H. S. Yoder Jr., *J. Phys.: Condens. Matter* **14,** 11489 (2002).
3. P. F. McMillan, *Nature Materials* **1**, 19 (2002).
4. R. J. Hemley and H. K. Mao, *Mineral. Mag.* **66**, 791 (2002).
5. C. J. Gilmore, *Acta Cryst. A* **52**, 561-589 (1996).
6. M. Sakata and M. Sato, *Acta Cryst.* **46**, 66 (1990).
7. H. Shimotani, T. Ito, Y. Iwasa, A. Taninaka, H. Shinohara, E. Nishibori, M. Takata, and M. Sakata, *J. Am. Chem. Soc.* **126**, 364 (2004).
8. E. Nishibori, I. Terauchi, M. Sakata, M. Takata, Y. Ito, T. Sugai, and H. Shinohara, *J. Phys. Chem.* **110**, 19215 (2006).
9. M. Takata, E. Nishibori, B. Umeda, M. Sakata, E. Yamamoto, and H. Shinohara, *Phys. Rev. Lett.* **78**, 3330 (1997).

10. A. Hoshikewa, N. Igawa, H. Yamauchi, and Y. Ishii, *J. Chem. Phys.* **125**, 034505 (2006).
11. K. Kato, M. Sakata, E. Nishibori, M. Takata, N. Hamada, and Y. Moritomo, *J. Phys. Soc. Jpn.* **74**, 2137 (2005).
12. B. B. Iversen, F. K. Larsen, M. Souhassou, and M. Takata, *Acta. Cryst. B* **51**, 580 (1995).
13. F. Izumi and T. Ikeda, Commission on Powder Diffraction, *IUCr Newslett.* **26**, 7 (2001).
14. E. D. Sloan, *Clathrate Hydrates of Natural Gases*, 2nd ed., Marcel Dekker, New York, 1998.
15. J. I. Lunine and D. J. Stevenson, *Icarus* **70**, 61 (1997).
16. M. M. Teeter, *Proc. Natl. Acad. Sci. U.S.A.* **81**, 6014 (1984).
17. M. v. Stackelberg and H. R. Muller, *Z. Electrochem.* **58**, 25 (1954).
18. M. v. Stackelberg and H. R. Muller, *Z. Electrochem.* **62**, 130 (1958).
19. R. K. McMullan and G. A. Jeffrey, *J. Chem. Phys.* **42**, 2725 (1965).
20. T. C. W. Mak and R. K. McMullan, *J. Chem. Phys.* **42**, 2732 (1965).
21. J. A. Ripmeester, J. S. Tse, C. I. Ratcliffe, and B. M. Powell, *Nature* **325**, 135 (1987).
22. J. S. Tse, V. P. Shpakov, V. R. Belosludov, F. Trouw, Y. P. Handa, and W. Press, Europhys. Lett. **54**, 354 (2001).
23. S. Desgreniers, R. Flacau, D. D. Klug, and J. S. Tse, *CeSMEC* (March 24-28, Florida, 2003).
24. S. Sasaki, S. Hori, T. Kume, and H. Shimizu, *J. Phys. Chem. B* **110**, 9838 (2006).
25. S. Alavi, J. A. Ripmeester, D. D. Klug, *J Chem Phys.* **125**, 104501 (2006).
26. K. Sugahara, T. Sugahara, and K. Ohgaki, *J. Chem. Eng. Data* **50**, 274 (2005).

27. C. Sanloup, H. K. Mao, and R. J. Hemley, *Proc. Natl. Acad. Sci. U.S.A.* **99**, 25 (2002).

28. K. Ohgaki, T. Sugahara, M. Suzuki, H. Jindai, *Fluid Phase Equilibria* **175**, 1 (2000).

29. J. S. Loveday, R. J. Nelmes, D. D. Klug, J. S. Tse, and S. Desgreniers, *Can. J. Phys* **81**, 539 (2003).

30. Y. A. Dyadin, E. G. Larionov, A. Yu. Manakov, F. V. Zhurko, *Mend. Comm.* **393**, 209 (1999).

31. A. Yu. Manakov, V. I. Voronin, A. V. Kurnosov, A. E. Teplykh, V. Yu. Komarov, and Y. A. Dyadin, *J. Incl. Phenom.* **48**, 11 (2004).

32. A. G. Ogienko, A. V. Kurnosov, A. Yu. Manakov, E. G. Larionov, A. I. Ancharov, M. A. Sheromov, M. A. Sheromov, A. N. Nesterov, *J. Phys. Chem. B* **110**, 2840 (2006).

33. S. L. Dong, A. I. Kolesnikov, J. C. Li, *Physica B: Condensed Matter* **263**, 429 (1999).

34. G. G. Malenkov, E. A. Zheligovskaya, *J. Incl. Phenom.* **48**, 45 (2004).

35. R. J. Hemley, H. K. Mao, and V. V. Struzhkin, *J. Synch. Rad.* **12**, 135 (2005).

36. C. Gutt, B. Asmussen, W. Press, M. R. Johnson, Y. P. Handa, and J. S. Tse, *J. Chem. Phys.* **113**, 4713 (2000).

37. A. Hoshikawa, H. Igawa, H. Yamauchi, Y. Ishii, *J. Chem. Phys.* **125**, 034505 (2006).

38. A. San-Miguel and P. Toulemonde, *High Pressure Research* **25**, 159 (2005).

39. E. Reny, S. Yamanaka, C. Cros, and M. Pouchard, *Chem. Commun.* **2000**, 2505 (2000).

40. J. S. Kasper, P. Hagenmüller, M. Pouchard, and C. Cros, *Science* **150**, 1713 (1965).

41. C. Cros, M. Pouchard, and P. Hagenmüller, *C. R. Acad. Sci* **260**, 4764 (1965).

42. J. L. Cohn, G.S. Nolas, V. Fessatidis, T.H. Metcalf, and G.A. Slack, *Phys. Rev. Lett.* **82**, 779 (1995).

43. J. S. Tse, K. Uehara, R. Rousseau, A. Ker, C. I. Ratcliffe, M. A. White and G. MacKay *Phys. Rev Lett.* **85**, 114 (2000).

44. J. Gryko, P. F. McMillan, R. F. Marzke, G. K. Ramachandran, D. Patton, S. K. Deb, and O.F. Sankey, *Phys. Rev.* B **62**, 7707 (2000).

45. D. Connetable, V. Timoshevskii, E. Artacho, and X. Blase, *Phys. Rev. Lett.* **87**, 206405 (2001).

46. H. Kawaji, H. Horie, S. Yamanaka, and M. Ishikawa, *Phys. Rev. Lett.* **74**, 1427 (1995).

47. K. Tanigaki, T. Shimizu, K.M. Itoh, J. Teraoka, Y. Moritomo, and S. Yamanaka *Nature Materials,* **2**, 653 (2003).

48. A. San Miguel, P. Kéghélian, X. Blase, P. Mélinon, A. Perez, J. P. Itié, A. Polian, E. Reny, C. Cros, and M. Pouchard *Phys. Rev. Lett.* **83**, 5290 (1999).

49. J.S. Tse, S. Desgreniers, Z.Q. Li, M.R. Ferguson, and Y. Kawazoe, *Phys. Rev. Lett.* **89**, 195507 (2002).

50. T. Kume, T. Koda, S. Sasaki, H. Shimizu, and J.S. Tse, *Phys. Rev.* B **70**, 052101 (2004).

51. A. San Miguel, A. Merlen, P. Toulemonde, T. Kume, S. Le Floch, A. Aouizerat, S. Paskarelli, G. Aquilanti, O. Mathon, T. Le Bihan, J.P. Itié, S. Yamanaka, *Europhys. Lett.* **69**, 556 (2005).

52. L. Yang, Y. M. Ma, T. Iitaka, J. S. Tse, K. Stahl, Y. Ohishi, Y. Wang, R. W. Zhang, J.F. Liu, H. K. Mao and J. Z. Jiang, *Phys. Rev. B* **74**, 245209 (2006).

53. T. Kume, H, Fukuoka, T. Koda, S. Sasaki, H. Shimizu, and S. Yamanaka., *Phys. Rev. Lett.* **90**, 155503 (2003).

CHAPTER I

Angular Dispersive Powder X-ray Diffraction

In this chapter, aspects of powder X-ray diffraction theory, relevant for the analysis and understanding of our X-ray diffraction experimental data will be presented. Also, a description of the Rietveld method, used in our structure refinement analyses and applied to powder X-ray diffraction data, will be given.

1.1 Introduction

Powder X-ray diffraction is a very powerful and widely used analytical technique for materials identification and crystal structure determination. A single crystal X-ray diffraction pattern is a collection of diffraction spots, each spot corresponding to a fulfilled Bragg diffraction condition. X-ray diffraction recorded from an ideal powder gives rise in space to a cone of diffraction every time Bragg's law (eq 1.1) is satisfied, due to the completely random orientations of the numerous crystallites ($\sim 10^6$ crystallites/cm^2) [1] in a powder sample (provided the incident beam of X-rays is monochromatic). Even though single crystal diffraction is the most appropriate method in structural analysis, powder diffraction is often times used due to the limitations associated with the former method. Here are examples for which the use of single crystal X-ray diffraction is less practical. Often times the accessibility of good quality and sizeable single crystals is limited (as in the case, for instance, of a material in a high-density phase obtained by the application of high pressure). Moreover, it is difficult to detect a multi-phase sample using single crystal diffraction.

The principal problem associated with powder X-ray diffraction lies in the reduced information content of the X-ray diffraction pattern caused by accidental and systematic peak overlap. Basically, powder diffractometry projects the three-dimensional reciprocal lattice into one-dimensional space. Such a projection causes partial or total

overlap of peaks from similar or identical lattice spacings. As a consequence, only a subset of all observable reflections have uniquely determined intensities, leading to a loss of structural information. This sometimes makes the task of structure determination and refinement by powder X-ray diffraction difficult. To some extent, this intrinsic problem has been overcome by the use of advanced X-ray synchrotron sources combined with whole pattern analysis methods (e.g., Rietveld refinement and LeBail extraction procedures). The use of synchrotron radiation can provide much better resolved X-ray diffraction patterns than conventional sources.

1.2 Scattering of X-rays by Crystals

X-rays, being electromagnetic waves, are susceptible to diffraction. Having wavelengths similar to the interatomic distances in crystals, they interact with atoms (more precisely, with their electrons) forming crystal lattice, in the same way that light interacts with a conventional diffraction grating.

The main features of an X-ray diffraction pattern are peak positions and peak intensity and shape. Bragg's law (1.1) gives the necessary condition for diffraction (peak position) but provides no information regarding peak intensity and possible peak extinctions due to the unit cell symmetry (crystallographic space group *appartenance*).

An arrangement of atoms (crystal) of periodicity d gives rise to constructive interference of the scattered radiation having a wavelength λ when Bragg's law is satisfied:

$$n\lambda = 2d\sin(\theta), \tag{1.1}$$

where n is an integer (order of diffraction) and θ is the incident angle of the incoming X-ray beam with respect to the plane of scattering.

The calculated intensity for an arbitrary point i of the diffraction pattern is a superposition of the background (mostly Compton scattering) and Bragg peaks, according to the following formula [2]:

$$y_{ci} = s\sum_{K} L_K |F_K|^2 \phi(2\theta_i - 2\theta_K) P_K A + y_{bi}, \quad (1.2)$$

where s is a scale factor,

K represents the (hkl) set of Miller indices for a given Bragg reflection,

L_K expresses the Lorentz, polarization, and multiplicity factors,

ϕ is the reflection profile function,

P_K is the preferred orientation factor,

A is an X-ray absorption factor arising from the sample,

F_K is the structure factor for the K-th Bragg reflection,

y_{bi} is the background intensity at the i point.

In the following sections, each factor in the diffraction intensity equation (1.2) will be described in detail.

1.2.1 Structure Factor

Among all the factors contained in the X-ray scattering intensity equation (1.2), the structure factor is the one bearing most of the structural information of the sample. This factor expresses the combined (total) scattering of X-rays for all atoms in the unit cell compared to that of a single electron [2]:

$$F_K = \sum_j g_j f_j(d) t_j(d) e^{|2\pi i(hx_j + ky_j + lz_j)|}, \quad (1.3)$$

where the summation is done over each j atom at the position (x_j, y_j, z_j) in the unit cell and

d is the d-spacing, defined as $d = \dfrac{\lambda}{2\sin\theta_K}$,

g_j is the site occupation factor for atom j,

t_j is the temperature factor for atom j,

f_j is the atomic scattering factor for atom j.

In general, the structure factor is a complex quantity and its amplitude $|F_K|$ is measured in electrons.

1.2.1.1 Temperature Factor (Debye-Waller Factor)

The temperature factor is a measure of the oscillating motion of atoms about their equilibrium positions. It is defined as:

$$t_j = \exp\left(-B_j \frac{\sin^2\theta}{\lambda^2}\right), \tag{1.4}$$

where B_j is the thermal displacement parameter of the j[th] atom:

$$B_j = 8\pi\left(\overline{u^2}\right)_j, \tag{1.5}$$

u being the deviation from the equilibrium position.

1.2.1.2 Atomic Scattering Factor

The atomic scattering factor for a given atom, f, is defined as the ratio of the total radiation amplitude scattered by an atom in a given direction to the amplitude scattered by a single electron in the same direction. Thus, it depends on the electronic charge distribution in the atom, direction of scattering, and incident wavelength used.

f has its maximum value, Z (atomic number), along the direction of the incident beam and is rapidly decreasing with the increase of $\frac{\sin\theta_K}{\lambda}$ (Fig 1.1).[3]

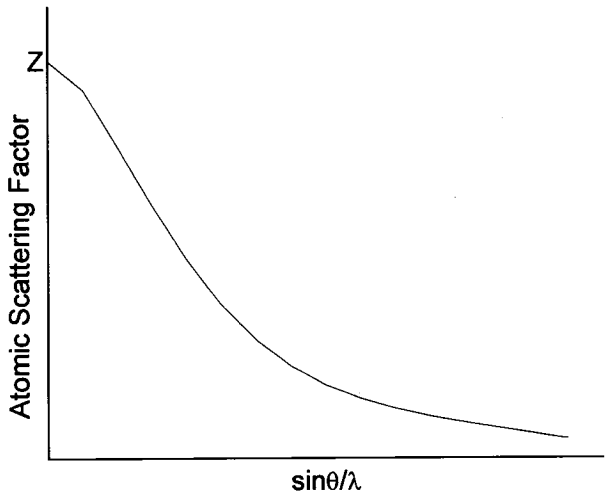

Figure 1.1. Atomic scattering factor as a function of $\frac{\sin\theta_K}{\lambda}$.

As described in equation (1.4) and Figure 1.1, both the atomic scattering factor and the Debye-Waller factor decrease dramatically with $\frac{\sin\theta_K}{\lambda}$, leading to a significant decrease in the structure factor and hence X-ray diffraction intensity at low d-spacings.

1.2.2 Peak Profile Functions

The powder X-ray diffraction peak profile is influenced by three categories of factors [2]:

a.) sample contributions:

1. intrinsic profile (Darwin profile) which is the result of uncertainty principle (location of the photon in a crystal is restricted to a rather small volume, so $\Delta p = \frac{h}{\Delta\lambda}$, so $\Delta\lambda$ must be finite and so finite width of the peak
2. crystallite size: as crystallite diameter, τ, decreases below 1μm the integral breadth of the peak (width of a rectangle having the same area and

height as the diffraction peak), β, increases according to $\beta = \frac{\lambda}{\tau \cos\theta}$ (this contribution can be modeled by a Lorentzian function)

3. microstrain: $\beta = \varepsilon \tan\theta$, where ε is microstrain parameter. (modeled by a Gaussian function)

b.) spectral distribution of incident radiation. This factor has been greatly limited by the use of the highly monochromatic synchrotron radiation.

c.) instrumental contributions that can be divided in two classes, depending on which type of broadening they are inducing :

1.) symmetric broadening

i. X-ray detector

ii. receiving slits

iii. monochomator

2.) asymmetric broadening.

In the case of our X-ray diffraction experiments, the most significant instrumental contribution in the symmetric broadening of the diffraction peaks is due to the limited spatial resolution introduced by the X-ray detector. No receiving slits were used in our experiments and the double-crystal monochromator induces far less line broadening than does the X-ray detector. Typically, for good quality samples, we measure a full-width-at-half-maximum (FWHM) of the diffraction peaks of about 0.06°. This is a sufficiently good peak resolution, considering the inherent broadening of the X-ray diffraction lines rising from a sample subject to non-ambient conditions like high pressure, as presented in this work.

The instrumental contributions to asymmetric broadening (due to axial divergence of the incident beam, specimen transparency, and flat specimen) are significantly improved with the use of highly parallel synchrotron radiation beam and the transmission geometry, as opposed to the Bragg-Brentano geometry.

The various contributions to the Bragg reflections' profile, presented above, introduce a fundamental problem: the X-ray diffraction peaks are well represented by neither the Gaussian, $G(\theta_i)$ nor Lorentzian, $L(\theta_i)$, profile functions. Therefore, other

profile functions, which are analytical convolutions of Gaussian and Lorentzian profiles, are commonly used as peak profile functions. Among them, Pearson VII and pseudo-Voigt are the most common ones.

Pearson VII, $P(\theta_i)$, is a symmetric function that reduces to a Lorentzian when m =1 and tends to a Gaussian for $m \to \infty$:

$$P(\theta_i) = L(\theta_i)^m, \tag{1.6}$$

where m is the Pearson VII index.

The pseudo-Voigt function is defined as:

$$V = \eta L + (1-\eta)G. \tag{1.7}$$

The mixing parameter, η, can be expressed as a linear function of $2\theta_i$ with refinable coefficients. Different variations of the Pearson VII and pseudo-Voigt functions were developed in order to account for the asymmetric contributions in the peak profile function. The function which describes in the most accurate way the profile of the X-ray diffraction lines measured in our experiments is the pseudo-Voigt function, and, consequently, it has been used in all our data analyses.

The full-width-at-half-maximum (FWHM) of the diffraction peaks, H, is usually modeled using the Caglioti formula:

$$H^2 = U\tan^2\theta + V\tan\theta + W, \tag{1.8}$$

where W, V, and U are refinable parameters.

1.2.3 Polarization Factor

The amplitude of the scattered wave depends on the angle between the polarization plane of the incident beam and plane of scattering. The polarization factor accounts for this dependence, which leads to an increase of the scattered intensity at low angles. In general, the polarization factor has the following expression:

$$P = P_0(1 - p\alpha), \tag{1.9}$$

where p is the degree of polarization of the incident X-ray beam,

P_0 is the polarization factor for a completely unpolarized beam,

α is a geometrical term.

P_0 and α are defined as follows:

$$P_0 = \frac{1+\cos^2(2\theta)}{2}; \tag{1.10}$$

$$\alpha = \frac{\sin^2(2\theta)}{1+\cos^2(2\theta)}. \tag{1.11}$$

Synchrotron radiation is highly polarized; the degree of polarization used for corrections of our X-ray diffraction data was 0.99.

1.2.4 Lorentz Factor

The Lorentz correction takes into account the fact that different reflections satisfy the diffraction condition for different periods of time, during the measuring process. The expression for the Lorentz factor depends on the geometry of diffraction. For the transmission geometry, used in all our X-ray diffraction experiments, the Lorentz correction was $\frac{1}{\sin 2\theta}$.

1.2.5 X-ray Absorption Factor

When X-rays pass through a material of thickness x, their intensity, I, is decreased due to absorption and scattering. The absorption component is accounted by the attenuation law:

$$I = I_0 e^{-\mu x}, \tag{1.12}$$

μ is called linear absorption coefficient and has the dimension of inverse distance and I_0 is the X-ray beam intensity before entering the material.

If absorption is not taken into account, diffraction from different parts of the sample should give the same contribution to the Debye diffraction ring. However, as it can be seen in Figure 1.2, different contributing regions correspond to different paths of incident and diffracted rays and consequently an absorption correction should be applied to the measured diffraction pattern. In the illustrated example, the attenuation of ray ***1*** is greater than for ray ***2***, since its path is longer.

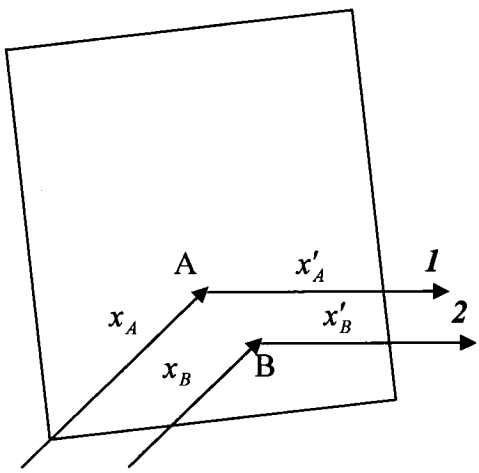

Figure 1.2. X-ray scattering by different regions of the sample.

This correction becomes important especially if the coefficient of absorption, which depends on the material and the incident wavelength, is high. With the use of the tunable synchrotron radiation, this problem can be minimized by conducting the experiment in a wavelength region away from the absorption edges of the material.

Also, high absorption results in a strong background due to fluorescence making, again, the capability of choosing a proper incident wavelength very important. All factors that have to be taken into consideration when choosing the wavelength of the X-ray beam for a certain diffraction experiment will be presented in Chapter II. A detail description of synchrotron radiation characteristics, relevant for our high pressure powder X-ray diffraction experiments, will also be given in Chapter II.

1.2.6 Multiplicity Factor

The multiplicity is the number of different planes with the same spacing in the unit cell forming a particular (hkl) family. For example, for cubic symmetry, the (100), (010), (001), (-100), (0-10), and (00-1) planes are all equivalent. Consequently, only one of those planes is represented (generally (100)), with multiplicity factor 6. As the symmetry of the unit cell decreases so does the multiplicity factor. As an example, in case of the tetragonal symmetry, the multiplicity factor for the (100) plane is 4. In a tetragonal crystal the (100) plane is equivalent with the (010), (-100), and (0-10) planes, but not with the (001) and (00-1) ones.

1.2.7 Preferred Orientation

Starting from fundamental principles of diffraction on polycrystalline samples, the ideal sample consists of crystals oriented completely at random. In this case, the diffraction pattern is independent on the orientation of sample relative to the incident X-ray beam. In actual samples, however, there is almost always some degree of preferred orientation of crystallites and thus the measured intensities of X-ray diffracted rays are affected. As a consequence, some diffraction peaks can completely disappear and the intensity of other lines can be very misleading. Preferred orientation can be easily recognized (from non-uniform intensity along the diffraction rings) if a diffraction image is recorded on an area detector which allows a clear visualization and inspection of the Debye diffraction rings; the same information about this phenomenon is completely hidden in the case of standard diffractometer recordings.

Various functions have been developed to correct the preferred orientation contribution to the diffraction patterns; they are implemented in all quantitative phase analysis and Rietveld refinement software. For the case of our data reported in this thesis, no preferred orientation corrections were necessary.

1.2.8 Background

In a powder X-ray diffraction experiment, background can arise from different sources. Those include:

- Incoherent (Compton) scattering
- Fluorescence radiation emitted by the sample
- Diffraction scattering from amorphous domains in the sample
- Diffraction scattering from materials other than the specimen, including sample mount, and air.

In most X-ray diffraction data analysis programs, background is usually modeled by a high order polynomial function. A 12-order polynomial function was used to refine the X-ray diffraction data presented in this study. In the case of most our datasets, a baseline subtraction was performed before the background refinement.

1.3 The Rietveld Method

The Rietveld analysis is a unique and valuable method for extracting detailed structural information from X-ray and neutron diffraction powder data. This method was devised as a complete powder diffraction pattern technique, which makes use of the full information contained in the pattern and not just the resolved peaks as it was traditionally done. The method was introduced by Hugo M. Rietveld in 1967 [4]. It is a whole pattern fitting structure refinement method where the least squares (χ^2-minimization) procedure is carried out until the best fit between the entire observed diffraction pattern and calculated one (based on equation 1.2) is reached. The function to be minimized is:

$$S_y = \sum_i w_i (y_i - y_{ci})^2 , \qquad (1.13)$$

where $w_i = 1/y_i$,

y_i is the observed intensity at point i in the pattern,

y_{ci} is the calculated intensity.

The weight of the pattern at step i, w_i, is used in calculations to ensure that all peaks, including those with very small intensities, give significant contributions during the refinement procedure.

This method is not an actual structure determination method, but rather a structure parameter refinement procedure. A sufficiently accurate starting model is thus required.

The possible variables in this χ^2-minimization analysis of powder X-ray diffraction data can be classified as the following:

1. peak position parameters (unit cell parameters, the zero point, wavelength, group symmetry);
2. peak shape parameters;
3. parameters depending on the peak area (atom coordinates, occupancies, anisotropic displacements, absorption, and extinction).

A typical Rietveld refinement plot is shown in Figure 1.3. In the upper field the observed (dotted line) and calculated (solid line) patterns are shown. The vertical bars indicate the positions of the Bragg reflections and the difference between the observed and calculated pattern is shown in the lower field.

The criteria by which the quality of refinement is assessed are expressed by several residuals (also known as the R-factors), such as:

R-structure factor: $$R_F = \frac{\sum \left| (I_K('obs'))^{1/2} - (I_K(calc))^{1/2} \right|}{\sum (I_K('obs'))^{1/2}}, \tag{1.14}$$

R-intensity factor: $$R_I = \frac{\sum \left| I_K('obs') - I_K(calc) \right|}{\sum I_K('obs')}, \tag{1.15}$$

R-pattern: $$R_p = \frac{\sum \left| y_i(obs) - y_i(calc) \right|}{\sum y_i(obs)}, \tag{1.16}$$

R-weighted pattern: $$R_{wp} = \left\{ \frac{\sum w_i \left(y_i(obs) - y_i(calc) \right)^2}{\sum w_i \left(y_i(obs) \right)^2} \right\}^{1/2}, \tag{1.17}$$

where I_K is the intensity of the Kth Bragg reflection and y_i is the intensity at a point i in the diffraction pattern.

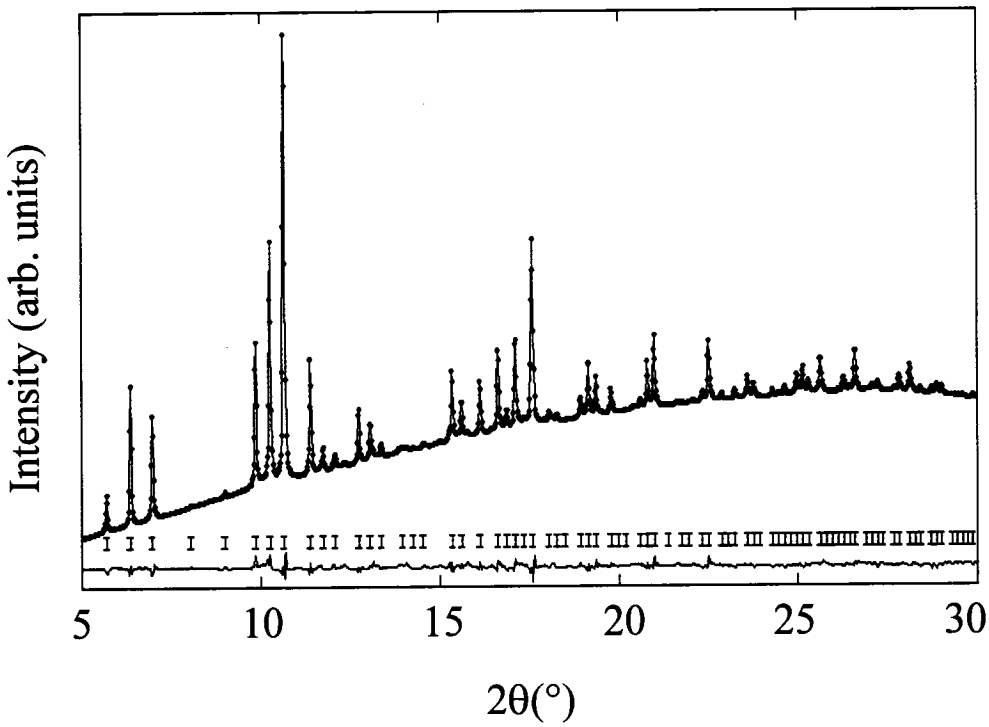

Figure 1.3. An example of a whole-pattern (Rietveld) refinement result: observed and calculated X-ray diffraction pattern of Ba_8Si_{46} clathrate. The dot symbols denote the experimental data; the solid line, the calculated pattern; tick marks the calculated peak positions; the bottom curve represents the difference between observed and calculated patterns.

From the mathematical point of view, R_{wp} is the most meaningful factor because the numerator is the residual quantity to be minimized. R_F and R_I are biased by the structural model used in the refinement because one cannot extract the absolute values for peak intensities, they are deducted based on the model (hence, writing them in quotation marks in Equation 1.14 and 1.15). Nevertheless, these two R factors can be very useful in some analysis (i.e. multiphase refinement) since they only account for misfits in the intensity of the Bragg's peaks.

The R-values are very important and useful indicators during the refinement process for the evaluation of a successful refinement. In addition, it is also important to use graphical criteria of fit (i.e. plots of the observed and calculated patterns) as a guide

during the refinement (see Figure 1.3). Graphics are used for a global view of the process and easy identification of gross errors, such as wrong values of starting lattice parameters, incorrect profile function or even space group.

References

1 J. I. Langford and D. Louër, *Rep. Prog. Phys.* **59** (1996).

2 R. A. Young, *The Rietveld Method* (International Union of Crystallography, Oxford University Press, 1995).

3 B. E. Warren, *X-Ray Diffraction* (Addison-Wesley Publishing Company, 1969).

4 H. M. Rietveld, *Acta Crystallogr.* **22**, 151 (1967).

CHAPTER II
Mapping Charge Density Distributions from X-ray Diffraction Data

Important information regarding the electronic structure and properties of crystalline phases can be extracted from the charge density distribution in the unit cell. In the present chapter, details on how charge density distributions can be reconstructed from X-ray diffraction data by means of Fourier analysis and the Maximum Entropy Method will be presented.

2.1 Electron Density Equation and Charge Density Fourier Mapping

In Chapter I, we have seen that the knowledge of the crystal structure enables structure factors and scattering intensities to be implicitly calculated. Now the inverse problem is considered: can one obtain the electronic density distribution in the unit cell if the structure factors are known? We will address this question by introducing the method of Fourier analysis as applied to crystallographic data.

The structure factor equation (1.3) was written under the approximation that the unit cell consists of atoms which are not interacting with each other. In other words, the unit cell content was regarded as individual atoms situated at lattice points, each atom having a scattering power given by the appropriate atomic scattering factor. Another way of looking at the unit cell content is to consider atoms as providing a continuous distribution of electron density at point $\boldsymbol{r}$, $\rho(r)$. In doing so, the expression for the structure factor (1.3) can be rewritten in terms of electron density, [1]:

$$F_K = \int_{\substack{unit \\ cell}} \rho(r) e^{\left|2\pi i(hx_j+ky_j+lz_j)\right|} dV\,, \tag{2.1}$$

V being the volume of the unit cell.

From equation (2.1), it becomes clear that the charge density function is the Fourier transform of the structure factor. Keeping in mind that the structure factor is a discrete function at reciprocal lattice points and that each F_K is associated with a volume $1/V$, this leads to the electron density equation valid in any point (x, y, z) in the unit cell:

$$\rho(x,y,z) = \frac{1}{V}\sum_K F_K \exp[-2\pi i(hx+ky+lz)]$$

or $$\rho(x,y,z) = \frac{1}{V}\sum_K [A_K \cos(2\pi(hx+ky+lz) + iB_K \sin(2\pi(hx+ky+lz)], \qquad (2.2)$$

with A_K and B_K denoting the real and imaginary components of F_K.

Electron density maps are usually computed at points on a three dimensional grid. From the interpolated peaks of the density distribution, the positions of the atomic centers can be found and hence the crystal structure can be deduced. The resolution of the density map is limited by the fact that only a finite number of diffraction peaks (and consequently structure factors) are accessible, for experimental reasons and limitations, and the electron density function calculated by means of equation (2.2) will be affected by series termination errors. Besides the resolution problem, the use of Fourier transformation to find electronic density distributions has another important inherent flaw. Equation (2.2) is a summation of trigonometric functions, and therefore a finite number of terms in the summation will always result in negative values in some regions of the electronic density map; negative values have no physical meaning. As can be seen in Figure 2.1, in the case of a Fourier transform, a peak in the charge density function is surrounded by oscillations of gradually decreasing amplitude arising only from the mathematical problem of limited number of terms in the summation [2]. That is why Fourier analysis can be useful for determining the atomic positions but cannot give meaningful information about the actual chemical bonding between the atoms. The problems in obtaining an accurate charge density map can be overcome to a good extent by using a different mathematical

approach, namely, the Maximum Entropy Method. The principles and analysis details of this method will be detailed in the next sections.

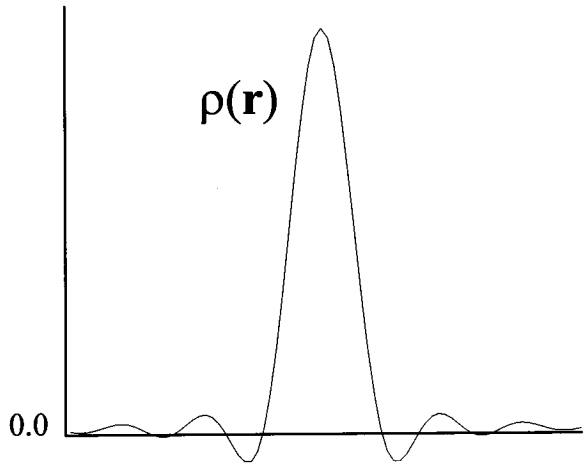

Figure 2.1. Electron density distribution obtained by Fourier mapping, affected by series termination errors.

2.2 Maximum Entropy Method

The Maximum Entropy Method (MEM) was first developed in the context of information and probability theory and was originally designed to enhance the information contained in noisy data in the field of radioastronomy [2]. Here it is considered for the reconstruction of electron density distribution starting from X-ray diffraction data.

2.2.1 Introduction to the Maximum Entropy Principle

In general, if a discrete probability distribution with a known set of N normalized probabilities $\{p_1, p_2, ...p_N\}$ is given, its entropy, S, or information content, I, is defined as:

$$S = -I = -\sum_{j=1}^{N} p_j \ln p_j \,. \tag{2.3}$$

If prior information, contained in the normalized set of probabilities $\{q_j\}$, is to be considered in the problem then according to Jaynes' expression of the information entropy [3]:

$$S = -\sum p_j \ln\left(\frac{p_j}{q_j}\right). \tag{2.4}$$

The maximum entropy principle states that the most probable distribution, given a set of constraints, is the one that maximizes the entropy of the system.

2.2.2 MEM as Applied to Charge Density Distributions Calculations

The Maximum Entropy Method was first introduced in crystallography by Collins in 1982 and it has been used since then especially to deduce the most probable charge density distribution consistent with the observed structure factors [3].

2.2.2.1 Previous Work

The first application of the MEM in a charge density study was performed on Si [4] and provided detailed structural information including bonding characteristics between atoms. Subsequently, it has been applied to a wide variety of materials and revealed important aspects of the nature of electronic structures from the viewpoint of charge density. Successful applications include calculation of electron density distribution of organo-metallic compounds [5, 6, 7], gas hydrates [8], transition metal

oxides [9] and metals [10], and studies of structural changes under high pressure [11, 12, 13]. Some intrinsic problems of MEM have also been emphasized. It has been shown that the incompleteness in the dataset of structure factors in the low angle region leads to non-physical features in the charge density distribution [14]. Also, if an insufficiently high number of structure factors is included in the MEM analysis, the fine details of the charge density distribution are distorted [14, 15].

2.2.2.2 Procedure

For the purpose of calculating the most probable charge density distribution consistent with the observed structure factors, the unit cell is divided into N pixels of equal size and the normalized electron density, ρ_i, at each i pixel is considered as a discrete probability distribution of independent events. Under these considerations, the entropy expression becomes:

$$S = -\sum_{i=1}^{N} \rho_i \ln\left(\frac{\rho_i}{\tau_i}\right), \tag{2.5}$$

where τ_i is the normalized density at i^{th} pixel derived from prior information (usually set to a uniform distribution at the beginning of analysis)

ρ_i is the normalized density, defined as:

$$\rho_i = \frac{\rho_i^*}{\sum_{i=1}^{N} \rho_i^*}, \tag{2.6}$$

with ρ_i^* being the actual charge density at pixel i.

S is maximized subject to the following three constraints:

$$\rho_i > 0 \tag{2.7}$$

$$C_F = \sum_{j=1}^{M_F} \frac{\left|F_c(K_j) - F_o(K_j)\right|^2}{\sigma_j^2} = M_F \tag{2.8}$$

$$C_N = \sum_{i=1}^{N} \rho_i = 1, \tag{2.9}$$

where M_F is the number of resolved reflections observed,

$F_c(K_j)$ and $F_o(K_j)$ are the calculated and the observed structure factors for reflection K_j, respectively,

σ_j is the estimated standard deviation of the observed structure factor.

C_F is usually referred to as "F-constraints".

Information about overlapping reflections in the powder X-ray diffraction pattern can also be introduced in the MEM analysis by using the so-called G-constraints:

$$C_G = \sum_{j=1}^{M_G} \frac{\left|G_{cj} - G_{oj}\right|^2}{\sigma_j^2} = M_G, \tag{2.10}$$

with $G_{cj}^2 = \dfrac{\sum_{i=1}^{L_j} m_i \left|F_c(K_i)\right|^2}{\sum_{i=1}^{L_j} m_i}$.

M_G is the total number of groups of overlapped reflections,

G_{oj} is the sum of the integrated intensities of overlapped reflections in group j,

L_j is the number of overlapped reflections in group j,

m_i is the multiplicity of the ith reflection.

In the "F" and "G" constraints expressions, the unknown, ρ, is contained in the structure factor expression, according to equation (2.1).

This mathematical optimization problem of seeking the extrema of a function f, subject to k constraints, g_k, is solved by using the Lagrangian multipliers method. In general, the method reduces to a problem in n variables and k constraints to a solvable problem of $(n+k)$ variables with no constraints. This method introduces a new and unknown scalar variable for each constraint, called the Lagrange multiplier. A new unconstrained function, F, which is a linear combination of the functions f and g_k having the multipliers as coefficients, is defined. The extrema of F coincides with the extrema of f, subject to constraints.

For our problem, we will define λ as the Lagrangian multiplier for "F" and "G" constraints and μ the multiplier for the normalization constraint, C_N. Consequently we will introduce a new function, Q, and find its maximum:

$$Q = S - \frac{\lambda}{2}\left(\frac{C_F + C_G}{M_F + M_G} - 1\right) - \mu(C_N - 1). \tag{2.11}$$

Q can be maximized by setting its partial derivatives with respect to ρ_i , λ and μ to zero:

$$\frac{\partial Q}{\partial \rho_i} = 0,$$

$$\frac{\partial Q}{\partial \lambda} = 0,$$

$$\frac{\partial Q}{\partial \mu} = 0.$$

The solution of this system will be:

$$\rho_i = \frac{\tau_i}{A}\exp\left(-\lambda\frac{\partial C}{\partial \rho_i}\right), \tag{2.12}$$

with $A = \sum_{i=1}^{N} \tau_i \exp\left(-\lambda\frac{\partial C}{\partial \rho_i}\right)$ and $C = \frac{C_F + C_G}{2(M_F + M_G)}$ [15].

Equation (2.12) cannot be solved analytically. Numerical methods, zero-th order single-pixel approximation and nonlinear single pixel-approximation, are used in the current available MEM software.

To summarize, in principle, the only information needed to obtain reliable charge density probability distribution results are the observed structure factors extracted from a high quality diffraction pattern and the volume of the unit cell.

The details of how the MEM theory is implemented in the software packages that we used will be presented in the following section.

2.2.3 MEM/Rietveld Analysis and MEM-based Pattern Fitting Method

For the purpose of finding charge density distributions, the observed structure factors are estimated from the experimental powder X-ray diffraction data using the Rietveld analysis implemented in a software called RIETAN-2000 [17]. These structure factors are then used as input in a MEM analysis program, PRIMA [18].

The problem in using "observed" structure factors estimated by the Rietveld refinement method is that these factors are biased towards the structural model used as both phases and calculated profiles used for the intensity partitioning are derived from the model. This approximate nature of the procedure for extracting integrated intensities lowers the accuracy of the electron densities determined by combining Rietveld and MEM for analysis.

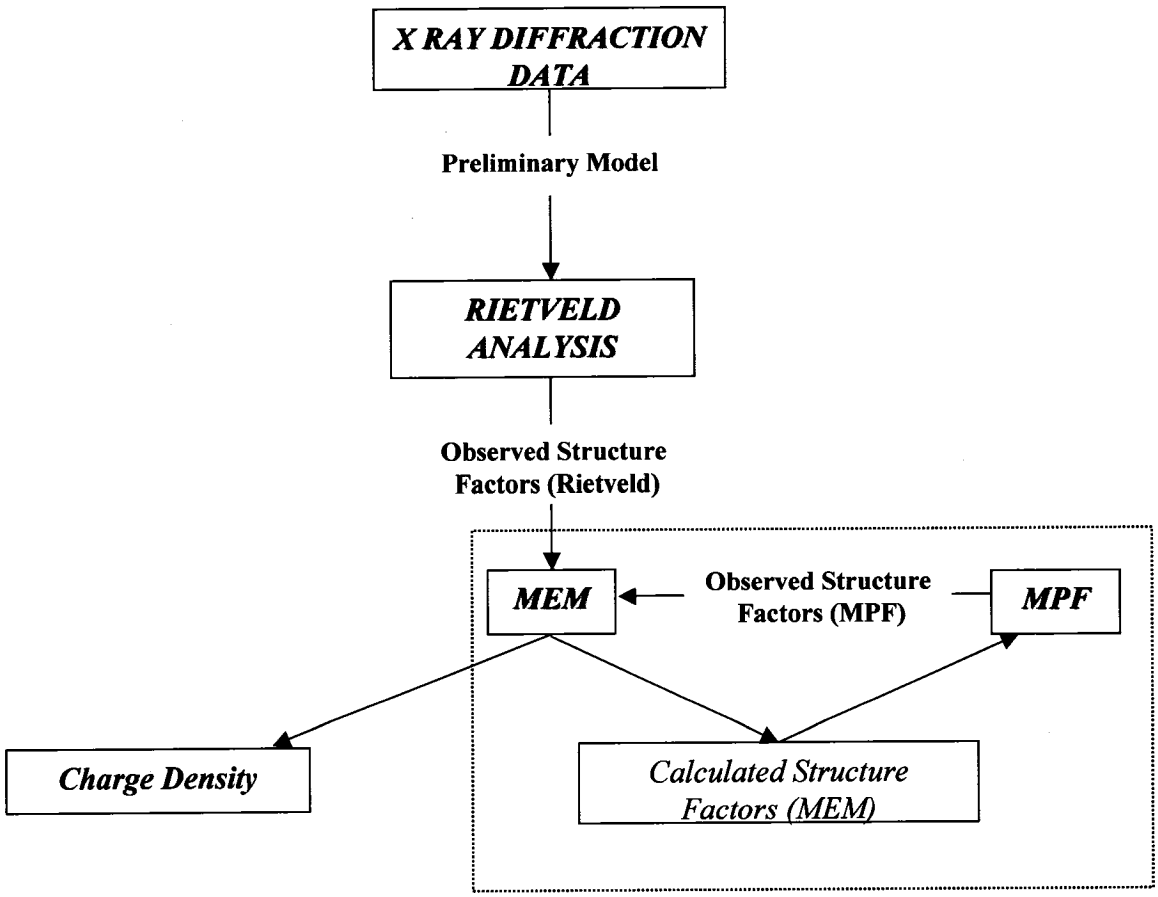

Figure 2.2. Rietveld/MEM/MPF analysis. The dotted frame comprises the MEM/MPF iterative process.

To minimize the bias due to the structural model, the MEM/Rietveld analysis is followed by iterations of another analysis method, **M**EM-based **P**attern **F**itting (MPF) [19]. The MEM software evaluates calculated structure factors, F_c(MEM), by Fourier transform of the electron densities. Then, we fit the calculated pattern to the observed one by fixing structure factors at values of F_c(MEM) obtained from the previous MEM analysis and refining only parameters irrelevant to the crystal structure (background, peak profile, etc.). Calculated structure factors estimated by the MPF method as described before, F_o(MPF), are analyzed again by MEM.

A schematic of the whole data analysis process is shown in Figure 2.2. In addition to the minimization of the structural model influence, the MPF method has another

advantage: it is significantly increasing the quality of the fit between measured and calculated patterns [19]. This iterative procedure is repeated until the goodness-of-fit parameters (especially R_I and R_F) of the pattern fitting procedure no longer decreases. Repetition of the MPF weakens the influence of the structural model on F_o (MPF).

Two type of factors are defined as measures of reliability of the MEM analysis [16], namely, R_F and R_{wF}:

$$R_F = \frac{\sum_{i=1}^{M_F} |F_c(K_i) - F_o(K_i)| + \sum_{i=1}^{M_G} |G_{ci} - G_{oi}|}{\sum_{i=1}^{M_F} |F_o(K_i)| + \sum_{i=1}^{M_G} |G_{oi}|}, \tag{2.13}$$

$$R_{wF} = \sqrt{\frac{\sum_{i=1}^{M_F} \frac{|F_c(K_i) - F_o(K_i)|^2}{\sigma_i^2} + \sum_{i=1}^{M_G} \frac{|G_{ci} - G_{oi}|^2}{\sigma_i^2}}{\sum_{i=1}^{M_F} \frac{|F_o(K_i)|^2}{\sigma_i^2} + \sum_{i=1}^{M_G} \frac{|G_{oi}|^2}{\sigma_i^2}}}. \tag{2.14}$$

The goal is to minimize those factors, but one must keep in mind that, although very important, numerical criteria are needed for assessment of the fit in quantitative detail while graphical examination of the results makes noting gross errors and omissions easy. One must ensure that the density distributions obtained make physical and chemical sense before drawing conclusions based on numerical criteria.

Uncertainties in the MEM calculated electron density distributions will be further addressed for the specific case of the charge density study of dense Ba_8Si_{46} (Chapter V).

References

1. M. F. C. Ladd and R. A. Palmer, *Structure Determination by X-ray Crystallography* (Plenum Press, 1993).
2. P. Coppens, *X-Ray Charge Densities and Chemical Bonding* (International Union of Crystallography, Oxford University Press, 1997).
3. C. J. Gilmore, *Acta Cryst. A* **52**, 561-589 (1996).

4. M. Sakata and M. Sato, *Acta Cryst.* **46**, 66 (1990).
5. H. Shimotani, T. Ito, Y. Iwasa, A. Taninaka, H. Shinohara, E. Nishibori, M. Takata, and M. Sakata, *J. Am. Chem. Soc.* **126**, 364 (2004).
6. E. Nishibori, I. Terauchi, M. Sakata, M. Takata, Y. Ito, T. Sugai, and H. Shinohara, *J. Phys. Chem.* **110**, 19215 (2006).
7. M. Takata, E. Nishibori, B. Umeda, M. Sakata, E. Yamamoto, and H. Shinohara, *Phys. Rev. Lett.* **78**, 3330 (1997).
8. A. Hoshikawa, N. Igawa, H. Yamauchi, and Y. Ishii, *J. Chem. Phys.* **125**, 034505 (2006).
9. K. Kato, M. Sakata, E. Nishibori, M. Takata, N. Hamada, and Y. Moritomo, *J. Phys. Soc. Jpn.* **74**, 2137 (2005).
10. B. B. Iversen, F. K. Larsen, M. Souhassou, and M. Takata, *Acta. Cryst. B* **51**, 580 (1995).
11. M. Sakata, T. Itsubo, E. Nishibori, Y. Moritomo, N. Kojima, Y. Ohishi, and M. Takata, *J. Phys. Chem. of Solids* **65**, 1973 (2004).
12. T. Yamanaka, *J. Synchrotron Rad.* **12**, 566 (2005).
13. K. Kato, Y. Ohishi, M. Takata, E. Nishibori, M. Sakata, and Y. Moritomo, *Phys. Rev. B* **71**, 012404 (2005).
14. M. Takata and M. Sakata, *Acta Cryst. A* **52**, 287 (1996).
15. M. Merli and A. Pavese, *Z. Kristallogr.* **221**, 613 (2006).
16. R. A. Dilanian and F. Izumi, *PRIMA Manual* (2004).
17. F. Izumi and T. Ikeda, *Mater. Sci. Forum*, **321-324,** 198 (2000).
18. F. Izumi and R. A. Dilanian, *Recent Research Developments in Physics* **3**, Transworld Research Network, Trivandrum, 699 (2002).
19. F. Izumi and T. Ikeda, Commission on Powder Diffraction, *IUCr Newslett.* **26**, 7 (2001).

CHAPTER III

Experimental Details

All angular dispersive powder X-ray diffraction experiments on gas hydrates were performed at the Cornell High Energy Synchrotron Source (CHESS), USA, beamlines B2 and A2, under high pressure and room temperature conditions. In the following sections, details about the experimental setup used for angular dispersive X-ray diffraction, description of the instruments used, and reasons for carrying on our X-ray diffraction experiments at a synchrotron radiation facility are presented.

3.1 Angular Dispersive X-ray Diffraction: Transmission Geometry

A schematic of the transmission geometry, used in the X-ray diffraction experiments, is presented in Figure 3.1.

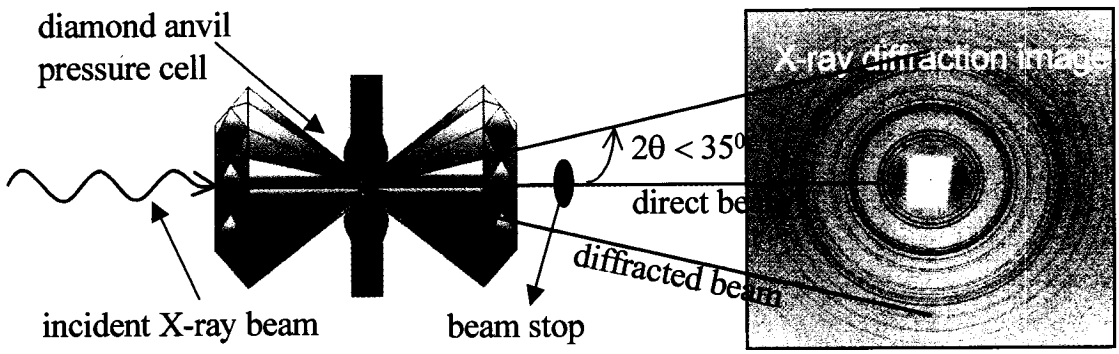

Figure 3.1. Schematic diagram of the angular dispersive X-ray diffraction experimental setup (transmission geometry).

In Figure 3.1, the main apparatus used in the experiment are shown: the diamond anvil cell (DAC), which contains the sample and is used to generate high pressure, and an image plate detector (IP) to record the X-ray diffraction rings arising from the sample. The actual experimental setup also contains collimators, to ensure a small synchrotron beam size on the sample, and a sample goniometer and point detector used to precisely align the sample in the X-ray beam. Sample alignment is performed by measuring the intensity of the transmitted beam through the DAC as a function of cell position.

A good alignment in the transmission geometry implies that both the IP detector and the flat faces (culets) of the DAC are placed perpendicular, as best as possible, to the incident X-ray beam, with the sample centered on the synchrotron beam. The accessible diffraction angle is limited to 35°, as indicated in Figure 3.1, due to the geometry of the diamond anvil cell, as explained in the next section. A small lead beam stop is used to attenuate the undiffracted (direct) X-ray beam to avoid damaging the detector. The shadow of the beam stop can be observed as a blank region in the center of the diffraction image. In the following sections, the DAC and IP detectors will be described in detail.

3.2 Diamond Anvil Cell

The diamond anvil cell (DAC) is a device capable of generating pressures almost as high as those found in the center of the Earth [1]. By applying such pressures to small samples, physical properties of materials can be studied as a function of density using a variety of experimental techniques, e.g., X-ray and neutron diffraction, Raman spectroscopy, X-ray inelastic scattering, and optical microscopy.

The DAC is based upon an opposed-diamond configuration, in which a sample is placed between the culets of two diamond "anvils" and is constrained on the sides by a metallic gasket (Figure 3.2). In that configuration, a modest force is required to create extremely large pressures in the sample chamber. DACs use diamond because it is known as the hardest, least compressible material and is transparent to high energy X-rays (Figure 3.3) and visible light. In order to obtain a hydrostatic pressure and to prevent damage of the diamonds, the faces of the anvils have to be aligned perfectly parallel.

Also, in some cases, depending on the sample, a pressure-transmitting medium, for instance, a methanol-ethanol mixture, nitrogen, argon, or helium is loaded together with the sample to ensure the best hydrostatic pressure conditions. When a diamond anvil cell is used in an X-ray diffraction experiment, only a part of the X-ray diffraction rings are accessible to measurement. This accessible angular range depends on the specific geometry of each pressure cell and is limited by the absorption of the diffracted rays in the tungsten carbide (WC) and Be plates supporting the two diamonds. In the case of the DACs used in our experiment the maximum angle is about 35°.

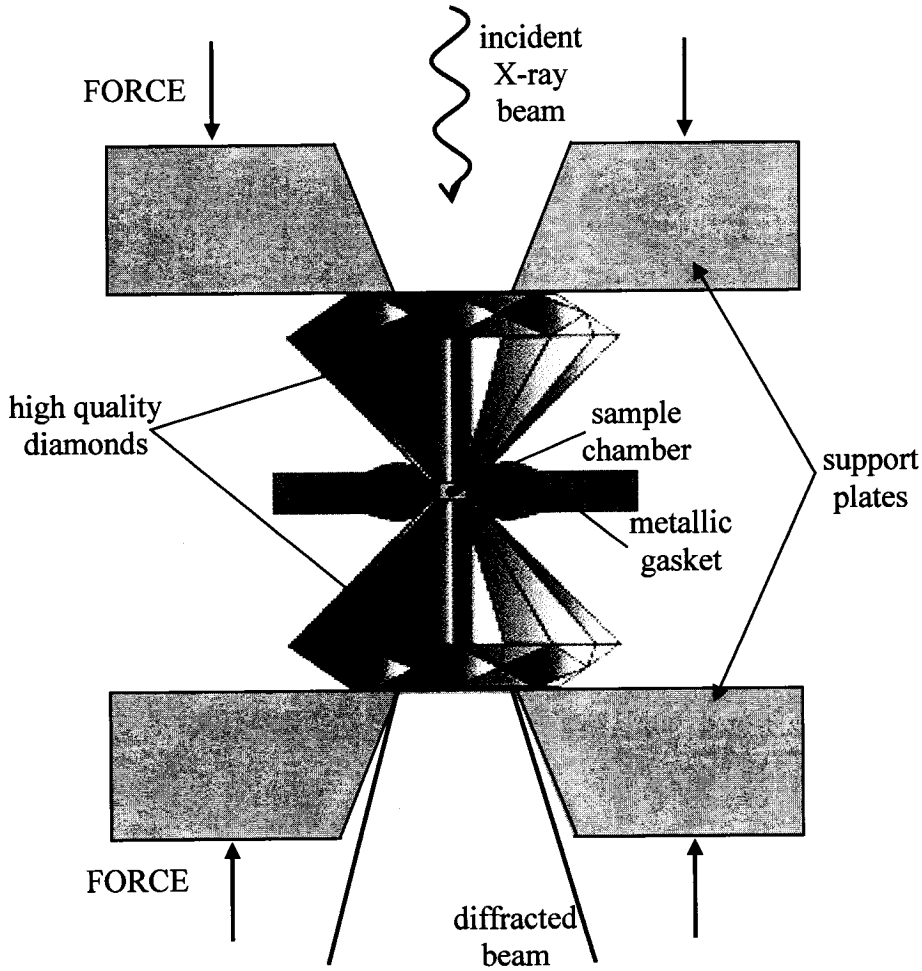

Figure 3.2. Schematic diagram of the DAC showing a sample constrained between diamond anvils and a metallic gasket. Diamond anvils are supported by strong WC and Be seats on which an external force is applied to generate pressure.

Although the study of gas hydrates presented in this thesis is limited to pressure only up to 2 GPa, experiments up to at least 50 GPa are commonly carried out in our laboratory.

Given the fact that samples compressed in DACs are very small, with volume of material of about 1000 μm^3, the use of highly intense X-ray radiation is imperative. Intense X-ray beams arise from synchrotron radiation.

3.3 Synchrotron Radiation: a Key to Intense X-ray Beam

If the trajectory of an electron (or positron) beam, traveling at relativistic speeds, is curved, it emits a continuous spectrum of electromagnetic radiation called synchrotron radiation. The energy of the electrons in the storage rings used for X-ray diffraction experiments is, typically, between 2-8 GeV. X-ray beam parameters like divergence and intensity at a certain wavelength value are determined by the energy of the electron beam. A 5.3 GeV electron beam is used as the source of synchrotron radiation at CHESS.

Due primarily to the small size of a sample compressed in a DAC, all X-ray diffraction experiments were carried out using synchrotron X-ray beam. A very small volume of sample requires a high flux of incident X-rays on the sample, so that a reasonable exposure time to record X-ray diffraction can be set. From this point of view, and several others which will be presented shortly, a synchrotron radiation source is far superior to a conventional X-ray source. As an example, the brilliance (photon intensity per $mrad^2$, per bandwidth, per unit of source area) of a sealed tube is 10^8 photons s^{-1} $mrad^{-1}mm^{-2}$ per 0.1% energy bandwidth while the third generation of high-energy synchrotron radiation sources provide beams with brilliance in the order of 10^{19} photons $s^{-1}mrad^{-1}mm^{-2}$ per 0.1% energy bandwidth [2].

Our experiments were carried out using monochromatic radiation (λ=0.4959 Å) obtained from a 49-pole wiggler and a Si(111) double crystal monochromator (CHESS A2 station) and from a bending magnet and a Ge(111) double crystal monochromator (CHESS B2 station). The use of Ge (111) crystals gives a larger energy bandwidth resulting in an increase of photon flux as compared to the Si(111) crystals.

Besides its high intensity, synchrotron sources have other great advantages very important in a high-pressure experiment, when comparing to conventional X-ray sources: tunable wavelength, parallel beam, and small beam size. These characteristics will be presented in the following sections.

3.3.1 Tunable Wavelength

Being able to choose the incident X-ray wavelength is important for several reasons: as Figure 3.3 shows, the transmission through diamond is strongly decreasing with the increase of wavelength, in the 0.4-1.4 Å region. Consequently, the X-ray diffraction experiments should be run at wavelengths lower than 0.7 Å, in order to have at least a 50% transmission (gray region on Figure 3.3). Also, a high background due to fluorescence can be avoided by tuning the wavelength to a value away from the absorption edge of the sample. Moreover, given the geometry of the DAC (see Figure 3.2), a limited angular range, $2\theta < 35^{\circ}$, is accessible for measurements.

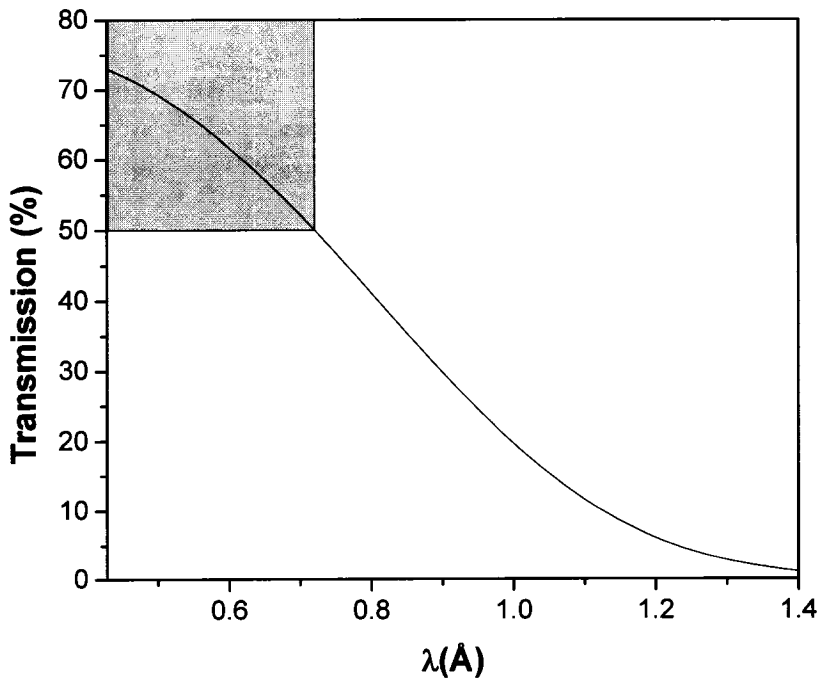

Figure 3.3. Transmission of X-ray radiation through a 4 mm-thick diamond as a function of wavelength [3].

As for most powder X-ray diffraction experiments, a favorable ratio between observation and unknown structural parameters would translate in an experimental *d*-spacing region down to about 1 Å, the incident wavelength has to be chosen by also taking into account this factor. Figure 3.4 shows that if a wavelength larger that 0.7 Å is used in high-pressure experiment a *d*-spacing region significantly higher than 1 Å will be accessible to X-ray diffraction measurements. The shaded area represents the experimental accessible angular limit when using DAC and a minimum *d*-spacing of 1 Å required in most X-ray diffraction experiments. The diffraction angle – *d*-spacing dependence is presented for several wavelengths. The three largest wavelengths, marked as dotted lines, are typical wavelengths available from conventional X-ray sources. The value 0.49 Å is used in our experiments. A value of 0.37 Å is the lowest wavelength for which X-ray diffraction studies were reported; tuning the synchrotron radiation to a smaller value leads to a dramatic decrease in beam intensity.

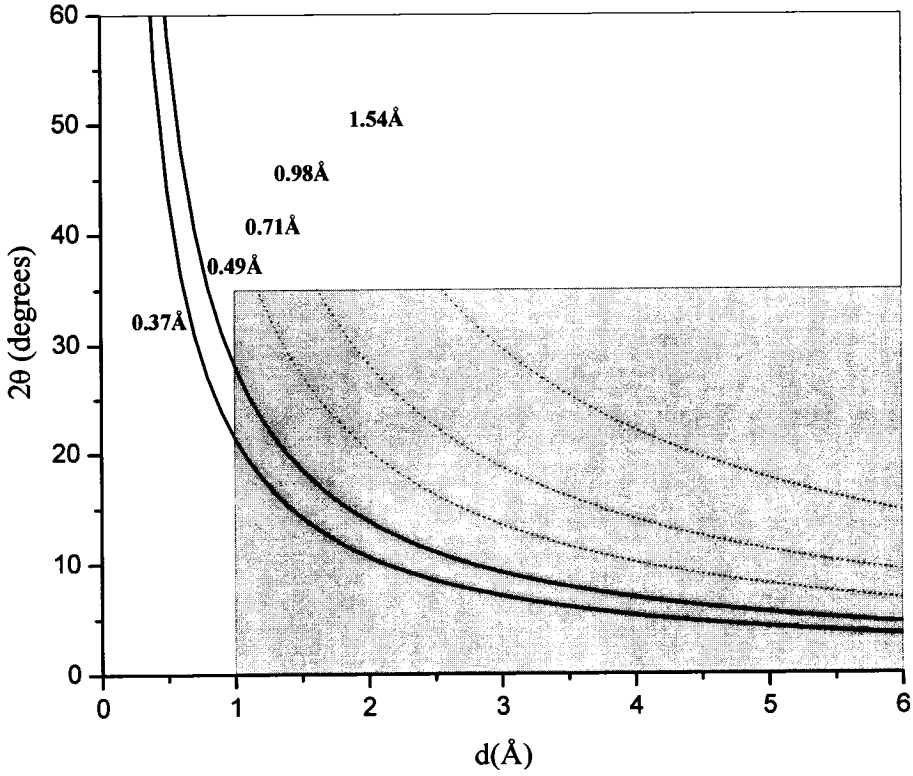

Figure 3.4. Dependence of the diffraction angle (twice the Bragg angle) with *d*-spacing, emphasizing the need to use X-ray radiation with wavelength lower then 0.7 Å in a high-pressure experiment performed using a diamond anvil cell.

3.3.2 Parallel Beam

The small divergence of the X-ray beam contributes to the fact that high-resolution powder X-ray diffraction patterns are obtained when using synchrotron radiation. For our X-ray diffraction datasets collected at CHESS, the full width at half maximum (FWHM) values for non-overlapping peaks were typically down to 0.06 degrees and the limiting experimental factor is the spatial resolution of the X-ray detector.

3.3.3 Small Beam Size

As the volume of samples loaded in DAC are small, the use of a highly collimated incident X-ray beam is desirable in order to avoid the appearance of X-ray diffraction lines other than those arising from the sample (e.g. peaks arising from the gasket). By performing transmission measurements, a precise alignment of the sample with the incident beam is assured. A very small beam size at sample (in the order of tens of μm^2) can be achieved, using mirrors and collimators, and still have a high photon flux in that area. The use of collimators is practical because the incident synchrotron beam is rather small, due to the combined effect of a small electron beam source (0.1 to 1 mm) and very low divergence of the synchrotron radiation beam (about 10^{-4}-10^{-5} rad) [4].

3.4 Area X-ray Detector

For the detection of the diffracted X-ray photons, Fuji ST-VI and MAR 345 image plates (IP) were used. These are area detectors, consisting of a thin layer of a phosphor ($BaFBr:Eu^{2+}$), which can be photo-stimulated by X-rays [5, 6]. The electrons excited from Eu^{2+} ions by the incident X-rays are trapped in a metastable state by Br and F vacancies, forming temporary "color centers". This latent image can be then read by means of a custom laser scanner. A Ne-He laser beam scans the image plate point by point, liberating the trapped electrons which will recombine with a hole. This

recombination process is accompanied by emission of luminescence, with intensity proportional to that of the X-rays incident on the image plate. The emitted light is then detected by a photo-multiplier tube, amplified, and digitally converted. Typical exposure times used in our high-pressure gas hydrates experiments are 15-30 minutes.

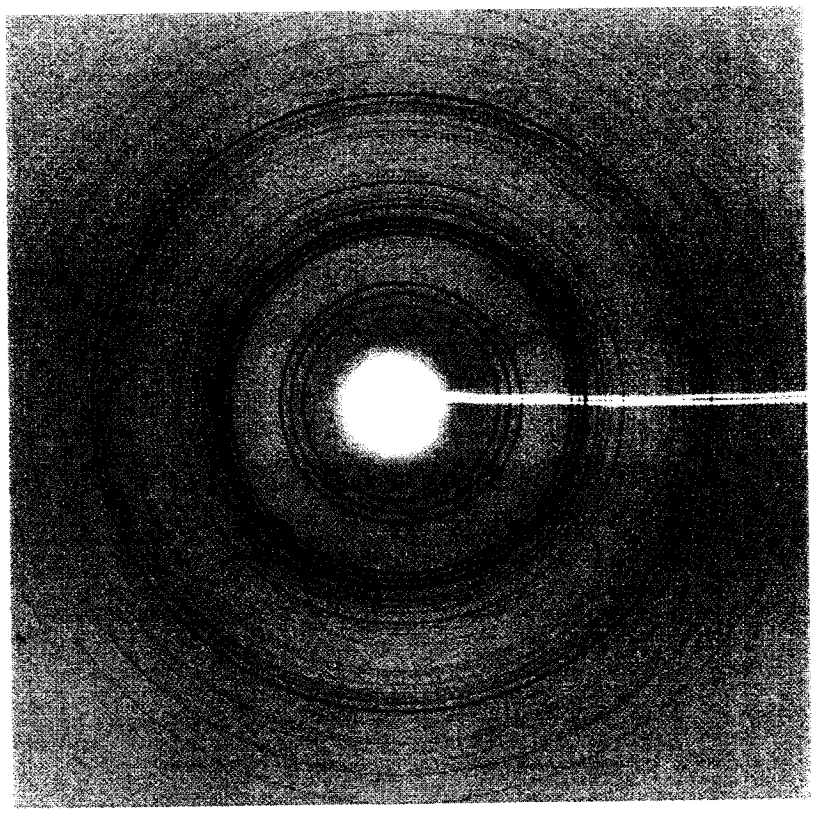

Figure 3.5. Typical 2D X-ray diffraction image of the sI gas hydrate recorded using an IP detector. The shadows of the beam stop and diode (used to monitor the flux of the X-ray transmitted beam) connection appear as blank region in the center and on the right side of the diffraction image, respectively.

An X-ray diffraction image recorded at CHESS using Fuji ST-VI IP is shown in Figure 3.5. The high quality of the diffraction image, representative for the gas hydrates patterns reported in this thesis, reflects the good quality of the samples. The uniform intensity along the diffraction ring observed in Figure 3.5 shows that the sample consisted of a fine crystalline powder (no grains or amorphous regions), and showing no preferred

orientation or strain. The large, intense Bragg spots arise from the single crystal diamonds.

3.5 Processing of the X-ray Diffraction Image

The digital image read from the image plate detector is processed and integrated using SImPA [7] and Fit2D [8] software. Often times, the X-ray diffraction image contains intense Bragg spots, which arise for instance from the single crystal diamonds; those Bragg spots are masked prior to the integration of the X-ray diffraction images. In order to integrate over the X-ray diffraction or Debye rings to obtain an "Intensity vs. 2θ" pattern, one needs to know the distance from the sample to the detector, for a given wavelength. In our experiments, this distance is found using an X-ray standard (silicon, NIST standard reference material 640b). An X-ray diffraction pattern of the Si standard, placed at the same position as the actual sample by loading Si in the DAC without applying pressure, is recorded with the area detector at fixed position. As the *d*-spacings corresponding to silicon X-ray diffraction peaks are well known [8], the sample-to-detector distance can be calculated. The spot where the direct beam hits the image plate is used to locate the position of the incident X-ray beam from which the 2θ angle is measured. Also, tilt corrections are performed in the software, using the X-ray diffraction image of the Si standard, to account for the fact that the image plate is not necessarily placed perfectly perpendicular to the transmitted X-ray beam.

3.5 Pressure Measurements

The ruby ($Al_2O_3:Cr^{+3}$) luminescence technique [9] is used to measure the pressure applied on the sample. Small ruby micro-spheres are loaded in the DAC together with the samples and the wavelength of the R_1-luminescence band is measured each time the pressure in the sample chamber was changed. The pressure value (in GPa) is calculated using pressure calibration curve:

$$P = 380.8\left[\left(\frac{\lambda}{\lambda_0}\right)^5 - 1\right], \tag{3.1}$$

where λ is the wavelength of R_1 peak at a given pressure and

λ_0 is the wavelength of R_1 peak at atmospheric pressure.

The position of the R_1-luminescence band at atmospheric pressure is measured for each set of ruby spheres used, as even a small difference compared with the accepted value would introduce significant errors in the pressure value, visible especially in the low pressure range of measurements (below 1.0 GPa). The mean wavelength corresponding to the R_1-luminescence band is 694.26 nm. The pressure values, calculated from equation (3.1), are reported up to 2 decimals in this thesis. Note that we can measure very accurate values, which are not necessarily very precise due to possible imperfections in detector calibration and, in the case non-hydrostatic pressure conditions in the sample chamber.

All gas hydrates samples were synthesized at the NRC, Ottawa, by absorption of the relevant gases into ice. Details of the procedure used were presented by Y. P Handa [10].

References

1. E. Soignard and P. F. McMillan, An Introduction to Diamond Anvil Cells and Loading Techniques, from *High Pressure Crystallography*, Kluwer Academic Publishers, 81 (2003).
2. Philip Coppens, *Synchrotron Radiation Crystallography*, Academic Press Lt., 1992.

3. L. A. Aslanov, G. V. Fetisov and J. A. K. Howord, *Crystallographic Instrumentation*, International Union of Crystallography, Oxford University Press, 1998.
4. http://henke.lbl.gov/optical_constants/filter2.html
5. A. Kinne, M. Thoms, H. R. Ress, T. Gerhard, M. Ehinger, W. Faschinger, and G. Landwehr, *J. Appl. Cryst.* **31**, 446 (1998).
6. M. Thoms, H. von Seggern, and A. Winnacker, *Phys. Rev. B* **44**, 9240 (1991).
7. S. Desgreniers and K. Lagarec, Technical report, LPSD/Université d'Ottawa (unpublished, 1997).
8. A. P. Hammersley, S. O Svensonn, M. Hanfland, A. N. Fitch, and D. Häusermann, *High Press. Res.* **14**, 235 (1996). FIT2D, European Synchrotron Radiation Facility. (1998).
9. H.K. Mao, J. Xu, and P.M. Bell, *J. Geophys. Res.* **91B**, 4673 (1986).
10. Y. P Handa, *J. Chem. Thermodyn.* **18**, 891 (1986).

CHAPTER IV

High-Pressure Powder X-ray Diffraction Study of Structure I Xe and Kr Clathrate Hydrates – Results and Discussion

A structural study of structure I (sI) xenon and krypton clathrate hydrates at high pressure and room temperature will be presented in this chapter. The structural properties of the sI gas hydrate phase are well documented from low-temperature studies of methane hydrate [1, 2]. Also, recent high-pressure X-ray and neutron diffraction and Raman spectroscopy reports clarified the pressure induced phase transformation sequence of Kr [3, 4], Xe, nitrogen [5], and methane hydrates [6-8]. However, to our knowledge, there are no detailed studies of the changes induced by pressure in the structural parameters or electron density topology of sI rare gas clathrate hydrates. Such a study can help the understanding of hydrophobic interactions between the water cage molecules and guest atoms, and mechanisms leading to a transition to a denser phase. For this purpose, high pressure powder X-ray diffraction experiments on Xe and Kr hydrates were performed at room temperature. Data were analyzed using the combined Rietveld and the Maximum Entropy (MEM) methods. After the sequence of high-pressure phases that these compounds undergo was established, a detailed analysis of the effect of pressure on the structural parameters and charge density distributions of sI Xe and Kr hydrates was performed. We focused our research on the sI phase as it is a common phase for both Xe and Kr hydrates (and also for many other clathrate hydrates) and the quality of the X-ray diffraction patterns recorded in the experiments was sufficient to successfully carry out a Rietveld and MEM analysis. Although X-ray diffraction patterns from the denser sH phase were recorded for both Xe and Kr hydrates, their quality was lower than that of sI patterns and performing meaningful Rietveld analysis was not possible. This is due, on one hand, to the appearance of grains in the sample, accompanying the sI-sH phase transition. On the other hand, the excess H_2O, in the form of ice VI and ice VII, is usually

produced during the phase transition, making the task of sH structure refinement even more difficult. We believe the later problem might be overcome to a good extend by performing the experiment at lower temperature conditions. The present chapter is organized as follows: at first, the structural properties of the three most common phases of the gas clathrate hydrates, structure I, structure II, and structure H, will be introduced. Then, the sequence of phase transitions that Xe and Kr hydrates undergo as a result of the application of pressure will be shown, and results from the Rietveld refinement and MEM analyses will be reported and discussed.

4.1 Crystalline Structure Gas Hydrates

Clathrate hydrates are inclusion compounds, in which guest molecules or atoms are trapped in cages formed by an ice-like host network of water molecules [9], thus the name "clathrates"- from the Latin "clathratus", "to encage".

Hydrates were discovered by Humphrey Davy (1811) [10], while working with mixtures of chorine and water. Up to the present times, the goal of the research on gas hydrates was to identify possible hydrate forming gases, study the pressure-temperature conditions for formation, and determine the composition and physical properties of hydrates. Today, three crystal structures are known as the most common clathrate hydrates structures: cubic structure I (sI) [11], cubic structure II (sII) [12], and hexagonal structure H (sH) [13].

Even though the detailed shape of the cavities (cages) in clathrates is different for each of the three hydrate structures, there are similarities, and the network of water molecules forming the cages is the same: the water molecules are connected to four nearest neighbor molecules through hydrogen bonds.

In order to stabilize the clathrate hydrate structures, a guest molecule or atom is needed. Otherwise, the attractive interactions between the water molecules forming the cavities lead to an inward directed force, and, subsequently, the collapse of the cage and the instability of the clathrate. Therefore, two types of interactions play a dominant role in stabilizing gas clathrate hydrate structures: the hydrogen bonds between the water

molecules forming the cages and the van der Waals interactions between the encaged atoms or molecules and the water framework. The size of the guest atom or molecule determines the size of the cage and, consequently the type of crystalline structure that the hydrate adopts.

In the following subsections, the structure of each of the three common phases of the gas clathrate hydrates, mentioned earlier, will be presented in detail.

4.1.1 Structure I Gas Clathrate Hydrates

Structure I, which has a cubic symmetry with *Pm3n* space group and a lattice constant of about 12 Å, is a low-pressure phase common for many gas clathrate hydrates. The first detailed crystallographic study of this structure was performed on the ethylene oxide hydrate in 1965 [14]. The hydrate structure I was found to be formed by two types of polyhedra, also referred to as cages. The 12-sided polyhedron (small cage) has twelve pentagonal faces (5^{12}). The 14-sided cavity (large cage) is delimited by 12 pentagonal and 2 hexagonal faces ($5^{12}6^2$). Pentagonal faces connect these types of cages to each other (Figure 4.1). Cages in sI are formed by three unique oxygen atoms, situated at Wyckoff positions *16i*, *24k*, and *6c* (further denoted in this chapter as O(*1*), O(*2*), and O(*3*), respectively) and three unique hydrogen atoms at Wyckoff positions *16i*, *24k*, and *48l*. At full occupancy, each cage, large and small, hosts one guest atom or molecule, at Wyckoff positions *2a* (small cage) and *6d* (large cage).

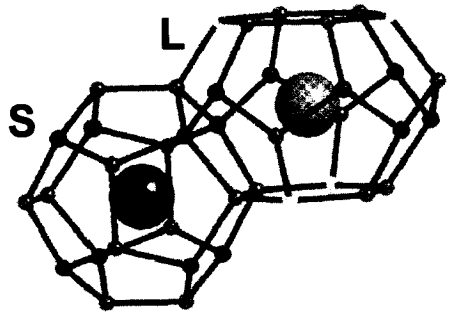

Figure 4.1. Small and large cages that form Structure I gas clathrate hydrates, connected by their pentagonal faces. For the cage framework, only the oxygen atoms are shown. The spheres inside the cavities represent a full cage occupancy with one guest atom/molecule [15].

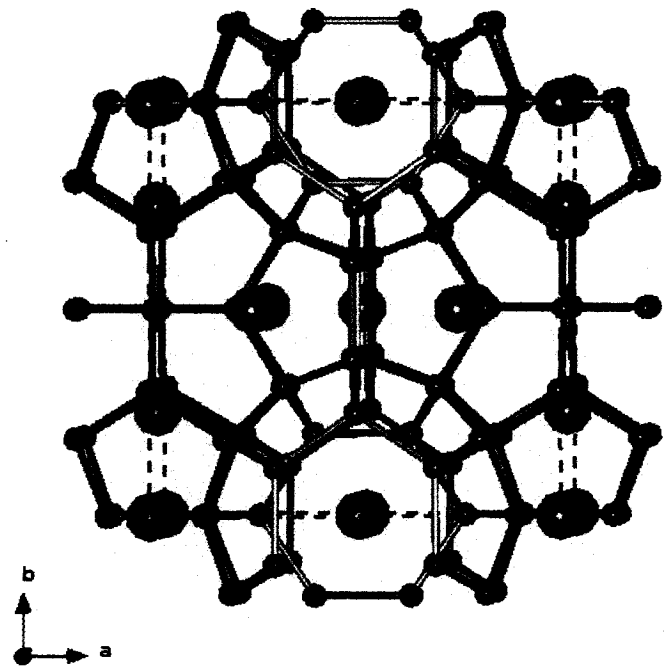

Figure 4.2. The cubic unit cell of sI clathrate hydrates with one guest atom/molecule occupying each cage. The large spheres represent the guest atoms and the small ones represent the oxygen atoms. For the sake of clarity, the hydrogen atoms are not displayed. The dotted lines mark the limits of one unit.

One unit cell consists of two small cages (located at the corners and in the middle), having an average diameter of about 15.6 Å, and six large cages (situated on the faces of the unit cell), with an average diameter of 18.7 Å (Figure 4.2).

Given the dimensions of the two types of cages, only molecules/atoms with diameter up to 6 Å (e.g. CH_4, Xe) can form this structure. These stability conditions in relation to the size of the guest species are valid at atmospheric pressure conditions. The same comment applies for sII and sH phases which will be discussed in the next subsections.

The guest/water molecule ratio for sI is 5.75 for a fully occupied $G_8(H_2O)_{46}$ (G being the guest species).

4.1.2 Structure II Gas Clathrate Hydrates

Structure II also has a cubic structure, with the space group *Fd3m* and a lattice constant of about 17 Å. Structure II consists of a network of small (5^{12}) cages (pentagonal dodecahedra), connected through face sharing in three dimensions [16]. The voids between these small cavities form the large ($5^{12}6^4$) cages (hexakaidecahedra) that are connected through the hexagonal faces (Figure 4.3). The unit cell of sII hydrate contains 16 small cages and 8 large cages that form a diamond lattice (with a chemical formula: corresponding to $G_{24}(H_2O)_{136}$, with G being the guest species). The guest/water molecule ratio for sII is 5.67 for a fully occupied $G_{24}(H_2O)_{136}$.

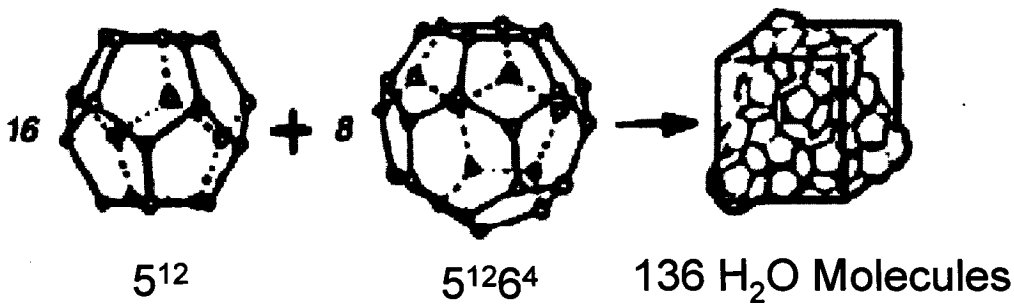

Figure 4.3. A schematic drawing of the two types of cages forming the cubic unit cell of sII gas hydrates [16].

With an average diameter of 32.9 Å, the hexakaidecahedra are bigger than the large cages forming structure I. They are also the most spherical of all the cavities of the three common clathrate hydrate structures; they can host molecules with diameters as large as 6.6 Å.

As the large cages in sII can host larger molecules than any of the cages in sI, it was thought for a long time that sII is only formed with guest molecules too large to fit in any of the cavities forming sI, for instance, propane or iso-butane. Later, neutron and X-ray diffraction studies showed that atoms or molecules with van der Waals diameters smaller than 4.2 Å (e.g. hydrogen, nitrogen, oxygen, argon, krypton) can form sII

hydrates [17]. This situation can be explained by the fact that sI hydrates are formed only when the size of the guest is less than 5.8 Å but sufficiently large (minimum 4.2 Å) such that the occupation of large tetrakaidecahedra cages (superior in number to small cages) is favored over the small dodecahedra cages. If the size of the guest is too small and the latter requirement no longer holds, then sII, having more dodecahedra cavities, has greater stability than sI.

4.1.3 Structure H Gas Clathrate Hydrates

Structure H is an hexagonal structure having the *P6/mmm* space group and lattice parameters of about a=12 Å and c=10 Å [13]. Its unit cell (Figure 4.4) contains three different types of cages: 3 pentagonal dodecahedra (5^{12}), 2 irregular dodecahedra ($4^3 5^6 6^3$), and one icosahedron ($5^{12}6^8$), referred to as small, medium and large cages, respectively (Figure 4.5). The large $5^{12}6^8$ cages are the largest of the hydrate cages, able to encage guest molecules as large as cyclooctane (van der Waals diameter of about 9 Å). Structure H cannot be formed with only one guest species. It will only form with the help of small guest molecules that occupy and stabilize the small cages. The guest/water molecules ratio for sH is 5.67 for a fully occupied $G_6(H_2O)_{34}$.

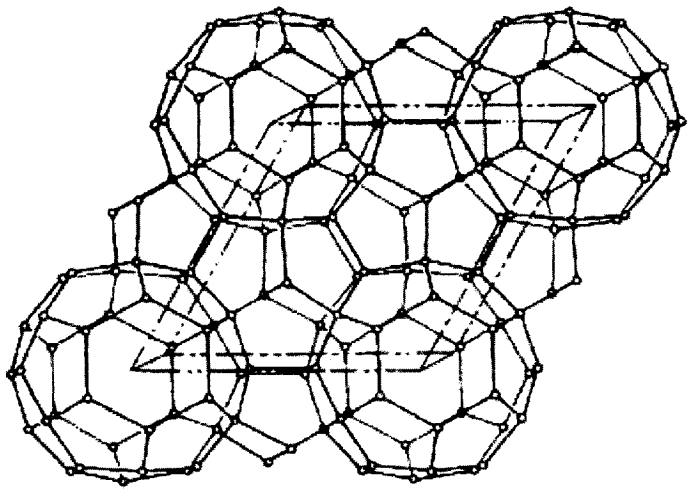

Figure 4.4. Structure of the host H_2O lattice in sH clathrate hydrate [9]. The limits of the hexagonal unit cell, formed by the three types of cavities detailed in the text and Figure 4.5, are marked by the dotted lines.

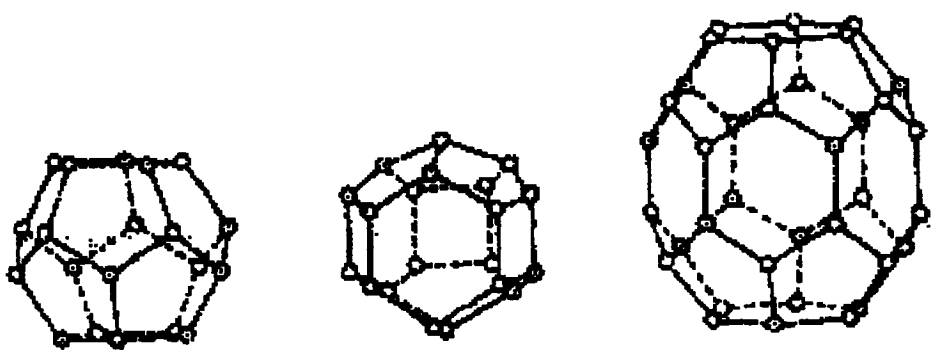

Figure 4.5. Geometry of the three types of cages occurring in sH gas hydrate [18].

In the following sections, experimental results from a high pressure X-ray diffraction study of Xe and Kr clathrate hydrates will be presented.

4.2 Structural Parameters of Kr and Xe Clathrate Hydrates: Refinement using the Rietveld Method

The sequences of low-pressure phases of Xe and Kr hydrates, as observed from the X-ray diffraction experiments, as well as the Rietveld refinement results will be presented in this section.

4.2.1 Xenon Clathrate Hydrate

Xenon clathrate hydrate is already known to adopt sI symmetry at low temperature and atmospheric pressure [5].

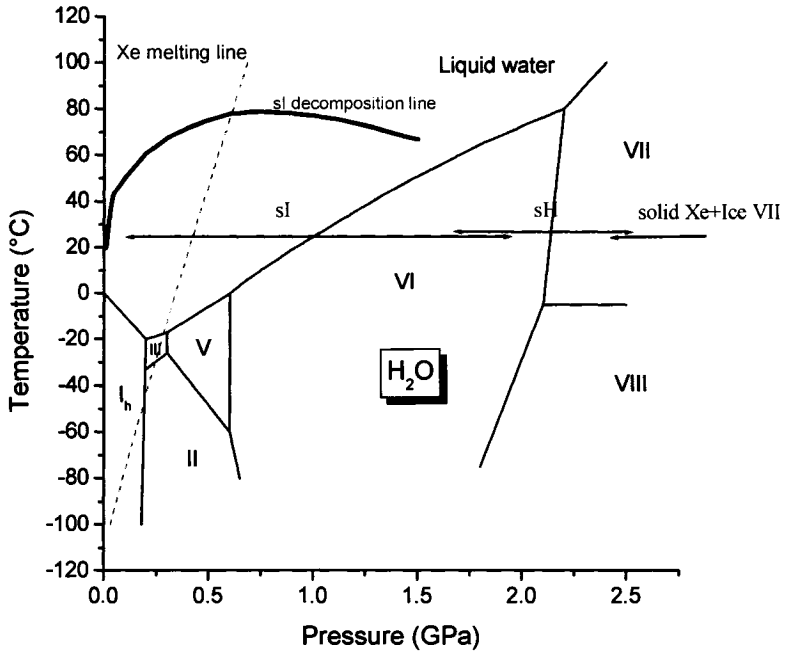

Figure 4.6. Temperature-pressure phase diagram of H_2O (black curves) with Xe clathrate hydrate stability fields at room temperature. Pressure stability ranges, at room temperature, of sI and sH Xe hydrates are represented by blue lines. The decomposition line of sI Xe clathrate (red curve) [20] and the melting line of pure xenon (green line) [21] are also presented.

In the following, X-ray diffraction patterns supporting the sI pressure stability range information presented in Figure 4.6 are shown. The starting pressure in the experiment was 0.16 GPa, at which sI hydrate phase can be observed. The pressure was gradually increased and, at 1.98 GPa, peaks from the next high pressure phase, the hexagonal structure (sH), started to develop (Figures 4.7 and 4.8).

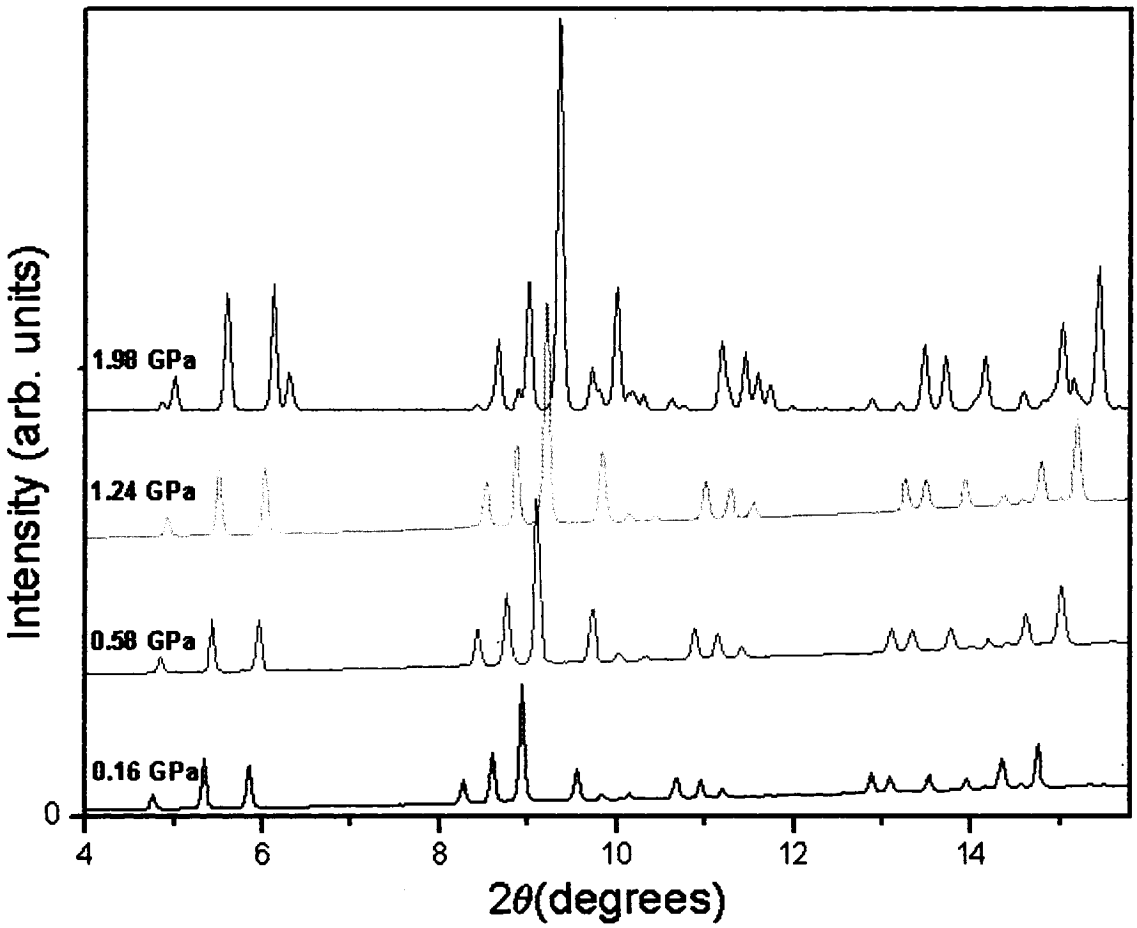

Figure 4.7. Integrated powder X-ray diffraction patterns of Xe hydrate recorded at increasing pressures. For the first three low-pressure patterns, all peaks could be indexed to the sI space group, *Pm3n*. The pattern at 1.98 GPa shows a mixture of sI and sH phases.

Each X-ray diffraction pattern presented in Figure 4.7 was analyzed in detail. For the X-ray diffraction pattern collected at 1.98 GPa, each peak was indexed to either cubic

sI or hexagonal sH structures, as shown in Figure 4.8. A Rietveld analysis, using RIETAN software [22], was carried out for the single phase sI patterns, recorded at 0.16, 0.58, and 1.24 GPa, to determine the structural properties as a function of pressure. Furthermore, the Rietveld and MEM/MPF analysis were performed over an angular range (expressed in terms of $\sin(\theta)/\lambda$) up to 0.452, 0.454 and 0.445 $Å^{-1}$ for the patterns measured at 0.16, 0.58, and 1.24 GPa, respectively.

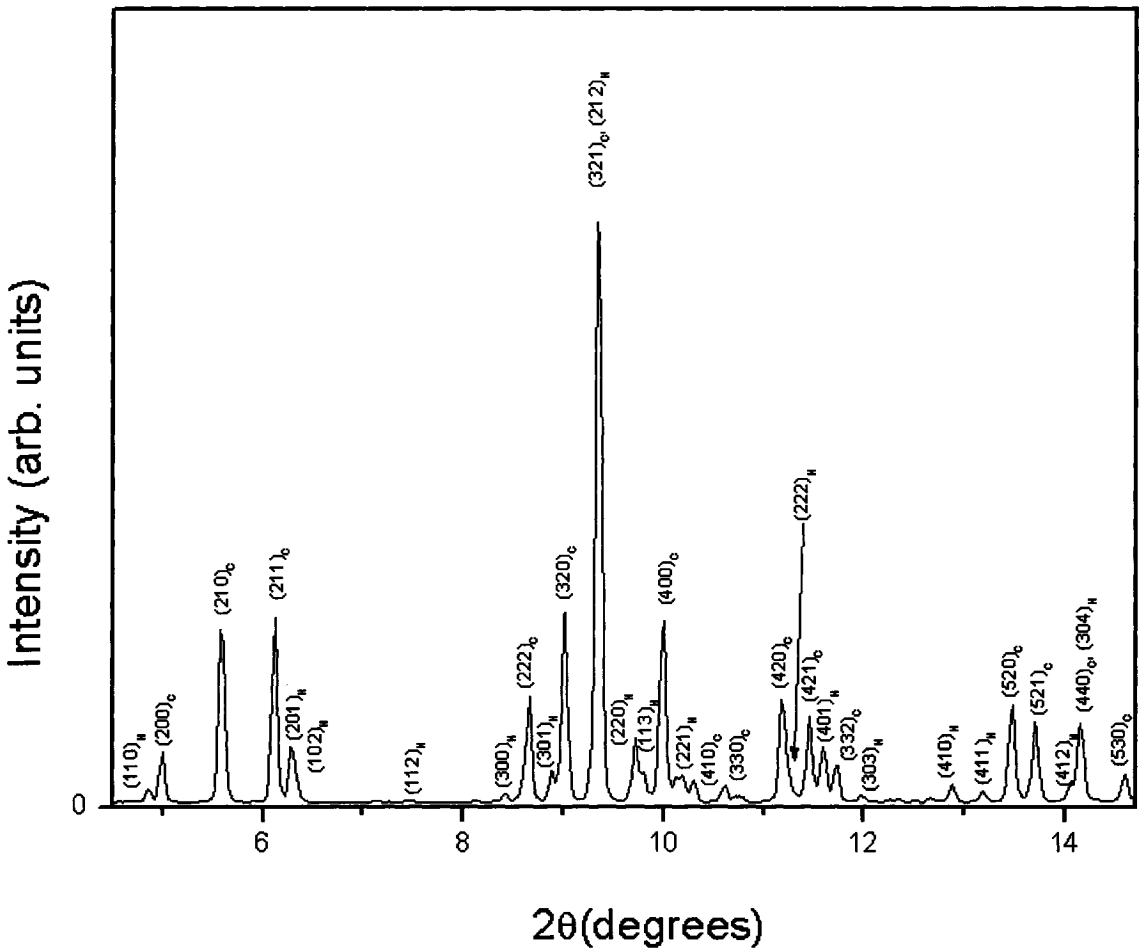

Figure 4.8. Integrated X-ray diffraction pattern of Xe hydrate at 1.98 GPa with background (baseline) subtracted. Peaks are labeled with their (*hkl*) indices, and subscripts "C" and "H" denote the cubic (sI) and hexagonal (sH) phases, respectively.

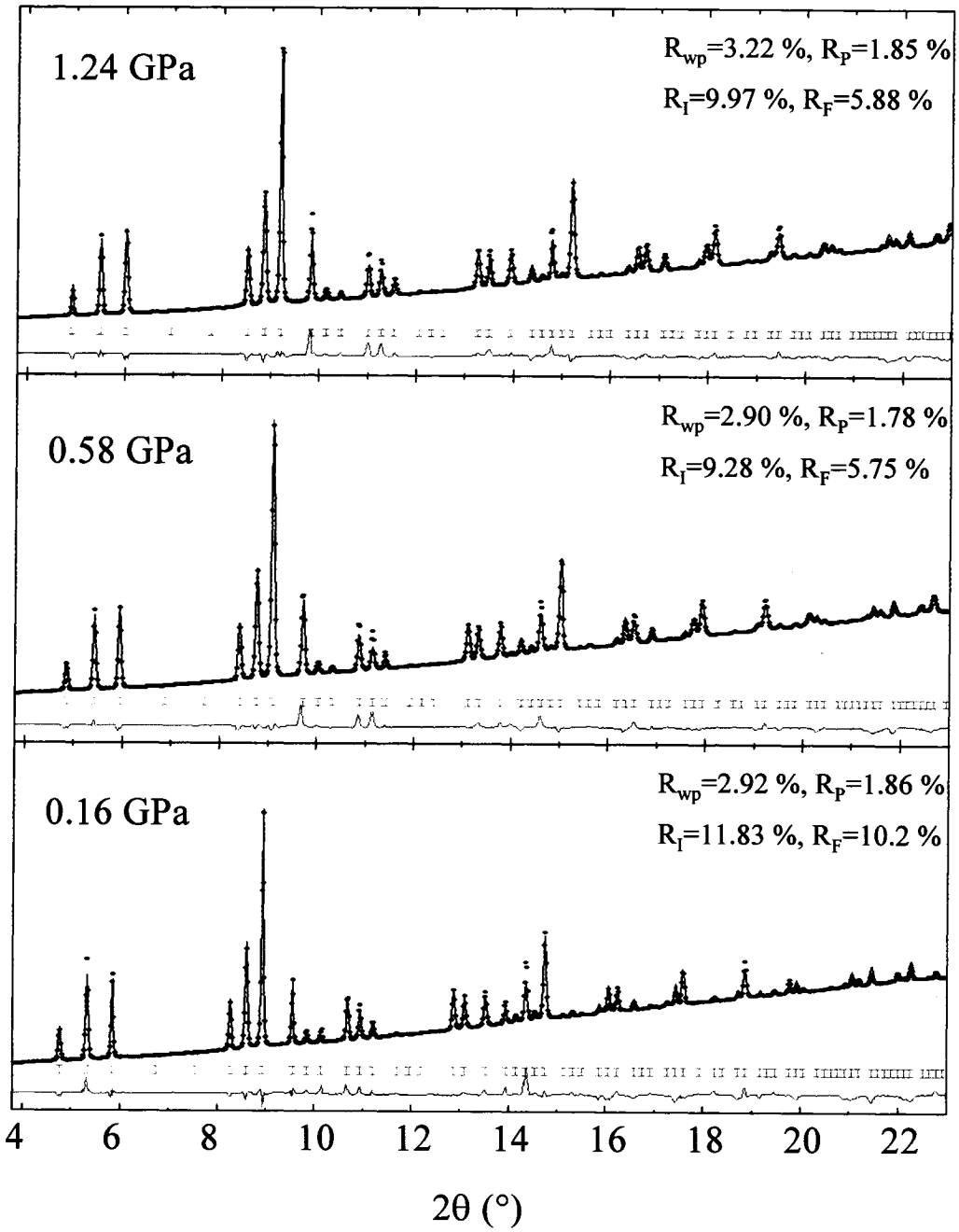

Figure 4.9. X-ray powder diffraction patterns of sI $Xe_8(H_2O)_{46}$ at different pressures. The dot symbols denote the experimental data; the solid line, the calculated pattern obtained from the Rietveld refinement; tick marks the calculated peak positions; the bottom curve represents the difference between observed and calculated patterns. The goodness-of-fit parameters resulted from the Rietveld analysis are shown for each pattern.

The parameters varied during the Rietveld refinements were: scale, profile function parameters, background, lattice parameter, guest atom occupancies, and atomic coordinates for the oxygen atoms that are not located at special positions. All those parameters were given the same weight during the refinement procedure. Even though well resolved X-ray diffraction peaks were recorded down to small *d*-spacings (around 1.1 Å), the number of X-ray diffraction peaks was too small for extracting any meaningful atomic thermal factors. Consequently, all atomic thermal factors were kept fixed at reasonable values during the refinements. The profile function used in the analysis was Pseudo-Voigt, as presented in Chapter I. Figure 4.9 presents the experimental and calculated diffraction patterns of sI Xe hydrate at various pressures at room temperature.

The lattice parameter, atomic positions, and site occupancy values obtained for Xe hydrate from the Rietveld analysis are showed in Table 4.1. The error associated with each parameter corresponds to that reported by RIETAN.

Pressure	Lattice	x	y	z	Occupancy	
(GPa)	Param. (Å)	O (*16i*)	O (*24k*)	O (*24k*)	Xe- *L*	Xe-*S*
0.16	11.911(1)	0.1815(8)	0.306(1)	0.120(1)	0.81(1)	0.756(8)
0.58	11.6960(7)	0.1878(6)	0.304(1)	0.1169(8)	0.758(8)	0.660(6)
1.24	11.5591(8)	0.1898(6)	0.3087(9)	0.1203(8)	0.750(8)	0.672(5)

Table 4.1. Lattice parameter, fractional coordinates of the oxygen atoms, and cage occupancies of sI xenon hydrate at different pressures. Xe-*L* and Xe-*S* denote xenon atoms in large and small cages, respectively.

While the position of O *(24k)* seems to not change with pressure, there is a tendency to increase observed for the atomic coordinate of O *(16i)* which translates to smaller distances in between these atoms. Also, cage occupancies, for both types of

cages, appear to slightly decrease with pressure. Unfortunately, this result cannot be confirmed as the excess Xe that would result from the decrease of cage occupancies would be difficult to detect from the XRD data. It should be noted that X-ray diffraction lines from solid Xe overlap with those arising from the sI sample.

As the *O(16i)*-O*(16i)* bond is only part of the large cages, the consistent decreasing trend of its length raises the question of whether or not the two different types of cages respond to the applied pressure in different ways. Table 4.2 presents relevant dimensions of the small and large cages as a function of pressure.

Pressure (GPa)	Small Cage Diameter (Å)	Large Cage Dimensions (Å)	
		Distance between the hexagonal planes (Å)	The longest "diameter" (Å)
0.16	7.828	5.955	9.061
0.58	7.635	5.848	8.960
1.24	7.658	5.779	8.778

Table 4.2. sI Xe hydrate cage dimensions for all three pressure points recorded in this experiment. The errors in bond lengths are about ±0.002 Å.

Over the experimental pressure range, the lattice parameter has decreased by 2.9%. Similar variations were observed for both small and large cages: a 2.1% decrease for the small cage diameter and 3.1% and 2.9% changes in the long and small axes of the large cavity, respectively. These values suggest that the large cages are affected by the applied increasing pressure to a slightly larger extent that the small cages. Since the small cages "survive" the phase transition to the next high pressure phase, sH, one could argue that this type of cage is more stable with pressure that the large cages. Having this in mind, this finding is not unexpected.

Changes induced by pressure in the host lattice may become more understandable after an inspection of the geometry of the cage building polygons: three types of polygons are present in the structure, i.e., two non-planar pentagons (called A

and B) and a planar hexagon. The small cages (5^{12}) are formed by twelve pentagons of type A, while the large cages ($5^{12}6^2$) are formed by four pentagons of type A, eight pentagons of type B and two hexagons (Figure 4.1). All dimensions of these three polygons were measured and their evolution with pressure is presented in Tables 4.3, 4.4, and 4.5. Tables 4.3, 4.4, and 4.5 present the bond angles and lengths of the hexagon, pentagon A, and pentagon B, respectively, for sI Xe hydrate. Figures 4.10, 4.11, and 4.12 illustrate the O-O bonds lengths and angles reported in Tables 4.3, 4.4, and 4.5.

Pressure (GPa)	**Angle (°)**		**Bond Length (Å)**	
	Bond O(*2*)-O(*3*)-O(*2*)	Bond O(*3*)-O(*2*)-O(*2*)	Bond O(*2*)-O(*3*)-O(*2*)	Bond O(*3*)-O(*2*)-O(*2*)
0.16	112.2	123.9	2.784, 2.784	2.784, 2.850
0.58	111.5	124.3	2.763, 2.763	2.763, 2.736
1.24	111.7	124.1	2.672, 2.672	2.672, 2.781

Table 4.3. Bond angles and lengths in the hexagonal plane forming the large cages of sI Xe hydrate. The errors of the bond angles are about ±0.1° and the errors of the bond lengths about ±0.002 Å.

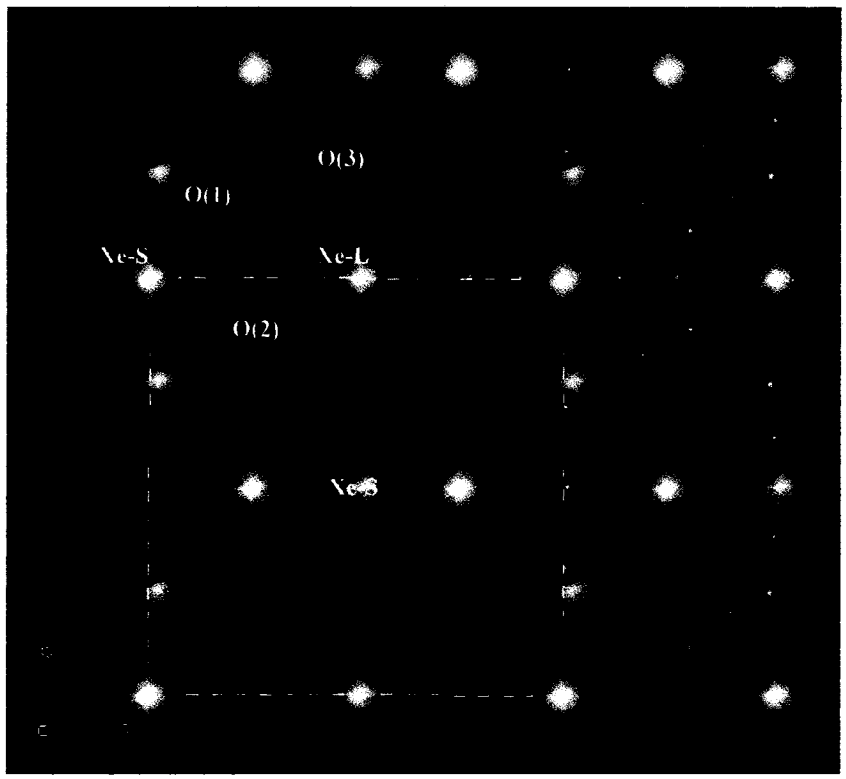

Figure 4.10. sI Xe clathrate hydrate. The black lines indicate the bond lengths and define the angles characteristic for the hexagonal face of the large cages, presented in Table 4.3. The small spheres represent O(1) atoms, medium size spheres the O(2) atoms, large spheres the O(3) atoms, and the gray spheres the Xe atoms. The dotted lines mark the limits of one unit cell.

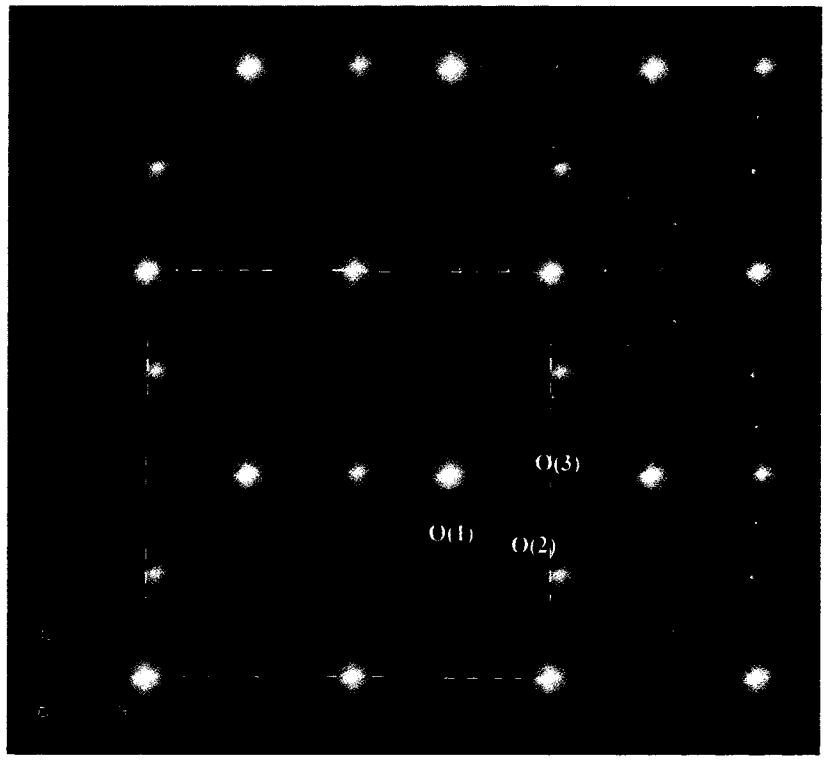

Figure 4.11. sI Xe clathrate hydrate. The black lines mark the bond lengths and define the angles characteristic for the pentagonal face B of the large cages, presented in Table 4.4. The positions of atoms are marked in the same way as in Figure 4.10.

Pressure (GPa)	**Angle (°)**			**Bond Length (Å)**		
	Bond O(*2*)-O(*3*)-O(*2*)	Bond O(*1*)-O(*2*)-O(*3*)	Bond O(*2*)-O(*1*)-O(*1*)	Bond O(*2*)-O(*3*)-O(*2*)	Bond O(*1*)-O(*2*)-O(*3*)	Bond *O(1)*-O(*1*)-O(*2*)
0.16	108.1	107.5	107.4	2.784, 2.784	2.723, 2.784	2.828, 2.723
0.58	108.5	104.1	110.6	2.763, 2.763	2.717, 2.763	2.519, 2.717
1.24	108.4	104.7	110.2	2.672, 2.672	2.710, 2.672	2.412, 2.710

Table 4.4. Bond angles and lengths in the pentagon B face forming the large cages of sI Xe hydrate. The errors of the bond angles are about ±0.1° and the errors of the bond lengths about ±0.002 Å.

Pressure (GPa)	**Angle (°)**			**Bond Length (Å)**		
	Bond O(*1*)-O(*2*)-O(*1*)	Bond O(*2*)-O(*1*)-O(*2*)	Bond O(*2*)-O(*2*)-O(*1*)	Bond O(*1*)-O(*2*)-O(*1*)	Bond O(*2*)-O(*1*)-O(*2*)	Bond O(*2*)-O(*2*)-O(*1*)
0.16	105.1	111.4	105.7	2.723, 2.723	2.723, 2.723	2.850, 2.723
0.58	107.9	108.3	107.8	2.717, 2.717	2.717, 2.717	2.736, 2.717
1.24	108.1	108.7	107.2	2.710, 2.710	2.710, 2.710	2.781, 2.710

Table 4.5. Bond angles and lengths in pentagon A face forming the small cages of sI Xe hydrate. These faces are also shared by the large cages. The errors of the bond angles are about ±0.1° and the errors of the bond lengths about ±0.002 Å.

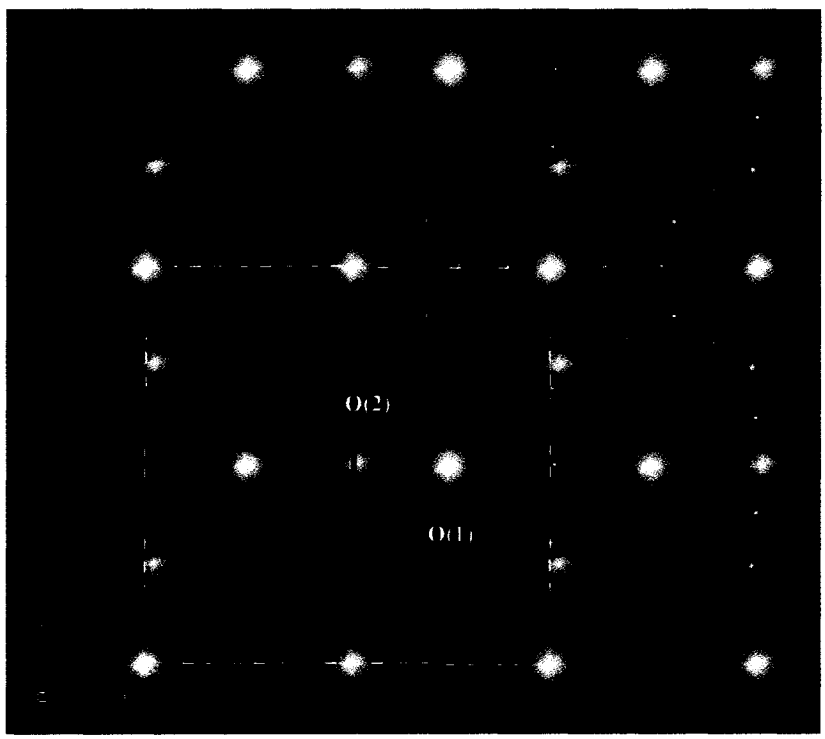

Figure 4.12. sI Xe clathrate hydrate. The black lines mark the bond lengths and define the angles characteristic for the pentagonal face A of the small cages, presented in Table 4.5. The positions of atoms are marked in the same way as in Figures 4.10. and 4.11.

As seen in Tables 4.3, 4.4, and 4.5, all bond lengths are decreasing with the increasing pressure. The largest change appears in the O*(16i)*-O*(16i)* bond length. A 15% decrease is observed for the bond length, while all the other bond lengths are decreasing by less than 3%. As the pressure is increased, changes of up to 3% are observed in the bond angles, translating in small distortions of both cages' geometries.

4.2.2 Krypton Hydrate

Several experimental runs were performed to study the structural transitions induced by high pressure in the krypton hydrate. Results of two experiments are presented in this section. The first experiment (run #1) proved to be very useful for the determination of the sequence of phases. In run #1 (Figure 4.13), one low pressure sII (Figure 4.14), two sI, and one sH (Figure 4.15) X-ray diffraction patterns were recorded as the pressure was increased. In the second experiment (run #2), three high-quality patterns of sI Kr hydrate were recorded (Figure 4.16). It should be noted that significant errors in the measured pressures in run #2 are suspected due to the following reasons: all of our runs, except for run #2, showed that sII occurs at low pressures, and transforms to sI at approximately 0.40 GPa; also, in a previous Raman spectroscopy study on Kr hydrate, Sasaki *et al.* [4] reported that the sII-sI phase transition takes place around 0.58 GPa. However, the diffraction patterns collected in run#2 will be used in the Rietveld/MEM analysis, due to their high quality. The probable errors in the pressure values will be taken into consideration when discussing the results.

In contrast to xenon clathrate hydrate, at low pressure and room temperature, krypton clathrate hydrate crystallizes in the cubic, sII structure. As pressure increases, a structural transition to the sI phase takes place. With further increase of pressure, sH structure is observed, as in the case of Xe hydrate. The low Bragg angle region of the integrated X-ray diffraction patterns collected at pressures in the 0.05-0.74 GPa range are presented in Figure 4.13.

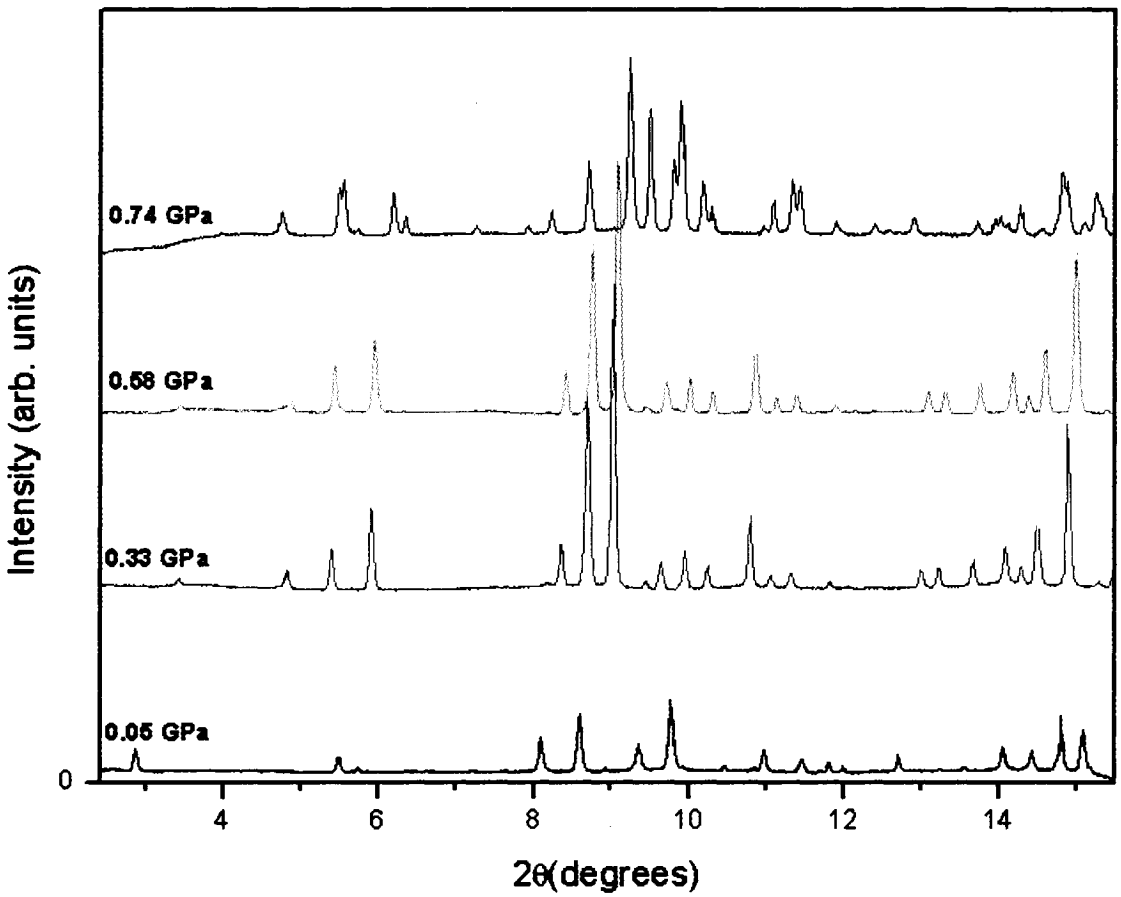

Figure 4.13. Integrated X-ray diffraction patterns of krypton hydrate as a function of pressure. sII (0.05 GPa), sI (0.33 and 0.58 GPa) and sH (0.74 GPa) phases can be observed. A background subtraction was performed for all four patterns.

Figure 4.14 presents in greater detail the Kr hydrate X-ray diffraction pattern collected at the lowest pressure in the experiment, i.e., 0.05 GPa. The Bragg reflections observed are indexed to the cubic sII phase.

At 0.74 GPa, all X-ray diffraction lines are rising from the sH Kr hydrate phase (Figure 4.15).

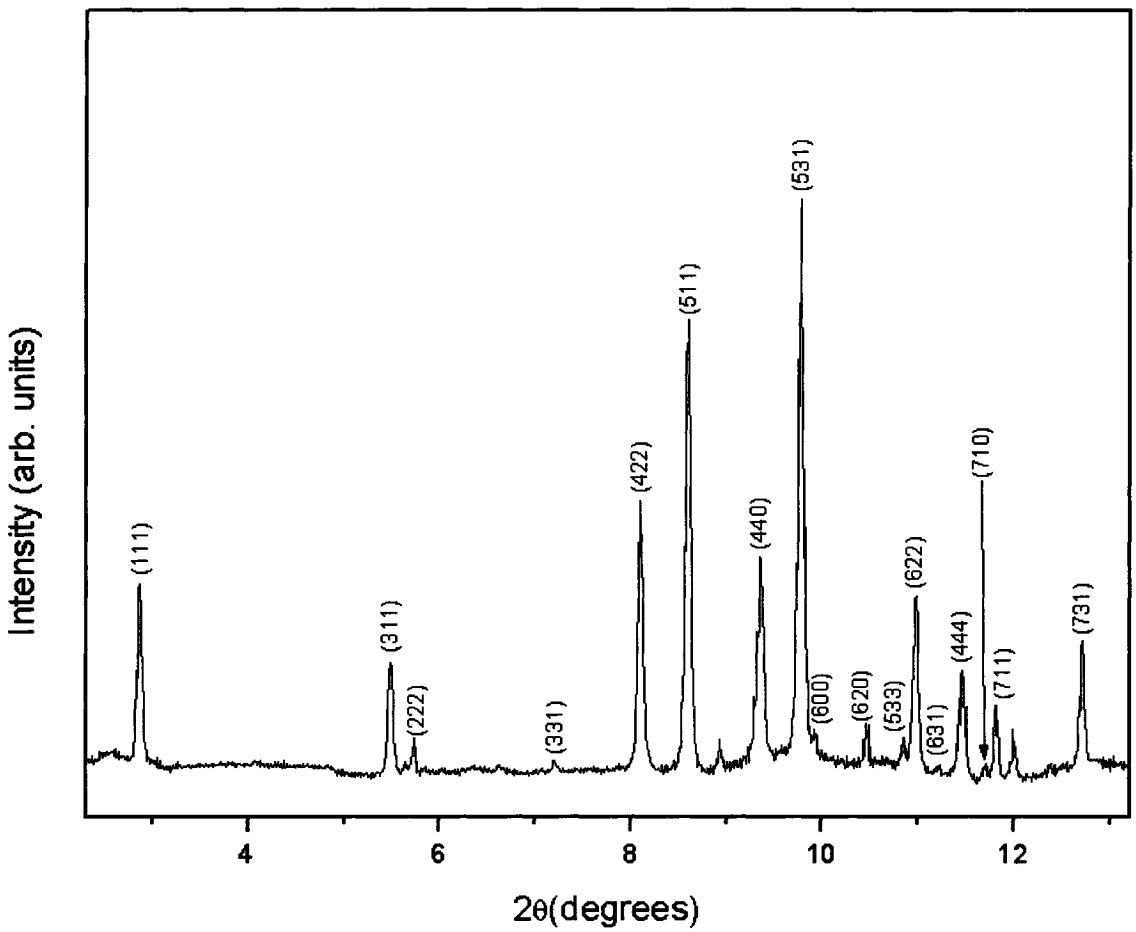

Figure 4.14. The low-angle range of the X-ray diffraction integrated pattern of sII Kr hydrate at 0.05 GPa, with background subtraction.

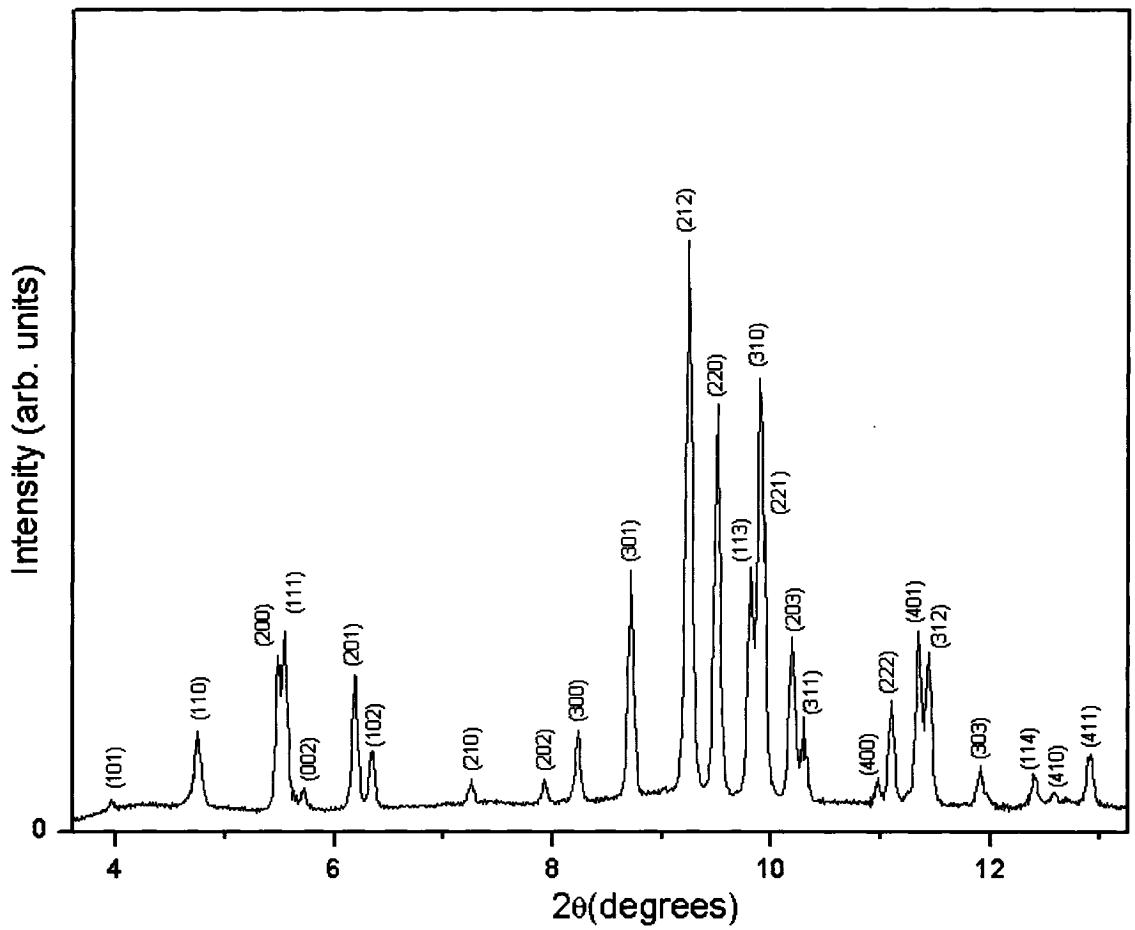

Figure 4.15. The low angle range of the background subtracted X-ray diffraction integrated pattern of sH Kr hydrate at 0.74 GPa.

The Rietveld analysis was carried out for three single phase sI X-ray diffraction patterns of Kr hydrate collected in run #2. The same parameters as for the Rietveld analysis performed in the case of Xe hydrate were varied: scale, profile function parameters, background, lattice parameter, guest atom occupancies, and atomic coordinates for the oxygen atoms not located at special positions. The corresponding refinement plots for each pressure point are shown in Figure 4.16. Reflections up to $\sin(\theta)/\lambda$ equal to 0.348, 0.328, 0.373 $Å^{-1}$ for the patterns measured at 0.05, 0.16 and 0.36 GPa, respectively, were considered in the Rietveld and MEM/MPF analysis.

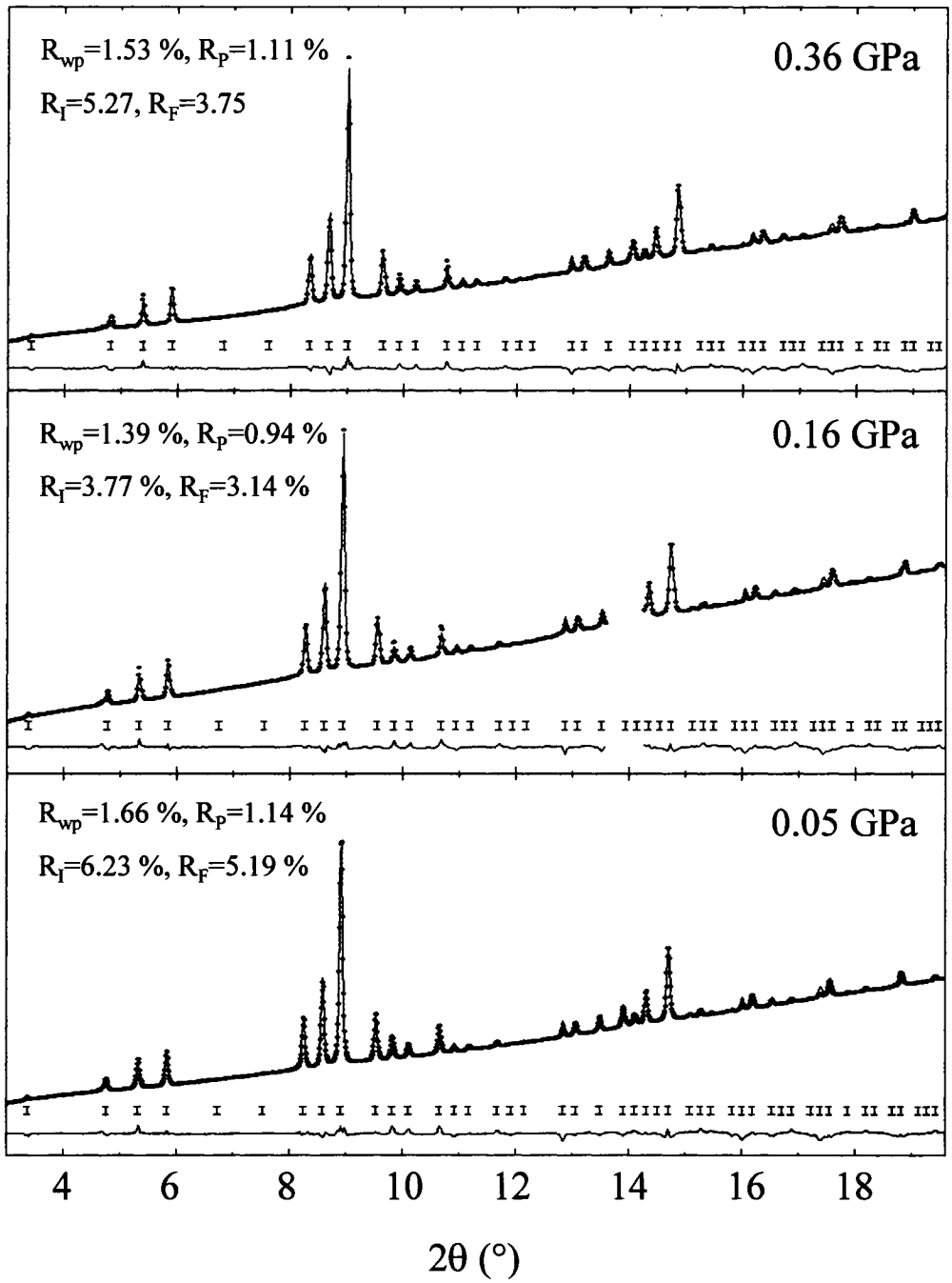

Figure 4.16. X-ray powder diffraction patterns of sI $Kr_8(H_2O)_{46}$ recorded at different pressures. The dot symbols denote the experimental data; the solid line, the calculated pattern; tick marks the calculated peak positions; the bottom curve represents the difference between observed and calculated patterns. The goodness-of-fit parameters resulted from the Rietveld analysis are shown for each pattern.

Tables 4.6, 4.7, 4.8, 4.9, and 4.10 present the values of the atom coordinates, cage occupancies, cage dimensions, and O-O bond angles and lengths as obtained from the Rietveld refinement for each pressure point. Figures 4.10, 4.11, and 4.12 present the O-O bonds forming the hexagonal, pentagon B, and pentagon A faces of the large and small cages. These are also relevant for the bond length and angle values listed in Tables 4.8, 4.9, and 4.10, respectively.

Pressure (GPa)	Lattice Param. (Å)	x O (*16i*)	y O (*24k*)	z O (*24k*)	Occupancy	
					Kr- *L*	Kr-*S*
0.05	11.937(1)	0.1858(4)	0.3117(5)	0.1187(4)	0.772(5)	0.675(3)
0.16	11.908(1)	0.1849(5)	0.3111(7)	0.1185(6)	0.791(9)	0.689(5)
0.36	11.826(1)	0.1856(5)	0.3117(6)	0.1195(5)	0.780(7)	0.682(5)

Table 4.6. Lattice parameter, fractional coordinates of the oxygen atoms, and cage occupancies of sI krypton hydrate at different pressures. Kr-*L* and Kr-*S* denote krypton atoms in large and small cages, respectively.

Pressure (GPa)	Small cage diameter (Å)	Large Cage Dimensions (Å)	
		Distance between the hexagonal planes	The largest "diameter"
0.05	7.950	5.968	9.102
0.16	7.927	5.954	9.086
0.36	7.896	5.913	9.001

Table 4.7. The small cage diameter and the smallest distance (between the hexagonal planes) and largest dimensions of the large cages of Kr hydrate at three different pressures. The errors in bond lengths are about ±0.002 Å.

Pressure (GPa)	**Angle (°)**		**Bond Length (Å)**	
	Bond O(*2*)-O(*3*)-O(*2*)	Bond O(*3*)-O(*2*)-O(*2*)	Bond O(*2*)-O(*3*)-O(*2*)	Bond O(*3*)-O(*2*)-O(*2*)
0.05	110.4	124.8	2.745, 2.745	2.745, 2.834
0.16	110.3	124.8	2.741, 2.741	2.741, 2.821
0.33	110.5	124.7	2.709, 2.709	2.709, 2.826

Table 4.8. Bonds angles and lengths in the hexagonal plane forming the large cages of Kr hydrate, as a function of pressure. The errors of the bond angles are about ±0.1° and the errors of the bond lengths about ±0.002 Å.

Pressure (GPa)	**Angle (°)**			**Bond Length (Å)**		
	Bond O(*2*)-O(*3*)-O(*2*)	Bond O(*1*)-O(*2*)-O(*3*)	Bond O(*2*)-O(*1*)-O(*1*)	Bond O(*2*)-O(*3*)-O(*2*)	Bond O(*1*)-O(*2*)-O(*3*)	Bond O(*1*)-O(*1*)-O(*2*)
0.05	109.0	105.9	108.5	2.745, 2.745	2.795, 2.745	2.795, 2.641
0.16	109.0	106.3	108.0	2.741, 2.741	2.780, 2.741	2.780, 2.688
0.33	108.9	106.4	108.0	2.709, 2.709	2.766, 2.709	2.766, 2.640

Table 4.9. Bonds angles and lengths in the pentagon B face forming the large cages of Kr hydrate. The errors of the bond angles are about ±0.1° and the errors of the bond lengths about ±0.002 Å.

Pressure (GPa)	Angle (°)			Bond Length (Å)		
	Bond O(*1*)-O(*2*)-O(*1*)	Bond O(*2*)-O(*1*)-O(*2*)	Bond O(*2*)-O(*2*)-O(*1*)	Bond O(*1*)-O(*2*)-O(*1*)	Bond O(*2*)-O(*1*)-O(*2*)	Bond O(*2*)-O(*2*)-O(*1*)
0.05	105.3	110.4	106.7	2.795, 2.795	2.795, 2.795	2.834, 2.795
0.16	104.7	110.9	106.5	2.780, 2.780	2.780, 2.780	2.821, 2.780
0.33	105.0	110.9	106.4	2.766, 2.766	2.766, 2.766	2.826, 2.766

Table 4.10. Bond angles and lengths in the pentagon A face forming the small cages of the Kr hydrate. These faces are also shared by the large cages. The errors of the bond angles are about ±0.1° and the errors of the bond lengths about ±0.002 Å.

As opposed to Xe hydrate, no significant changes have been found in the atom positions, cage occupancies, or cage geometry of the krypton hydrate as the pressure is increased. Only slightly (less than 1%) decreasing trends are observed in the lattice parameter and cages dimensions values. Also, the bond angles and lengths are very similar with the ones reported for the methane hydrate at 2 K [1]. Even though the measurements on the Kr and methane hydrates were performed at different pressure – temperature conditions, a comparison between the two sets of data may be relevant, considering that the diameter of the Kr atom (4.0 Å) is very close to the diameter of the relatively small methane molecule (4.3 Å).

The analysis of X-ray diffraction data by MEM can provide very important and interesting insights on structural properties of various compounds (as detailed in Chapter II), beyond the reach of the Rietveld analysis. The application of this model-independent method of extracting charge density distributions from the XRD data was pursued for the case of sI Xe and Kr hydrates. This is the object of the next section.

4.3 Charge Density Distributions Derived from the MEM Analysis of sI Kr and Xe Hydrates

To extract the charge density distributions directly from our powder X-ray diffraction data, we used the Maximum Entropy Method (MEM) in conjunction with the Rietveld refinement and MEM-based Pattern Fitting (MPF) methods. These methods and the software used are described in detail in Chapter II.

The MEM calculations were always initiated from a uniform prior density distribution, resulting from dividing the total number of electrons in the unit cell (note: the cage occupancies provided by the initial Rietveld refinement were taken into account) by the volume of the unit cell. Also, all MEM calculations were performed over a 64×64×64 pixel mesh representing the unit cell. The iterative MEM/MPF procedure was applied until the R_I factor, as defined in Chapter I, was minimized.

To our knowledge, our work presents the first study of changes induced by pressure in the electron charge density distribution of sI gas clathrate hydrates. Our results clearly show that the guest-host interaction differs significantly depending on the guest location, in the small or large cages, at high pressures.

4.3.1 Details of the MEM/MPF Analysis of Structure I Xenon Hydrate X-ray Diffraction Data

In the case of xenon hydrate, the MEM calculations were carried out based on 131, 129, and 108 X-ray reflections, extracted from the 0.16, 0.58, and 1.24 GPa X-ray diffraction patterns, respectively, out of which 42 reflections were non-overlapping in each pattern. After 2 MEM/MPF cycles the R_I goodness-of-fit parameter reached its minimum and the analysis was stopped for all three diffraction datasets. A significant improvement of the fit between the measured and calculated patterns is observed for all

three pressure points after the MEM/MPF cycles as illustrated in Figure 4.17 and listed in Table 4.11. A small Bragg angle range of the observed and calculated diffraction patterns at 1.24 GPa is presented in Figure 4.17, to better visualize the improvement of the fit.

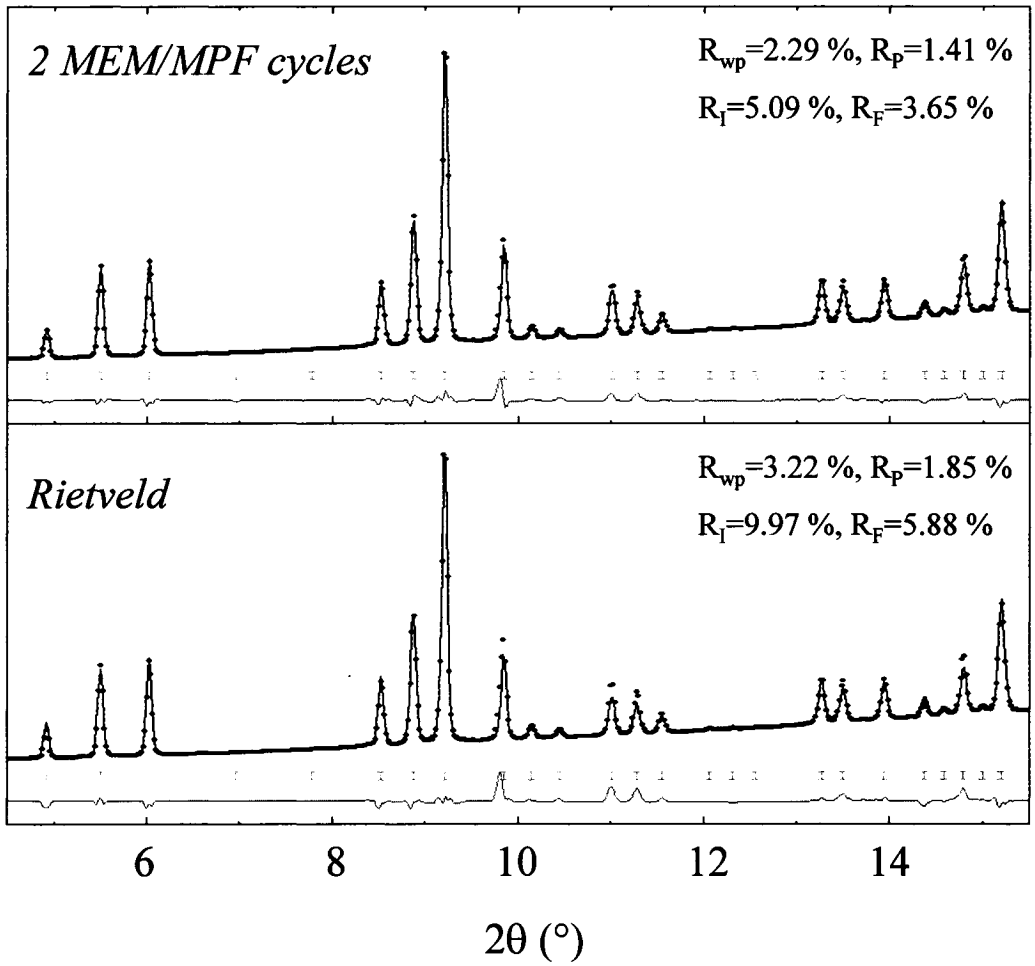

Figure 4.17. X-ray powder diffraction pattern of sI Xe hydrate at 1.24 GPa in the low Bragg angle range. The solid lines denote the calculated patterns using Rietveld analysis (lower panel) and MEM/MPF method (upper panel); the dot symbols denote the experimental data; tick marks the calculated peak positions; the bottom curve represents the difference between observed and calculated patterns.

The reliability (R) factors (defined in Chapter II) obtained from the MEM analysis for each pressure point are presented in Table 4.12.

Pressure (GPa)	**Goodness-of-Fit Parameters after the Rietveld Analysis (%)**	**Goodness-of-Fit Parameters after the 2 MEM/MPF Cycles (%)**
0.16	R_{wp}=2.92, R_P=1.86 R_I=11.83, R_F=10.2	R_{wp}=2.41, R_P=1.52 R_I=8.42, R_F=7.76
0.58	R_{wp}=2.90, R_P=1.78 R_I=9.28, R_F=5.75	R_{wp}=2.22, R_P=1.45 R_I=5.28, R_F=4.01
1.24	R_{wp}=3.22, R_P=1.85 R_I=9.97, R_F=5.88	R_{wp}=2.29, R_P=1.41 R_I=5.09, R_F=3.65

Table 4.11. Goodness-of-fit parameters resulting from the Rietveld analysis and 2 MEM/MPF cycles for all the sI Xe hydrate patterns recorded in the experiment.

Pressure (GPa)	**MEM Reliability Factors (%)**
0.16	R_{wF}=6.7, R_F=8.2
0.58	R_{wF}=3.6, R_F=3.9
1.24	R_{wF}=3.3, R_F=3.6

Table 4.12. Reliability factors resulting from the MEM analysis for all the sI Xe hydrate patterns recorded in the experiment.

4.3.2 Details of the MEM/MPF Analysis of Structure I Krypton Hydrate X-ray Diffraction Data

For the krypton hydrate, 68 (30 non-overlapping), 56 (30 non-overlapping), and 78 (33 non-overlapping) reflections extracted using the Rietveld method from the X-ray diffraction patterns collected at 0.05, 0.16 and 0.36 GPa, respectively, are used as constraints in the MEM calculations.

Pressure (GPa)	**Goodness-of-Fit Parameters after the Rietveld Analysis (%)**	**Goodness-of-Fit Parameters after the 2 MEM/MPF Cycles (%)**	**Reliability Factors (MEM) (%)**
0.05	R_{wp}=1.66, R_P=1.14 R_I=6.23, R_F=5.19	R_{wp}=1.47, R_P=0.95 R_I=3.67, R_F=3.20	R_{wF}=3.0, R_F=3.3
0.16	R_{wp}=1.39, R_P=0.94 R_I=3.77, R_F=3.14	R_{wp}=1.38, R_P=0.93 R_I=2.43, R_F=2.20	R_{wF}=1.1, R_F=1.0
1.36	R_{wp}=1.53, R_P=1.11 R_I=5.27, R_F=3.75	R_{wp}=1.46, R_P=1.04 R_I=3.70, R_F=2.99	R_{wF}=3.1, R_F=3.3

Table 4.13. Goodness-of-fit parameters resulting from the Rietveld analysis and MEM/MPF cycles for the Kr hydrate, and MEM reliability factors.

MEM/MPF cycles are performed to weaken the influence of the initial model used in the Rietveld refinement, until no significant improvement in the MPF fit (translated in minimum value for the R_I factor) was observed. The number of cycles after which R_I factor reached its minimum is 2 in the case of the 0.16 and 0.36 GPa patterns and 4 for the pattern recorded at 0.05 GPa.

The charge density distribution maps calculated in these cycles are the ones that give the best description of the experimental X-ray diffraction patterns and will be presented and discussed further in this chapter. Table 4.13 shows results which indicate the improvement of the fit to the measured Kr hydrate X-ray diffraction patterns as reflected in the goodness-of-fit parameters and the reliability factors for the MEM analysis at all pressures.

4.3.3 Charge Density Distribution Maps of sI Xe and Kr Hydrates

Charge density distribution maps of sI xenon hydrate at three different pressures available from the experiment are calculated following the procedure described in Chapter II for the MEM/MPF analysis.

Figure 4.18 displays the resulting charge density distribution maps in the (100) plane.

Figure 4.18. Contour plots of the charge density in the (100) plane of the $Xe_8(H_2O)_{46}$ unit cell, highlighting the Xe atom in the large cage. Contour lines are drawn from 0 to 2.0 *e*/ Å^3 at intervals of 0.1 *e*/ Å^3.

In this plane, the corners are occupied by Xe atoms, hosted by the small cages, while the Xe atoms in the large cages are situated at the (1/4, 1/2) fractional positions. Two parts of the hexagonal rings belonging to the large cages can be seen in the lower and upper part of the plane. This structure is formed by one oxygen atom O (*6c*) at (1/2, 1/4) and the two other oxygen atoms O (*24k*) located at (1/4, 1/8) and (3/4, 1/8), respectively.

The most noticeable feature in these plots is the distortion of the electron distribution of the Xe atom in the large cage from a spherical distribution. The charge density distribution is elongated along the large axis of the large cage (transverse axis) and, to a lesser extent, along the short (longitudinal) axis, for all pressures. Previous experimental and theoretical studies of Xe hydrate by inelastic X-ray scattering (IXS) [23] and inelastic incoherent neutron scattering (IINS) [24] reported three different vibrational frequencies attributed to the Xe guest atoms, two vibrations corresponding to atoms in the large cages and one to the atom inside the small cages. Moreover, the Xe vibrations in the large cages are found to be considerably larger than those in the small cages. Also, one low-wavenumber peak in the Raman spectrum (56 cm^{-1} at 296 K) [4] of methane hydrate is attributed to the translational vibration of the guest molecule in the host water cage; from theoretical calculations [25], the presence of the same peak has been predicted in other gas hydrates at lower wavenumbers.

(100)

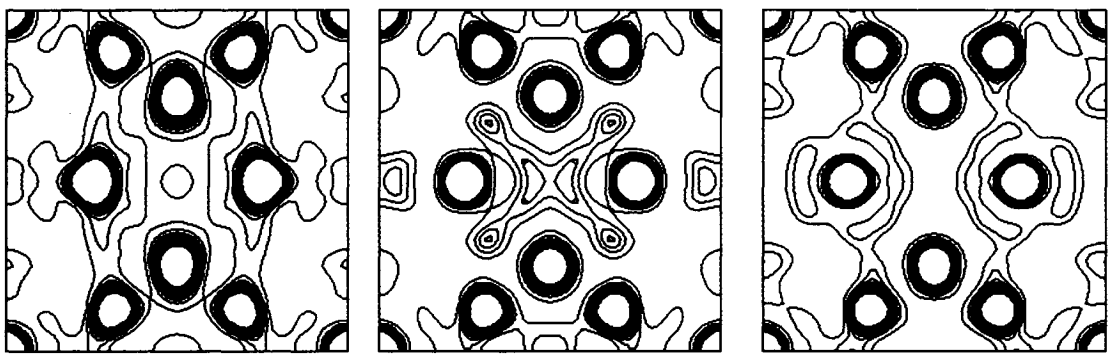

0.05 GPa 0.16 GPa 0.36 GPa

Figure 4.19. Contour plots of the charge density in the (100) plane of the sI Kr hydrate unit cell, highlighting the Kr atom in the large cage. Contour lines are drawn from 0 to 2.0 *e*/ $Å^3$ at intervals of 0.1 *e*/ $Å^3$.

Based on those previous observations, the anisotropic charge density distributions obtained in the present MEM calculations can be interpreted as a temporal average of the fluctuating position of Xe atoms in the large cages. Thus, these charge density distributions, reconstructed by MEM, imply that there is a preferential translational motion of the Xe atoms along the largest axis of the large cage.

As pressure increases, the electronic distribution of oxygen atoms forming the large cage appears to become more diffuse. Also the distance between these atoms becomes shorter. This finding is in agreement with our Rietveld results on the O-O bond lengths.

A similar distortion from the spherical symmetry of the electronic distribution of the atoms hosted by the large cages can be observed in the krypton hydrate (Figure 4.19). In this case, however, the distribution is more pronounced along the axis between the two hexagonal faces of the large cage (the short axes of the cage) than along the transversal one, especially at higher pressure values. This behavior is in agreement with previous low- and room-temperature neutron diffraction studies of the scattering amplitude density distribution of deuterated methane hydrate [2, 26], which revealed the tendency for an elongation of the density distribution of methane in large cages of methane hydrate in the same direction as we are reporting for Xe and Kr hydrates.

As in the case of the Xe hydrate, the deviations from the spherical distribution observed in the oxygen atoms forming the large cages become less apparent as the pressure increases.

To visualize more clearly the electronic distribution of the atoms hosted by the small H_2O cages, the (200) plane, which cuts through the middle of the unit cell, is displayed in Figure 4.20 for the case of Xe and Kr hydrates. The xenon (Figure 4.20a) and krypton atoms (Figure 4.20b) in the small cage can be observed in the center of the density maps. In contrast to the behavior of atoms located in the large cages, charge density distribution of the atoms hosted in small cages is rather spherical and does not change with pressure, to the extend of the resolution of the analysis, for both Xe and Kr hydrates. A spherical distribution of the scattering amplitude density has also been

observed for the methane molecule in the small cages, as obtained by MEM applied to neutron diffraction data collected in the 7.7-116 K temperature range [2, 26].

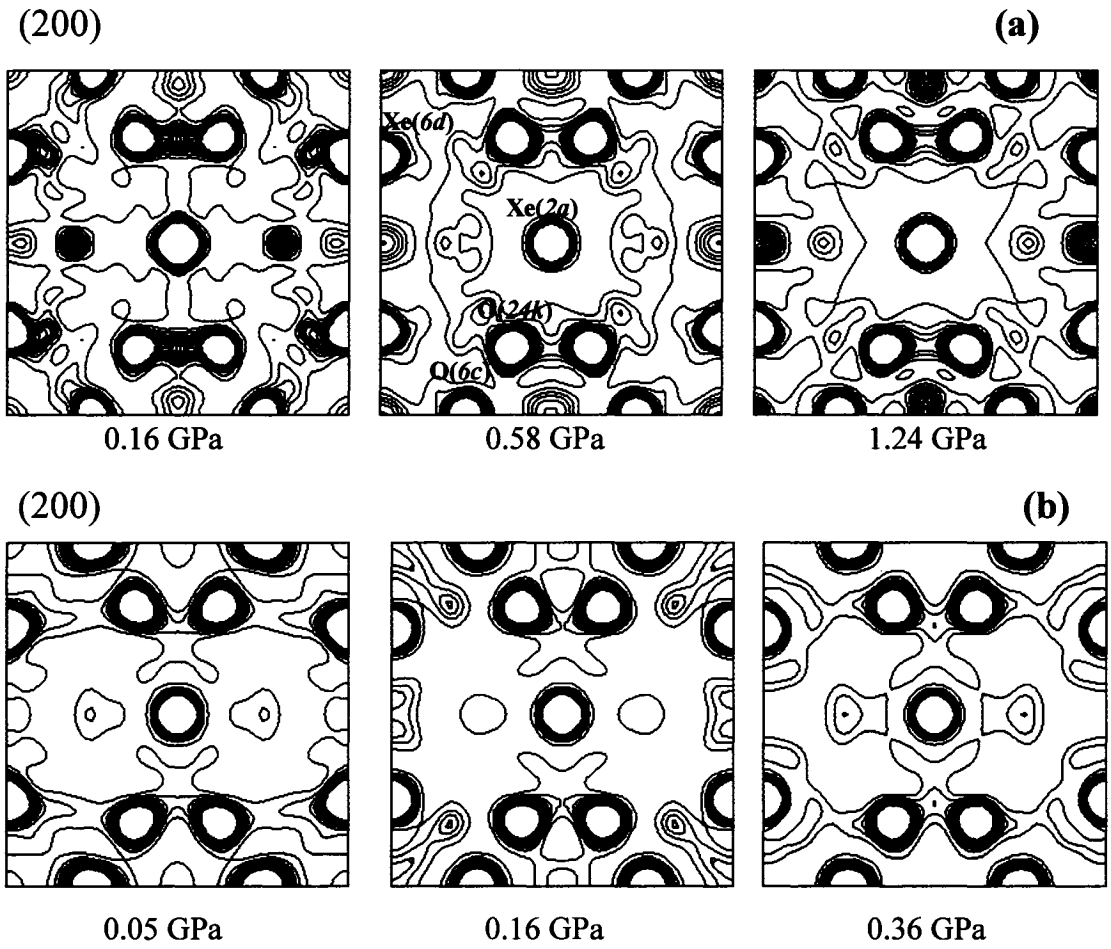

Figure 4.20. Contour plots of the charge density in the (200) plane of the (a) sI Xe hydrate and (b) Kr hydrate unit cell, highlighting the guest atoms of the small cage. Contour lines are drawn from 0 to 2.0 *e*/ Å^3 at intervals of 0.1 *e*/ Å^3.

Figures 4.21 (a) and (b) show the (110) plane for xenon and krypton hydrates, respectively. Besides the guest atoms in the small cages present in the center of the each density map, pairs of O(*16i*)-O(*16i*) bonds can also be visualized in Figure 4.21. Those bonds are part of pentagon B, forming the large cages. In the case of Xe hydrate, the electron distribution of the O(*16i*) atoms becomes more diffuse as the pressure is

increasing, a similar trend as the one observed for the oxygen atoms situated at the other sites in the unit cell. Moreover, the bond distance O(*16i*)-O(*16i*) decreases with pressure. No significant changes as a function of pressure can be observed in the O(*16i*) charge density distribution or bond length for the Kr hydrate.

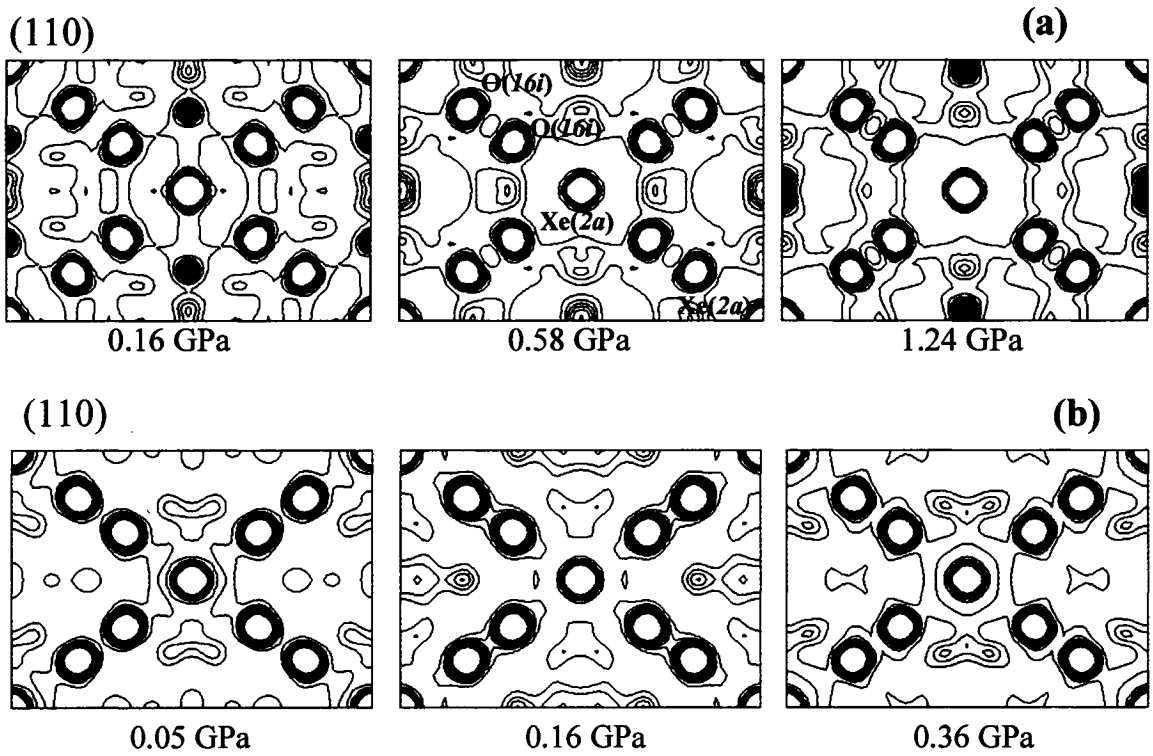

Figure 4.21. Contour plots of the charge density in the (110) plane of the sI (a) Xe hydrate and (b) Kr hydrate unit cell, highlighting the O-O bonds, part of the large cage, exclusively. Contour lines are drawn from 0 to 2 $e/Å^3$ at intervals of 0.1 $e/Å^3$.

These observations, regarding the changes in the electron density distributions of Xe and Kr sI phases as the pressure is increased, based only on the visualization of the density maps, can be validated by further examining of the charge density difference maps [$\Delta\rho = \rho(P) - \rho(0)$] between the calculated charge density at a given pressure, $\rho(P)$, relative to that at the lowest pressure, $\rho(0)$, as will be presented and discussed in the following subsection.

4.3.4 Difference Charge Density Distribution Maps of Structure I Xenon and Krypton Hydrates

In the present study, difference charge density distributions were computed relative to the lowest pressures, 0.16 GPa and 0.05 GPa, for Xe and Kr hydrates, respectively, by subtraction of the charge density at each grid point used in the MEM analysis. Therefore, the effect of volume reduction as a function of pressure was not taken into account, using, for instance, the equation of state.

Changes observed in the charge density distribution of the Xe atom in the large cages, relative to the distribution at 0.16 GPa, (Figure 4.22) suggest that this atom does not exhibit a uniform charge distribution and that the tendency of elongation along the transverse axis is increasing with pressure. Our observation is in agreement with the conclusions drawn from the examination of the absolute charge density distributions.

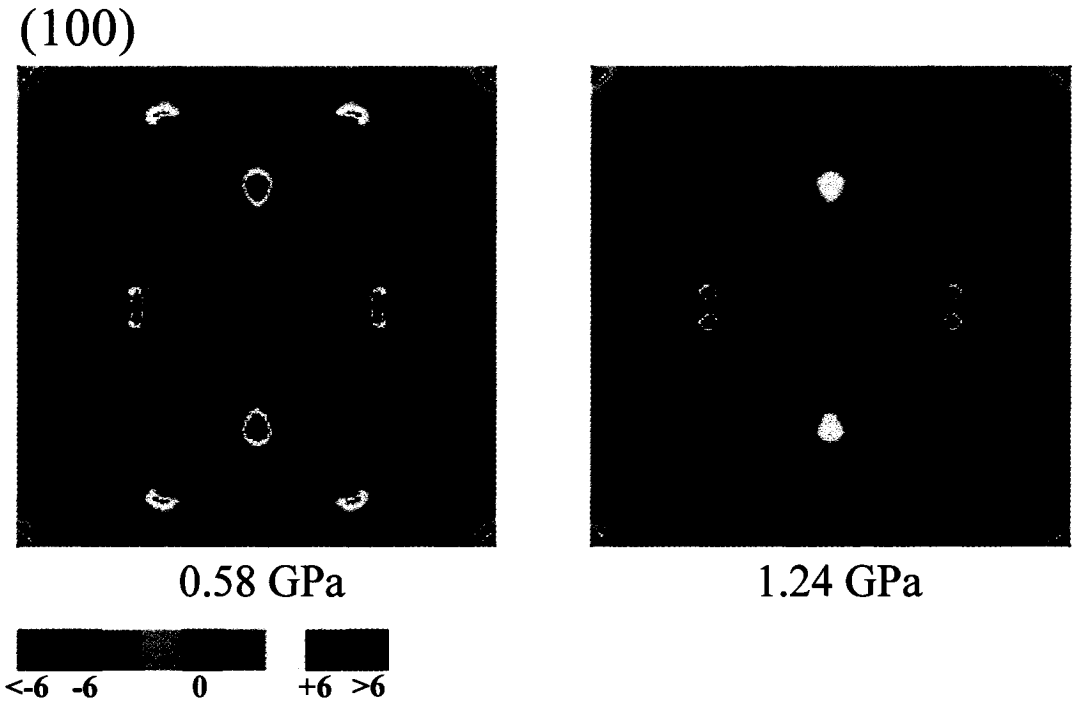

Figure 4.22. Plots of MEM charge density difference relative to 0.16 GPa, for the (100) plane of the sI Xe hydrate unit cell. Contour lines are drawn from –6.0 to 6.0 *e*/ Å^3 at intervals of 0.2 *e*/ Å^3.

The examination of the difference in charge density distributions in the (100) plane of the Kr hydrate unit cell (Figure 4.23) reveals that the electron distribution of Kr atoms in the large cages becomes more elongated in the longitudinal direction than in the transverse one, as the pressure is increasing.

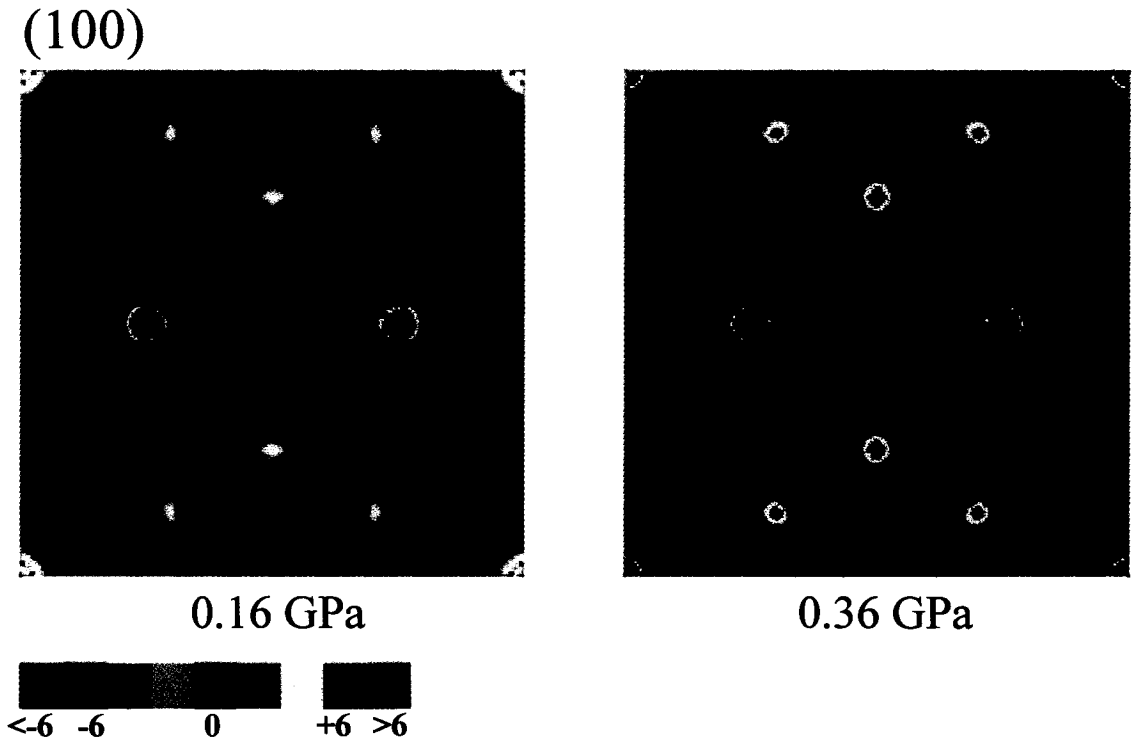

Figure 4.23. Plots of MEM charge density difference relative to 0.05 GPa, for the (100) plane of the sI Kr hydrate unit cell. Contour lines are drawn from –6.0 to 6.0 *e*/ Å^3 at intervals of 0.2 *e*/ Å^3.

The difference charge density distributions in the (200) plane shown in Figure 4.24 confirm the fact that the spherical electron distributions of guest atoms in small cages are not altered by the applied pressure. Also, as pressure increases, these atoms seem to gradually accumulate charge. Distortions in the electron distribution around the oxygen atoms occupying the *6c* and *24k* sites are also observed.

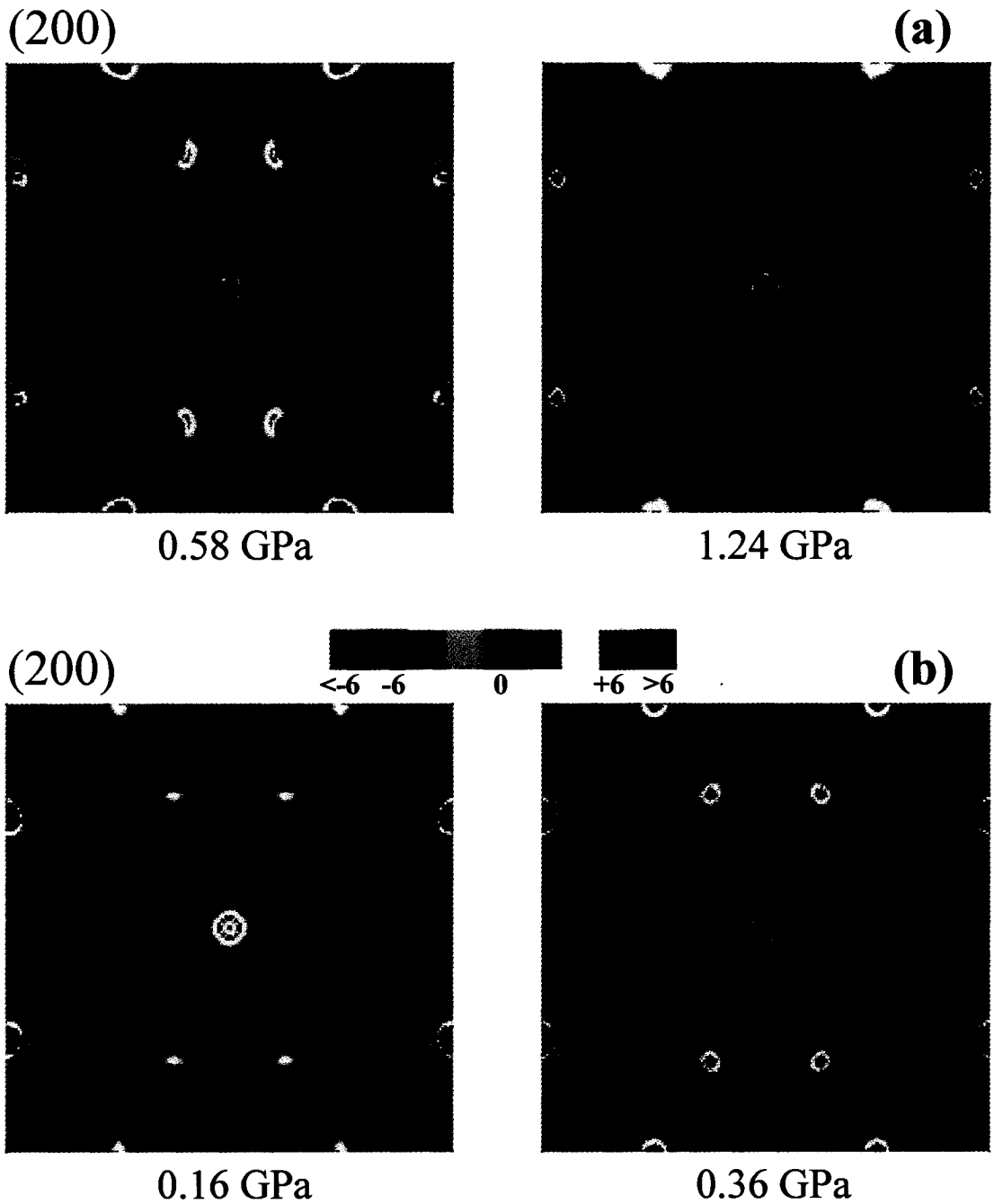

Figure 4.24. Plots of MEM charge density difference relative to 0.16 GPa and 0.05 GPa, respectively, for plane (200) of the sI (a) Xe hydrate and (b) Kr hydrate unit cells. Contour lines are drawn from –6.0 to 6.0 *e*/ Å^3 at intervals of 0.2 *e*/ Å^3.

Based on these observations, we can conclude that atoms located in the small cages are more susceptible to share electrons with the water molecules forming the cage framework, suggesting the existence of a stronger guest-host interaction in this type of cage. This conclusion was also reached in two previous studies of the xenon hydrate, namely, IINS [24] and molecular dynamics simulations [27]. At the same time, the relative changes in the electron distributions of the Xe/Kr atoms in large cages appear to be primarily related to changes in the amplitude of vibration in the transverse and longitudinal directions.

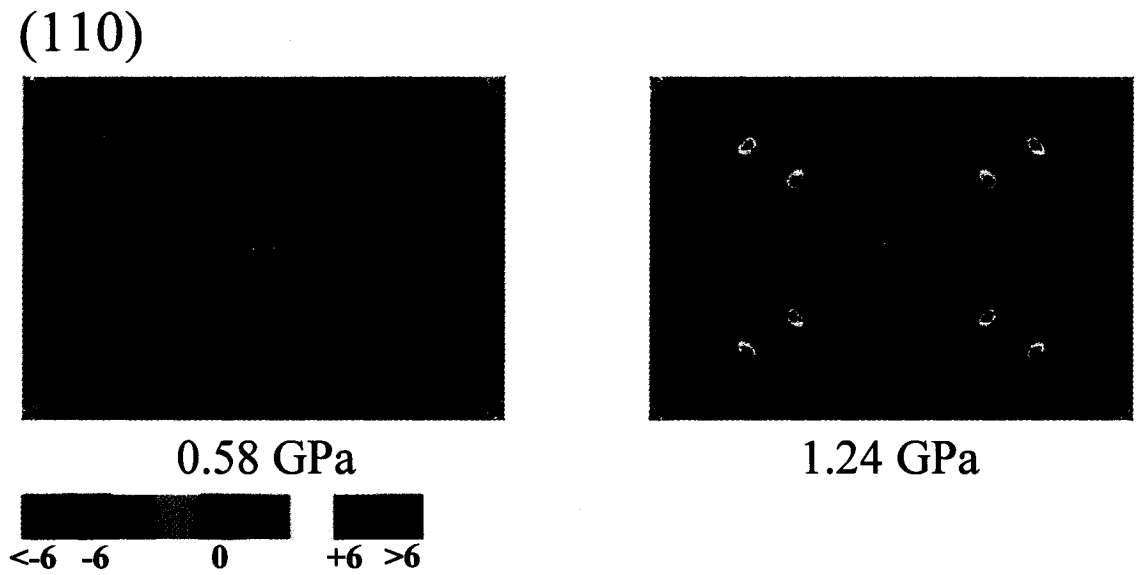

Figure 4.25. Plots of MEM charge density difference relative to 0.16 GPa, for plane (110) of the Xe hydrate unit cell. Contour lines are drawn from –6.0 to 6.0 *e*/ Å^3 at intervals of 0.2 *e*/ Å^3.

Figure 4.25 shows the changes in the charge density distribution of the O(*16i)* atoms, relative to the distribution calculated at 0.16 GPa for Xe hydrate. Especially for the 1.24 GPa distribution, the density map clearly reveals the change in the atom position, marked by blue and red regions. Even though the effect of volume reduction at higher pressures was not considered in the calculations of the difference charge density

distribution, it cannot account for these changes in the oxygen atom position, as similar shifts in the atomic charge density distributions were not observed for atoms occupying positions fixed by symmetry (i. e. O(*6c*), Xe/Kr(*2a*), Xe/Kr(*6d*)). It is clear that the oxygen atoms are gradually changing their position, getting closer as the pressure is increasing. This observation is in very good agreement with the O*(16i)* – O*(16i)* bond length values obtained from the Rietveld analysis and as presented in Table 4.4.

The gradual changes of the O*(16i)* atom position, induced by pressure, are only observed in the xenon hydrate. The charge density difference maps of Kr hydrate (Figure 4.26) show no significant changes in the oxygen atoms' position or electronic distribution.

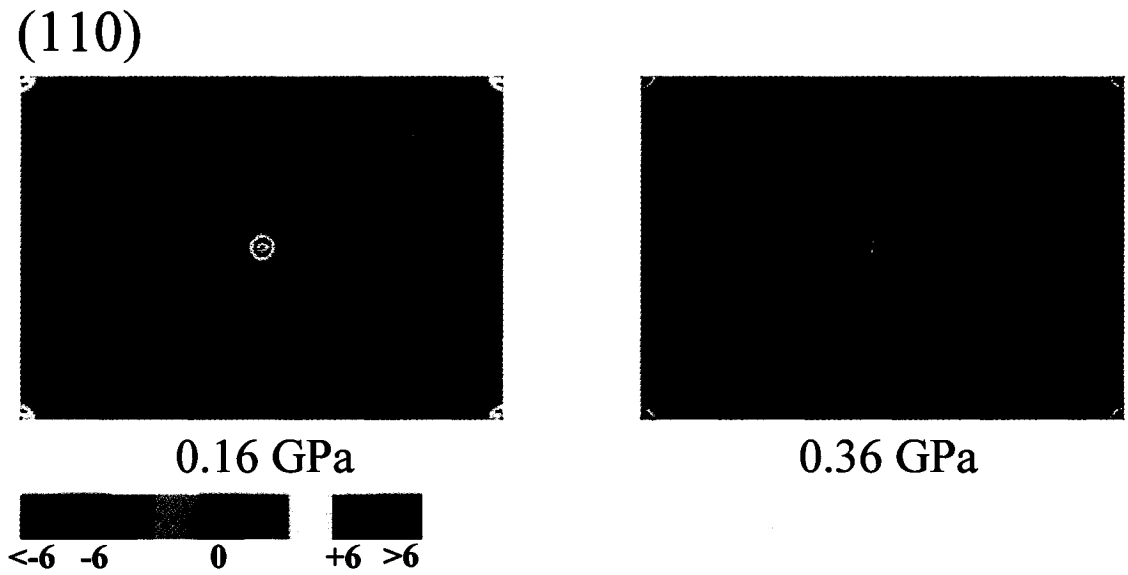

Figure 4.26. Plots of MEM charge density difference relative to 0.05 GPa, for plane (110) of the sI Kr hydrate unit cell. Contour lines are drawn from –6.0 to 6.0 *e*/ Å^3 at intervals of 0.2 *e*/ Å^3.

4.4 Summary and Conclusions

Synchrotron radiation powder X-ray diffraction experiments were performed to study the pressure induced phase transformations of Kr and Xe hydrates at room temperature. After clarifying the sequence of phase transitions for each of these compounds, we focused on the response of the sI phase to the applied pressure, from the point of view of the change of electronic density reconstructed from the Rietveld/MEM analysis.

For sI Kr hydrate, a slightly decreasing trend, as a function of increasing pressure, was observed for the lattice parameter and cages dimensions, but no significant changes were found in the atom positions and O-O bond angles and lengths from the Rietveld refinement. As significant errors in the pressure values are suspected, it is hard to know if sI Kr hydrate is, indeed, very stable with pressure, or if the pressure range over which our X-ray diffraction data were collected was too small to observe substantial changes.

In the case of sI Xe hydrate, consistent changes in the lattice parameter and cages geometry were observed, as assessed from the Rietveld refinement. In the 0.16-1.24 GPa pressure range (over which sI phase is stable) changes up to 3% were observed in the lattice parameter and O-O bonds angles and lengths. By far, the biggest change, i.e., 15%, was observed in the O*(16i)*-O*(16i)* bond length. This bond is a part of pentagon B, which is forming the large cages. This suggests that increasing pressure has a more substantial effect on the large cages than on the small ones. No significant changes have been observed in the atomic positions of O*(6c)* and O*(24k)*, but a clear increasing trend was found for the atom coordinate of O*(16i)*, translating into the decrease of the O*(16i)*-O*(16i)* bond length mentioned above. This observation was also confirmed by examining the charge density distributions obtained *via* MEM.

The close examination of the MEM calculated charge density distributions for the encaged guest atoms, correlated with the previous studies on the methane hydrate and xenon hydrate, is leading to several important conclusions. It is obvious that the thermal motions of the guest atoms differ between the small and the large cages. Spherical charge

density distributions were found for both the Xe and Kr atoms in the small cages at all pressures explored in this study. The same spherical scattering amplitude density distributions have been reported for methane hydrate at different low temperatures and pressure. In all three cases (Xe, Kr, and CH_4 hydrates), the density distributions of the atom/molecule in the large cages show significant distortions from the spherical symmetry, indicating preferential directions of vibration. As it has been suggested before for the case of methane hydrate [7], a strong correlation exists between the symmetry of the cage and the thermal motion isotropy of the guest atom/molecule. The high, almost spherical, symmetry of the small cage induces a highly isotropic motion for the atom/molecule encaged by it. Also, for the case of the atom/molecule in the large cages, it appears that, while the vibration amplitudes are higher for the Kr atoms and methane molecules along the direction of the short axis of the cage, larger amplitudes describing the motion of the Xe atoms are observed along the direction perpendicular to the short axis. These differences are probably related to the size of the guests, the Xe atom having a larger atomic/molecular radius than Kr or methane.

Keeping in mind that the pentagonal dodecahedron (small cage) can be also found in the next high-pressure phase (sH) that these three types of gas hydrates undergo, it is reasonable to speculate that the large translational vibrations observed for the guest atoms/molecule in the large cage, in junction with the decreasing dimensions of the cage, are leading to structural phase transition to the hexagonal structure. To confirm this idea, detailed neutron diffraction studies to show the influence of increasing pressure on the O-H bonds (inaccessible to an X-ray diffraction experiment) forming the cage structures would be needed. Also, single crystal diffraction experiments should be carried out to confirm the changes in oxygen atoms position and the cage occupancies observed in the present study.

References

1. C. Gutt, B. Asmussen, W. Press, M. R. Johnson, Y. P. Handa, and J. S. Tse, *J. Chem. Phys.* **113**, 4713 (2000).
2. A. Hoshikawa, H. Igawa, H. Yamauchi, Y. Ishii, *J. Chem. Phys.* **125**, 034505 (2006).
3. S. Desgreniers, R. Flacau, D. D. Klug, and J. S. Tse, *CeSMEC* (March 24-28, Florida, 2003).
4. S. Sasaki, S. Hori, T. Kume, and H. Shimizu, *J. Phys. Chem. B* **110**, 9838 (2006).
5. J. S. Loveday, R. J. Nelmes, D. D. Klug, J. S. Tse, and S. Desgreniers, *Can. J. Phys* **81**, 539 (2003).
6. J. S. Loveday, R. J. Nelmes, M. Guthrie, D. D. Klug, and J. S. Tse, *Phys. Rev. Lett.* **87**, 215501 (2001).
7. J. S. Loveday, R. J. Nelmes, M. Guthrie, S. A. Belmonte, D. R. Allan, D. D. Klug, J. S. Tse, and Y. P. Handa, *Nature* **410**, 661 (2001).
8. H. Hirai, T. Tanaka, T. Tawamura, Y. Yamamoto, and T. Yagi, *Phys. Rev. B* **68**, 172102 (2003).
9. Sloan, E. D. *Clathrate Hydrates of Natural Gases*, 2nd ed., Marcel Dekker, New York, 1998.
10. H. Davy, *Phil. Trans. Roy. Soc.* **101**, 1 (1811).
11. M. v. Stackelberg and H. R. Muller, *Z. Electrochem.* **58**, 25 (1954).
12. M. v. Stackelberg and H. R. Muller, *Z. Electrochem.* **62**, 130 (1958).
13. J. A. Ripmeester, J. S. Tse, C. I. Ratcliffe, and B. M. Powell, *Nature* **325**, 135 (1987).
14. R. K. McMullan and G. A. Jeffrey, *J. Chem. Phys.* **42**, 2725 (1965).
15. C. A. Perottoni and J. A. H. da Jornada, *J. Phys.* **13**, 5981 (2001).
16. T. C. W. Mak and R. K. McMullan, *J. Chem. Phys.* **42**, 2732 (1965).

17. D. W. Davidson, Y. P. Handa, C. I. Ratcliffe, J. S. Tse, and B. M. Powell, *Nature* **311**, 142 (1984).
18. E. Dendy Sloan Jr., *Nature* **426**, 353 (2003).
19. Lin-gun Liu and Wiliam A. Bassett *Elements, Oxides, and Silicates: High-Pressure Phases with Implications for the Earth's Interior*, Oxford University Press, New York, 1986.
20. A. P. Jephcoat, *Nature* **393**, 355 (1998).
21. Y. A. Dyadin, E. G. Larionov, A. Yu. Manakov, F. V. Zhurko, *Mend. Comm.* **393**, 209 (1999).
22. F. Izumi and T. Ikeda, *Mater. Sci. Forum*, **321-324,** 198 (2000).
23. J. Baumert, C. Gutt, V. P. Shpakov, J. S. Tse, M. Krisch, M. Muller, H. Requardt, D. D. Klug, S. Janssen, and W. Press, *Phys. Rev. B* **68**, 174301 (2003).
24. C. Gutt, J. Baumert, W. Press, J. S. Tse, and S. Janssen, *J. Chem. Phys.* **116**, 3795 (2002).
25. J. S. Tse, D. D. Klug, J. Y. Zhao, W. Sturhahn, E. E. Alp, J. Baumert, C. Gutt, M. R. Johnson, and W. Press, *Nat. Mater.* **4**, 917 (2005).
26. J. Baumert, C. Gutt, M. R. Johnson, J. S. Tse, D. D. Klug, and W. Press, *J. Chem. Phys.* **120**, 10163 (2004).
27. J. S. Tse, B. M. Powell, V. J. Sears, and Y. P. Handa, *Chem. Phys. Lett.* **215**, 383 (1993).

CHAPTER V

Pressure Induced Structural Transformations in Ba_8Si_{46} Clathrate – Results and Discussion

The purpose of this chapter is to present the results on the structure and dynamics of dense Ba_8Si_{46} clathrate. Pressure-induced changes in the Ba_8Si_{46} clathrate have been studied via high resolution angular dispersive X-ray diffraction. The experimental data were analyzed using the Rietveld Method to find accurate structural parameters and the Maximum Entropy Method (MEM) to extract the most probable charge density distributions. Our experimental findings, regarding the changes induced by the application of high pressures, will be discussed and compared with previous studies.

5.1 Structure I Silicon Clathrate under Room Conditions

Silicon clathrates are cage-type materials formed by silicon fullerene-like polyhedra, which share their faces to form a three-dimensional Si-sp^3 covalent network. Silicon clathrates are known to form two different types of crystalline structures: cubic type-I (sI) and cubic type-II (sII) [1]. At full cage occupancy, the chemical formulae of these structures are M_8Si_{46} and $M_{24}Si_{136}$ for sI and sII phases, respectively, M denoting the guest atom. Both phases are structurally similar to sI and sII phases of another class of guest-host materials, gas clathrate hydrates, presented in Chapter IV.

The type-I structure, characteristic for the barium doped silicon clathrate, has a cubic symmetry with space group *Pm3n*, formed by two types of polyhedra, as shown in Figure 5.1. The twelve-sided cavity (usually referred to as the small cage) consists of twelve pentagonal faces (5^{12}) and is located at the center and in the corners of the cubic unit cell. On the faces of the unit cell are situated six large cages (fourteen sided cavities

with twelve pentagonal and two hexagonal faces – $5^{12}6^2$). The two types of cages are connected through a pentagonal face.

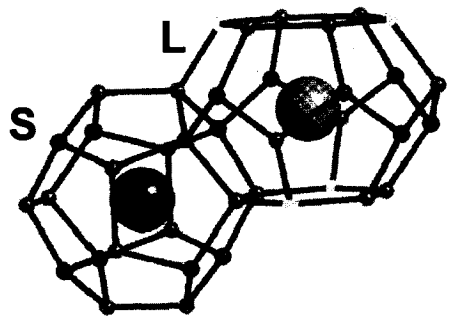

Figure 5.1. Small and large cages that form structure I Si clathrates. The small spheres represent the silicon atoms, and the large ones the encaged barium atoms. The two types of cages share pentagonal faces. Adapted from Perottoni *et. al.* [2]

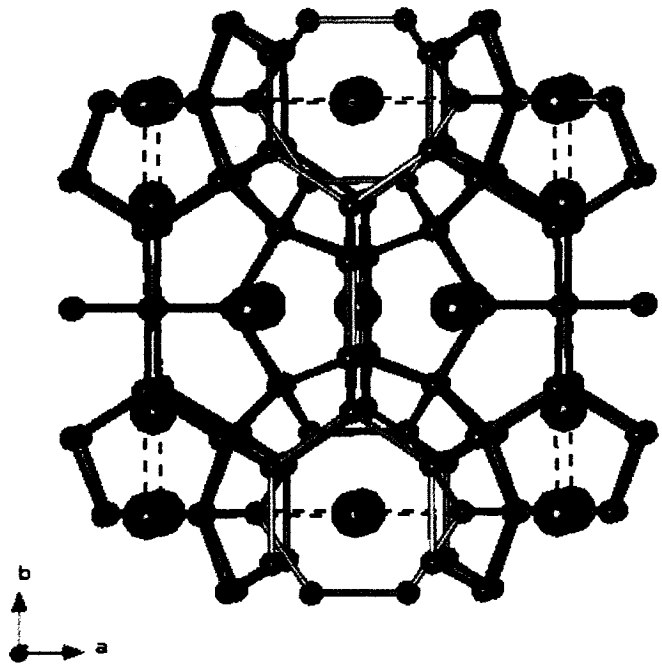

Figure 5.2. The cubic unit cell of Ba_8Si_{46} clathrate with guest (Ba) full occupancy. The gray sticks represent the Si bonds forming the cage framework. The small and large spheres show the position of Si and Ba atoms, respectively. The dotted line marks the limits of the unit cell.

The clathrate framework is formed by silicon atoms located at three distinct Wyckoff symmetry sites in space group *Pm3n*: *6c*, *16i*, and *24k*. At full occupancy, each cage contains one barium atom: Wyckoff positions *2a* for Ba in small cages (Ba-*S*) and *6d* for Ba in large cages (Ba-*L*). One unit cell, delimited by the dotted black lines, is represented in Figure 5.2. The Si atoms forming the framework of the cages are illustrated as small spheres and the guest Ba atoms as large spheres.

5.2 Previous Work and Motivation for Conducting the Present Study

Since the first synthesis of Na doped Si clathrate [1], various types of clathrates have been prepared with different guest atoms (e.g. K, Sr, and Ba) [2] or different host atoms (other group IV or III/V elements). This class of compounds has attracted increasing attention in the last few years because of their potential applications for thermoelectrics [3, 4] and wide band gap semiconductor devices [5, 6]. Moreover, superconductivity discovered in Ba doped Si clathrate [7, 8] has driven extensive studies of this compound and other related semiconductor clathrates.

In addition to presenting a superconducting state, Ba_8Si_{46} shows a peculiar physical property: when compressed, as shown from x-ray diffraction (XRD) measurements, a reversible iso-structural phase transition occurs and is characterized by a sudden reduction in the unit cell volume at about 14-17 GPa [9, 10]. In contrast to the change of the lattice parameter at the transition, no abrupt change in the atom positions has been found. Near-edge x-ray absorption [9] and Raman spectroscopy studies [11], however, have revealed an additional "transition" for Ba_8Si_{46} at about 5 GPa. The physical origin of the two "transitions", at 5 and 14-17 GPa, is still not clearly understood.

Ba L_{III} XANES spectra [9] show significant changes in the absorption edge position at 5 GPa, which might indicate rehybridization of the Ba atoms. It has been suggested [9] that the features in the Ba L_{III}-absorption edge probably probe only changes related to the large cages since there are three times more of them than small cages in a

unit cell. Also, the Raman spectroscopy study reveals that the two vibrational bands related to Ba in the large cages suddenly become a broader and weakened band. Since theoretical calculations show a small transfer of electrons from Ba to the Si framework (0.02 *e* for Ba-*S* and 0.03 *e* for Ba-*L*), it has been proposed that this transition is driven by a substantial change in the polarizability of Ba-*L* atoms [10].

Besides the large volume collapse observed by XRD at about 17 GPa, Raman spectroscopy shows that a strong vibrational peak (89 cm^{-1} at atmospheric pressure), believed to be related to Si framework vibrations, suddenly disappears around 15 GPa. Also, Yang *et al.* [10] reported that the thermal parameters of all silicon atoms increase significantly from around 2 $Å^2$ to 5 $Å^2$ at about 17 GPa. These values are unphysically high for the dense Ba_8Si_{46} structure and have been translated as dynamically disordered Si atoms. Thus it has been suggested [10] that this disorder leads to an abrupt collapse of the unit cell volume, without a change in crystalline structure.

To further explore the subtle changes in structural parameters and electronic density distribution induced by the application of high pressure, high quality high pressure angle dispersive X-ray powder diffraction measurements on Ba_8Si_{46} clathrate were carried out [10]. The goal of this investigation was to reproduce the previous reported results summarized above and to propose possible mechanisms for the two transitions observed as a function of pressure. As we believe that structural changes observed in the previous studies should reflect in changes in the charge density distribution inside the unit cell, the application of the model-independent Maximum Entropy Method to extract the electron density directly from the XRD diffraction data was pursued in the present work.

5.3 Experimental Details

The experiments presented in this study were performed by a collaborating group, at SPring8 (Japan) and are presented in detail in a previous study [10].

Alloy ingots with a composition of Ba_8Si_{46} were prepared by arc melting pure elements of 99.9999% Si and 99.8% Ba in a purified argon atmosphere. Structure I Ba_8Si_{46} clathrate sample was synthesized by a high temperature and high pressure route at 3 GPa and 1173 K, using a multi-anvil pressure apparatus with 8 mm cube pressure cells. High quality *in situ* high pressure angular dispersive XRD measurements at ambient temperature using a diamond anvil cell (DAC) with liquid helium as pressure transmitting medium were performed at the BL10XU beamline, SPring8 (Japan) at a wavelength of 0.4969 Å. Pressure was measured using the ruby fluorescence technique previously presented in Chapter III. A total of 25 diffraction patterns from atmospheric pressure up to approximately 32 GPa were recorded, at room temperature, using an image plate detector.

5.4 Structure Refinement using the Rietveld Method

X-ray diffraction patterns observed at different pressures as well as the results of the associated Rietveld refinements will be presented in this section.

X-ray diffraction patterns measured with increasing pressure up to 31 GPa are shown in Figure 5.3. Except for peak shifts with pressure, no additional features or significant change in relative intensities, which might indicate a change in the crystal symmetry, have been observed. All patterns could be indexed with the cubic *Pm3n* space group.

Rietveld analysis was performed in order to see the pressure-induced evolution of structural parameters (lattice parameter and atomic positions). The observed and calculated XRD patterns, as well as the difference traces that illustrate the good agreement between the measured data and refinements, at 0, 8, and 16 GPa, are shown in Figure 5.4. The quality of X-ray diffraction data was very good, even at high pressure where Bragg reflections at high angles were clearly resolved (Figure 5.4, insert). For the Rietveld refinement, performed using program RIETAN 2000 [12], the fitted parameters were: peak profile parameters (using pseudo-Voigt function), lattice constant, atomic

thermal parameters, atom positions, background parameters (using 12-coeficient polynomial function), the shift in the angle values, and the scale parameter. No correction for the preferred orientation was needed.

The pressure dependence of the full width at half maximum (FWHM) values, obtained from the refinements for three non-overlapping reflections, is presented in Figure 5.5.

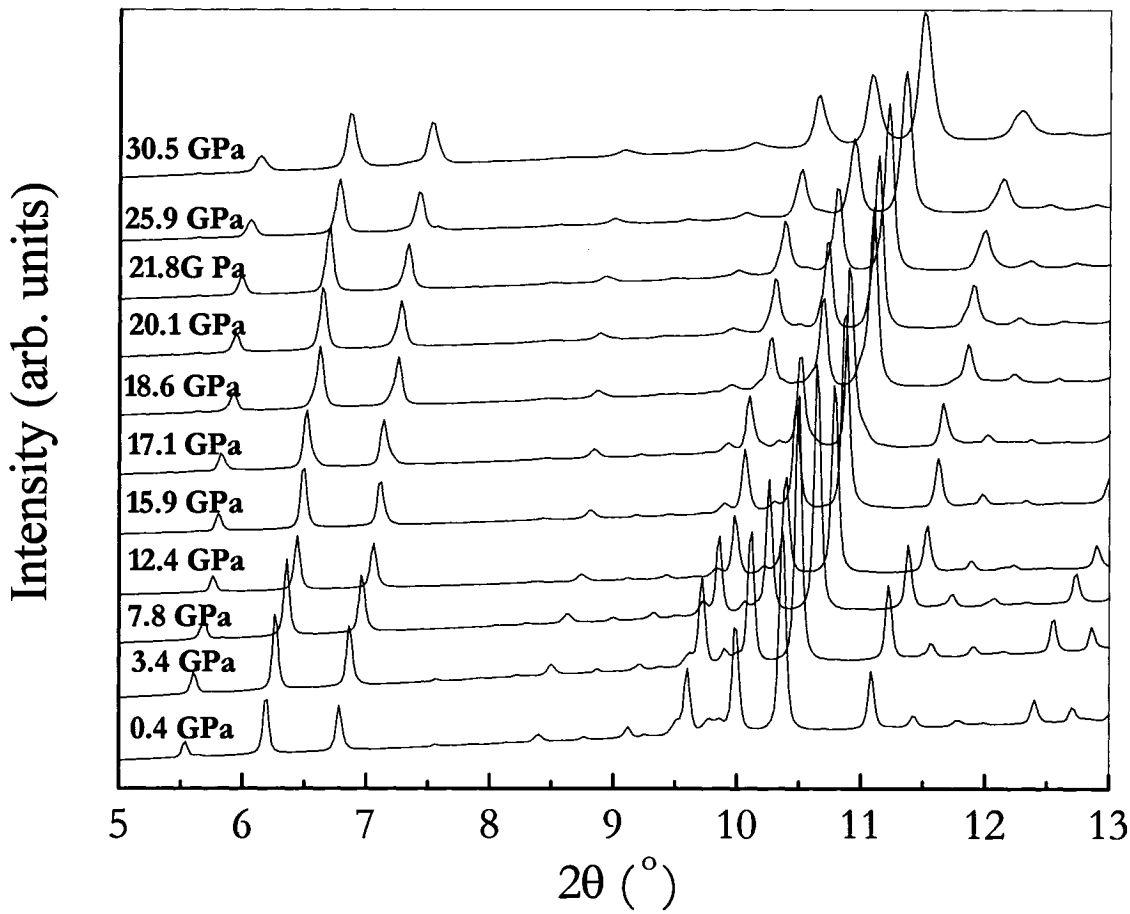

Figure 5.3. Pressure evolution of the angular dispersive XRD patterns. The shift of the diffraction peaks towards higher angles can be observed as the pressure is increasing.

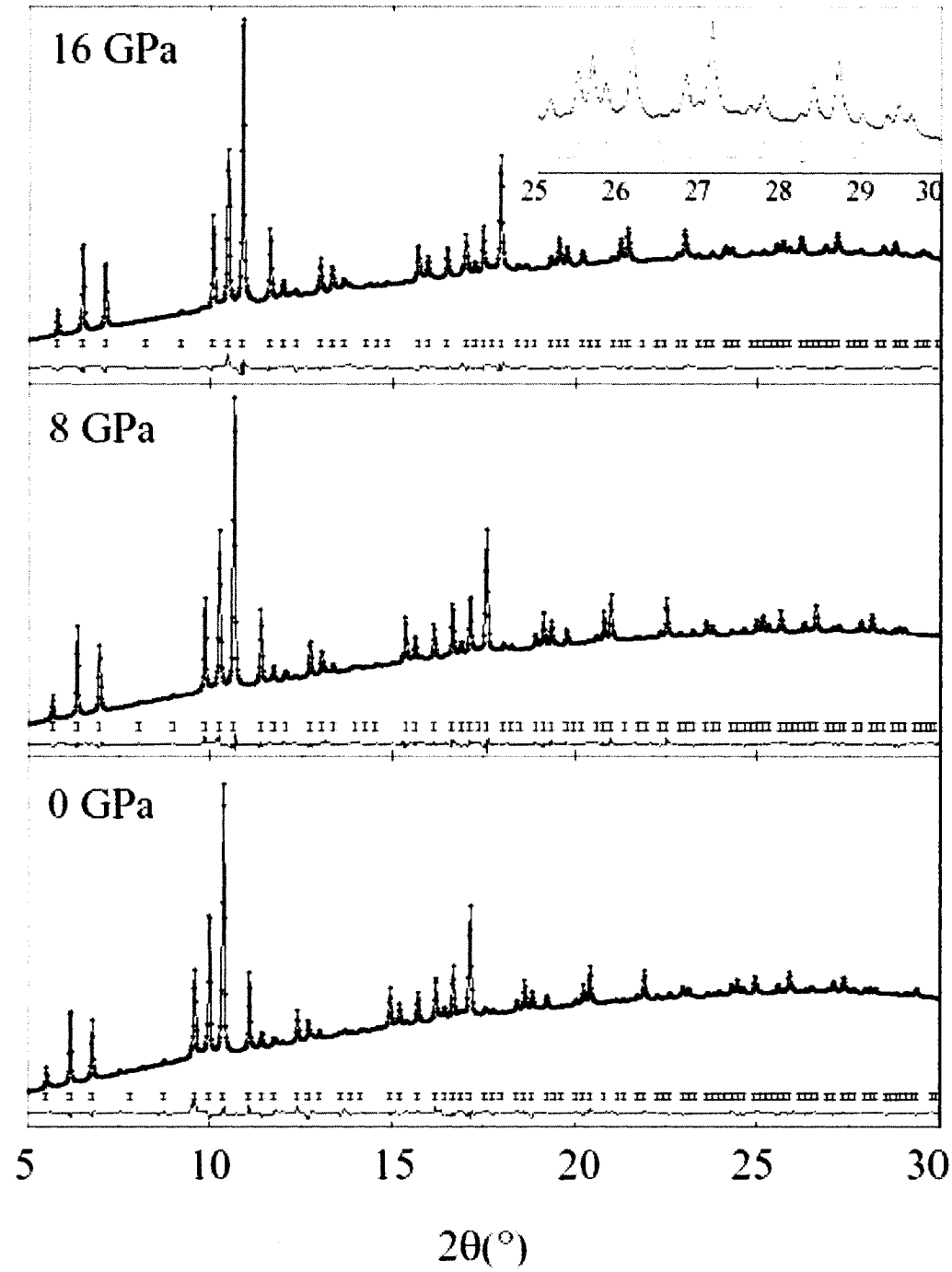

Figure 5.4. X-ray powder diffraction of Ba_8Si_{46} at selected pressures. The dot symbols denote the experimental data; the solid line, the calculated pattern; tick marks the calculated peak positions; the bottom curve represents the difference between observed and calculated patterns.

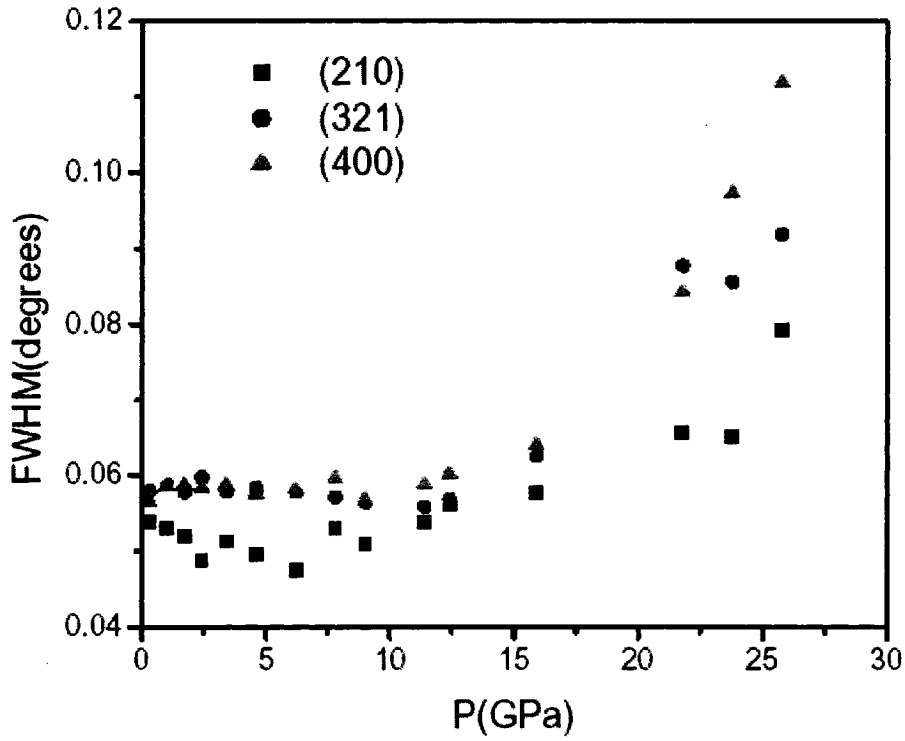

Figure 5.5. FWHM for three non-overlapping peaks as a function of pressure.

It is important to notice that, as a result of using He as an hydrostatic pressure transmitting medium, no deterioration of lineshape or linewidth was observed up to 16 GPa. Above 16 GPa a substantial broadening of the width of all diffraction peaks is observed, as well as the increasing of FWHM with the increasing pressure. The abrupt change in the X-ray diffraction peak profile is obviously intrinsic to the phase transition since the He pressure transmitting medium is expected to remain hydrostatic up to at least 30 GPa.

Figure 5.6 shows the pressure dependence of unit cell lattice parameter obtained from Rietveld refinements.

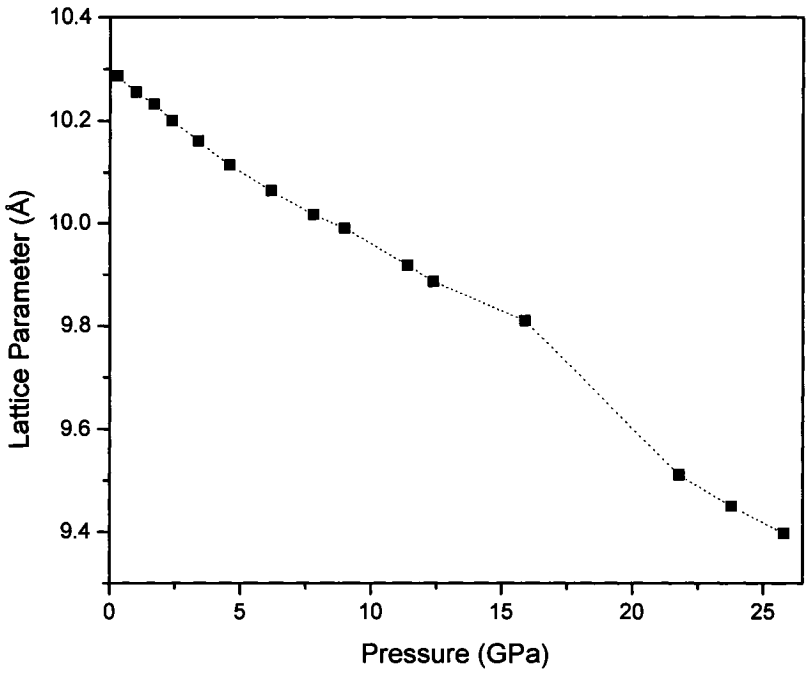

Figure 5.6. Lattice parameter as a function of pressure. The dotted line is drawn to guide the eye. The errors of the lattice parameter values are about ±0.001 Å.

Up to about 16 GPa, the lattice constant was found to decrease with pressure in the expected fashion, dictated by Birch-Murnaghan isothermal equation of state [13]. At 16 GPa, an abrupt drop in the lattice parameter (and, consequently, unit cell volume) is clearly observed. This result verifies that the reduction in cell volume reported in previous experiments on K_8Si_{46} clathrate [14] and Ba_8Si_{46} clathrate [9, 10] is, indeed, an intrinsic phase transition rather than a non-hydrostatic effect. On the other hand, no abnormality in the lattice parameter has been observed at pressure around 5 GPa, as one would probably expect following the near-edge x-ray absorption [9] and Raman spectroscopy studies [11].

For the purpose of understanding the nature of the two previously reported transitions, the evolution with pressure of the three internal atomic coordinates which describe the silicon atomic position is highly relevant.

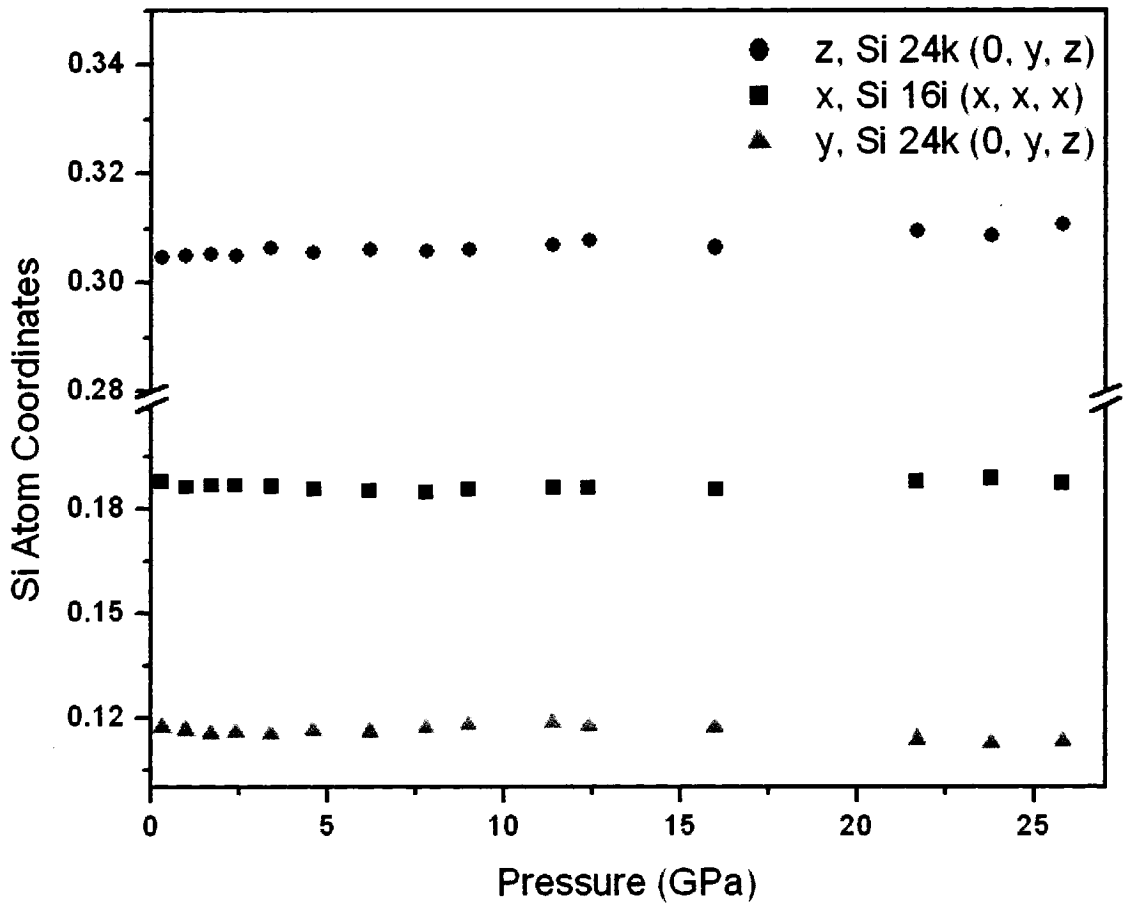

Figure 5.7. Pressure dependence of Si atom positions. The errors associated with the relative atom coordinates values are about ±0.001.

Within the uncertainty, all Si atoms remain in the same position, indicating that there is no pressure induced change in the geometry of the Si cages (Figure 5.7). Our results are in good agreement with those previously reported by San Miguel *et al.* [9]. These findings lead to the conclusion that the transition observed at 16 GPa is an homothetic volume collapse of the silicon cages.

Given the unanswered questions regarding the origin of the structural changes induced by high pressure in Ba_8Si_{46} clathrate, an analysis of the changes in the charge density distributions derived for all pressure points available in the experiment was pursued as an attempt to clarify the ambiguous points. Results of the MEM analysis, used

to calculate the most probable electron density distributions from the X-ray diffraction data, are presented in the next section.

5.5 Charge Density Distributions Derived from the MEM Analysis

To further explore the characteristics of the two transitions observed at high pressure in Ba_8Si_{46}, we have derived electron density distributions of high density Ba_8Si_{46} directly from the XRD data, using a model-independent method: the Rietveld/Maximum Entropy Method (MEM) analysis. We will show that the structural changes reported in the three previous studies [9-11] are reflected in the electron density distribution variations with pressure.

5.5.1 Details of the MEM/MPF Analysis

The Rietveld/MEM and MEM/MEM-based Pattern Fitting (MPF) methods have been presented in Chapter II. The MEM calculations were carried out using PRIMA [15]. The electron density maps were generated using the program LIMNER [16].

In this study, the total number of reflections considered varied from 129 (at 0.3 GPa) to 95 (at 25.8 GPa). Out of the total number, 43 reflections (for 0.3 GPa) and 40 (for 25.8 GPa) were non-overlapping. The reliability factors R_{wp} and R_I for the Rietveld refinements were, typically, 1.3% and 6%, respectively. MEM analyses were initiated from a uniform charge density distribution and performed for a cubic lattice of 64×64×64 pixels. MEM analyses were followed by iterations of MPF to minimize the bias to the structural model in the extraction of the observed structure factors F_o. The iterative procedure was repeated until the R_I factor was minimized, becoming 3 % on average, as opposed to 6%, as obtained typically from a Rietveld refinement only. Figure 5.8

illustrates the improvement of the fit between the observed and calculated patterns after 4 MEM/MPF iterations as opposed to conventional Rietveld refinement.

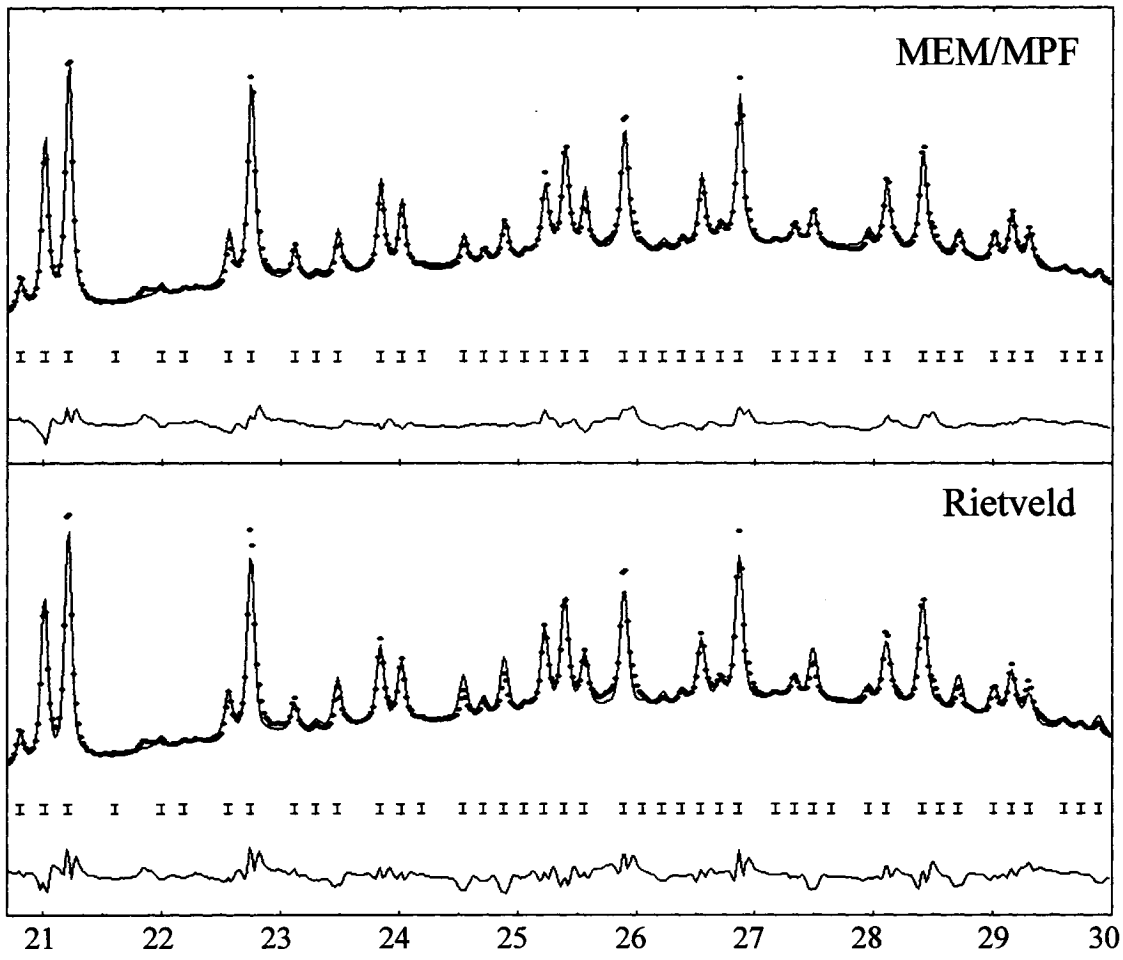

Figure 5.8. Observed and calculated patterns at 11.4 GPa, in the high angle region. The goodness-of-fit parameters were R_{wp}=1.32%, R_I =5.80% for the Rietveld analysis and R_{wp}=1.05%, R_I =2.86% after 4 MEM/MPF cycles.

The weighed reliability factor (R_{wF}) derived from the MEM analysis was in the 2.5-3.9 % range for the data in the entire pressure measurement domain.

For a good visualization of all the significant changes in the electron density distribution in a unit cell, three different crystallographic planes were chosen to be plotted, namely, the (100), (200), and (110) planes. The (100) plane cuts through the

middle of Ba-*L* (site *6d*) and Ba-*S* (site *2a*, corners of the picture) atoms; two different sites of the framework silicon atoms can also be observed (see Figure 5.9a). To better visualize the changes in Ba-*S* electron distribution, the (200) plane cutting through the middle of the unit cell (i. e. Ba-*S* atom) is also shown (Figure 5.9b). And finally, the (110) plane was further chosen as it shows the charge density distribution of the bonding between two connecting symmetry related Si atoms at 16*i* symmetry sites (Figure 5.9c).

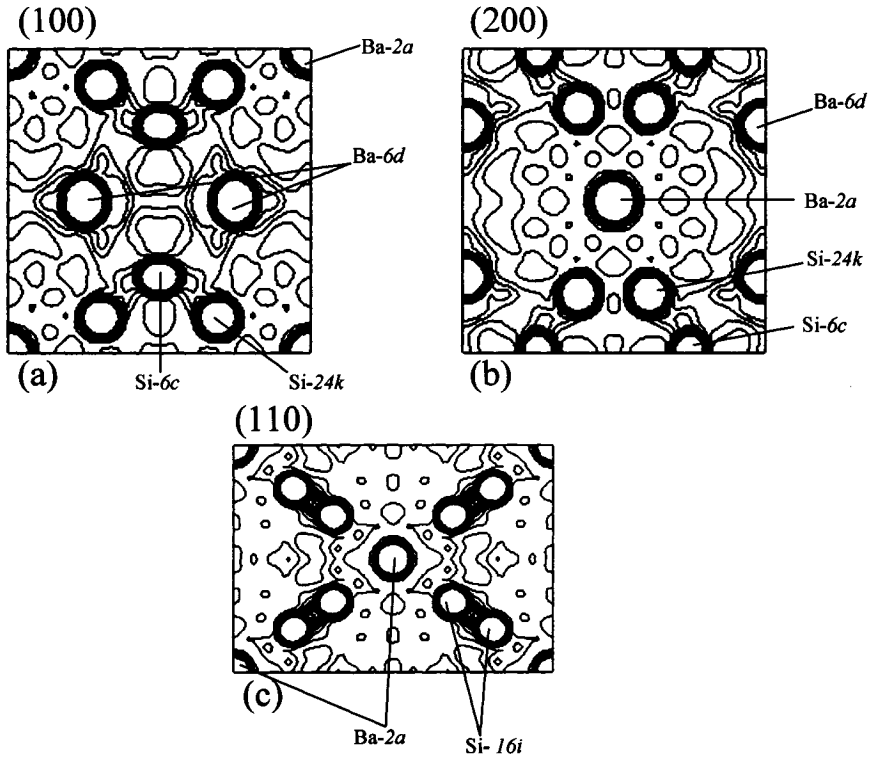

Figure 5.9. The (100), (200), and (110) crystallographic planes of the Ba_8Si_{46} unit cell. The minimum and maximum contour levels are 0.06 and 2.00 $e/Å^3$, respectively with a contour spacing of 0.10 $e/Å^3$.

5.5.2 Difference Charge Density Distribution Maps

Before starting a detailed analysis of the pressure induced changes of the electron density maps of Ba_8Si_{46} clathrate, we wanted to test the internal consistency of the electron density distributions computed using MEM. For this purpose we studied the

charge density difference [$\Delta\rho = \rho(P) - \rho(P_0)$] between the calculated charge density at a given pressure, $\rho(P)$, relative to that at the lowest pressure (0.3 GPa, in our study), $\rho(P_0)$, as obtained from MEM analysis.

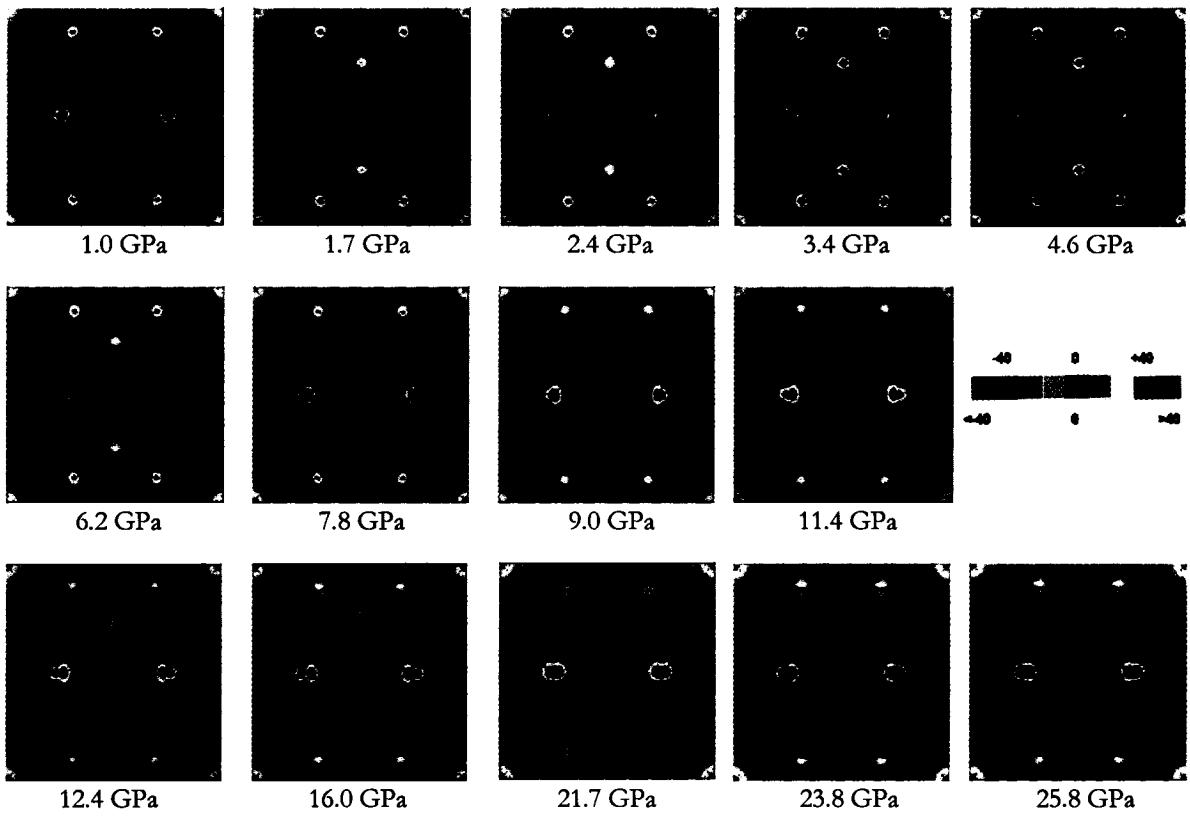

Figure 5.10. Plots of MEM charge density difference relative to 0.3 GPa at selected pressures, plane (100). Contour lines are drawn from –40.0 to 40.0 *e*/ Å^3 at intervals of 0.1 *e*/ Å^3.

The $\Delta\rho$ maps were computed by subtraction of the charge density at each grid point used in the MEM analysis. Therefore, the effect of volume reduction at higher pressures was not taken into account. This study can also provide qualitative information on the change of electron density topology when Ba_8Si_{46} is compressed, even without proper volume normalization.

The charge difference density maps at several pressures for the (100) plane are shown in Figure 5.10. Systematic changes in the charge density differences are observed, relative to the charge density distribution at 0.3 GPa. The appearance of systematic changes demonstrates the internal consistency of the charge density derived from the MEM analysis. The most noticeable feature is the gradual increase in the charge accumulation on the Si atoms (*6c* and *24k* sites) for pressures up to about 7 GPa. As pressure is increasing over 7 GPa, the charge accumulation relative to the 0.3 GPa distribution at the Si sites starts to diminish. At 26 GPa, the electron distribution at the Si atoms is depleted quite significantly. The electron density of the Ba atoms in the large cages seems to accumulate and distort significantly with increase pressure. The distortion of the electron cloud around the Ba-*L* atom shows the electrons are polarized away from the ideal crystallographic Ba atomic sites.

To visualize the change in Ba-*S* charge density, the (200) plane is plotted in Figure 5.11. Similar to that of the (100) plane, a systematic change in the charge density difference contours is observed. In contrast to Ba-*L* atom, at most of the pressures, electrons are polarized away from the Ba in small cages central sites, as indicated by a slight depletion of charge density (blue contour), into the immediate surroundings (yellow contours). We can conclude that Ba atoms in the small cages are more susceptible to sharing valence electrons with cage forming Si atoms when cubic structure-I Ba_8Si_{46} is compressed. From 9 GPa to 26 GPa, again relative to the 0.3 GPa, a gradual charge transfer is observed from both the Si and the Ba atoms into the interstitial space.

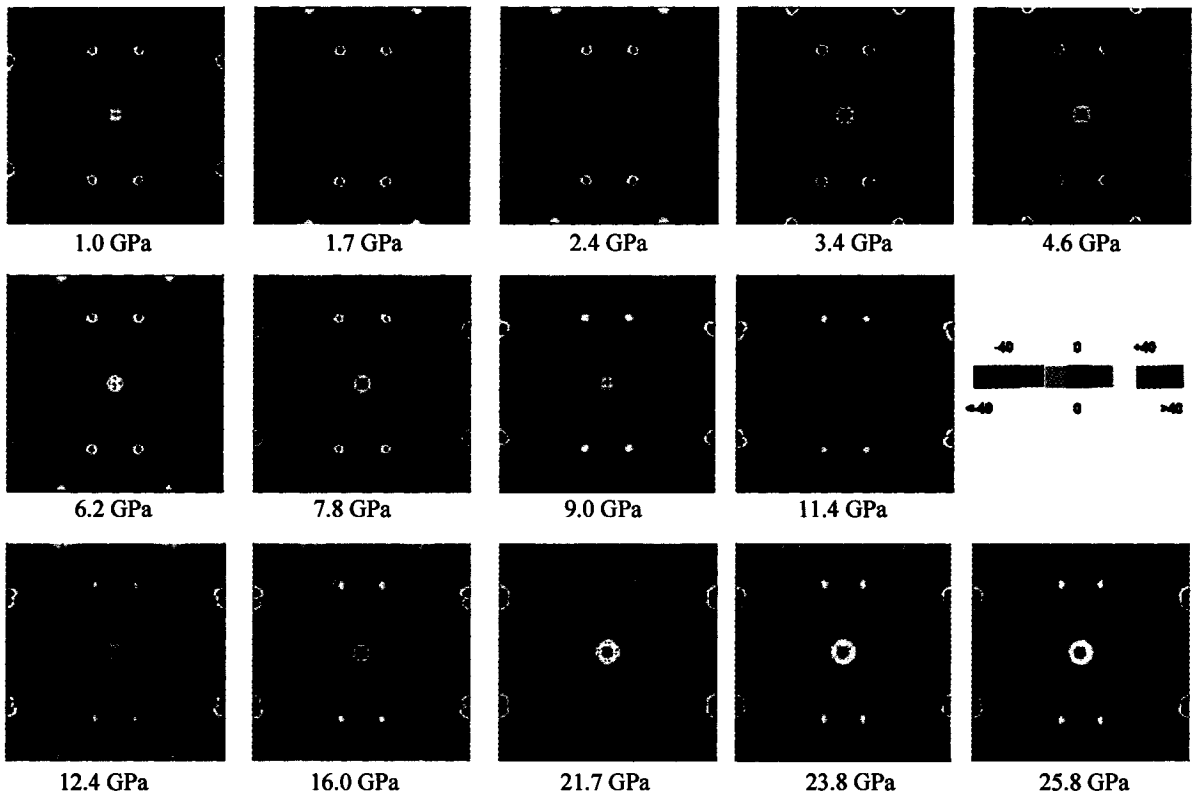

Figure 5.11. Plots of MEM charge density difference relative to 0.3 GPa at selected pressures, plane (200). Contour lines are drawn from –40 to 40 *e*/ Å^3 at intervals of 0.1 *e*/ Å^3.

As only Si-*6c* and Si-*24k* atoms can be seen the (100) and (200) planes, the charge density maps of the (110) plane are plotted (Figure 5.12) to study the changes in electron distribution for Si at the *16i* sites. The plots in Figure 5.12 confirm the same behavior for all the framework silicon atoms, regardless of the crystallographic site. There is an initial accumulation of electrons on the framework Si atoms until 7 GPa. Between 7 and 16 GPa, the charge redistribution on the Si atoms seems to decrease and then the electron charge starts to shift away from the Si atoms for pressures higher than 16 GPa.

The analysis of changes with pressure of the electron density maps, relative to 0.3 GPa distribution, reveals that there are clear signs of pressure induced electronic changes

at about 7 GPa and at 16 GPa. We believe that these changes are related to the phase transitions observed previously in Ba_8Si_{46} clathrate.

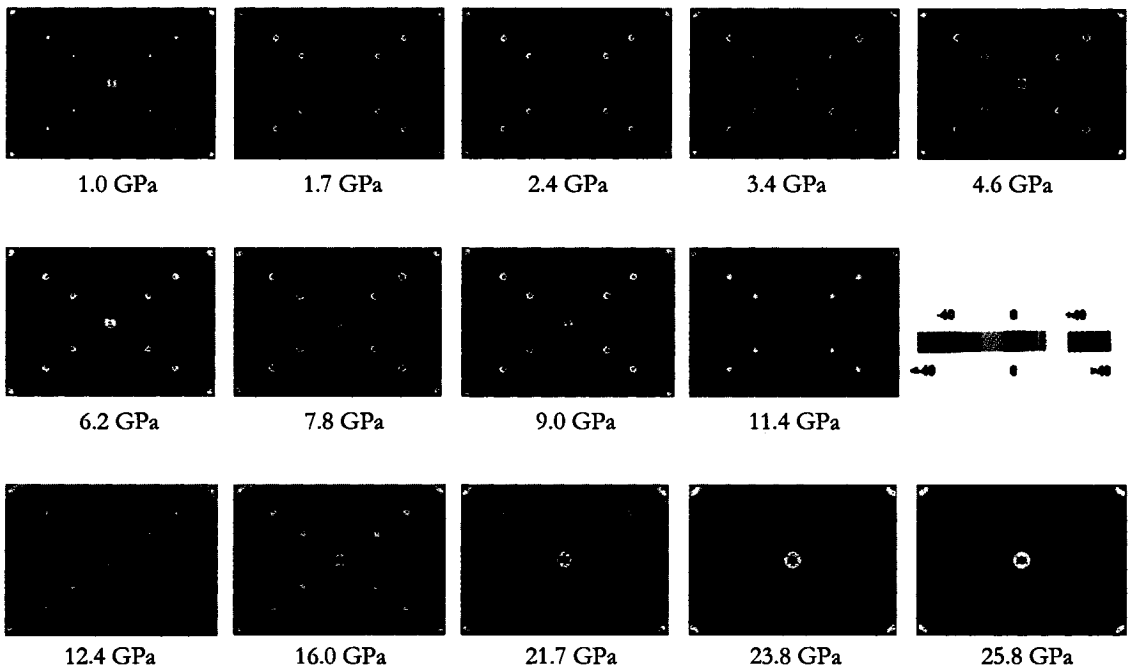

Figure 5.12. Plots of MEM charge density difference relative to 0.3 GPa at selected pressures, plane (110), revealing the changes in the Si-*16i* atoms. Contour lines are drawn from –40 to 40 *e*/ Å^3 at intervals of 0.1 *e*/ Å^3.

To confirm and detail the conclusions drawn from the examination of the difference electron density distribution maps, the absolute charge density distributions calculated for each pressure are presented and analyzed in the next section.

5.5.3 Absolute Charge Density Distributions

We now move to analyzing the electron density maps computed by MEM and cutting through the two unique Ba atoms [(100) and (200) planes] and pairs of Si bonds [in the (110) plane]. A quick examination of the charge density distributions at various pressures immediately reveals two "breaking points" in the behavior of the system as the pressure is increasing. The pressures corresponding to these discontinuities are actually the same with those at which phase transitions were reported in the previous studies: 7 and 16 GPa. The results are in substantial agreement with the preliminary assessments from the charge density difference plots. The following discussion of results is going to be structured around the two observed transitions.

5.5.3.1 Proposed Mechanism for the 7 GPa Transition

The contour lines around the two Ba-*L* atoms lying on the (100) plane (Figure 5.13) clearly show that at low pressure (1 GPa) the electron densities are mostly concentrated in close proximity to atom centers. As the pressure increases, *e.g.,* to 7.8 GPa, the electron density becomes more diffuse and spreads over into the interstitial space. There is also a strong indication that the "effective" size of the Ba is reduced somewhat. Moreover, the contour lines around the Si atoms become denser indicating a small increase in charge accumulation.

A similar charge change distribution pattern also emerges for the Ba-*S* atom lying in the (200) plane (Figure 5.14) when Ba_8Si_{46} is compressed from 1 to 7.8 GPa. A substantial charge transfer from the Ba atoms to the Si framework under ambient pressure is already present, as indicated by the charge density difference map. This observation indicates that Ba-Si interactions are enhanced upon compression and consequently promotes the migration of Ba valence electrons into empty states of predominant Si-like character.

This behavior is consistent with the calculated electronic band structure of Ba_8Si_{46}, which reveals that strong hybridization of the Ba state with the Si_{46} conduction band plays a key role in the superconducting behavior [17-19]. The increase of charge density in the interstitial region and at the Si atoms sites is in accord with the increase of the atomic thermal parameters determined from the previous Rietveld refinement study [10].

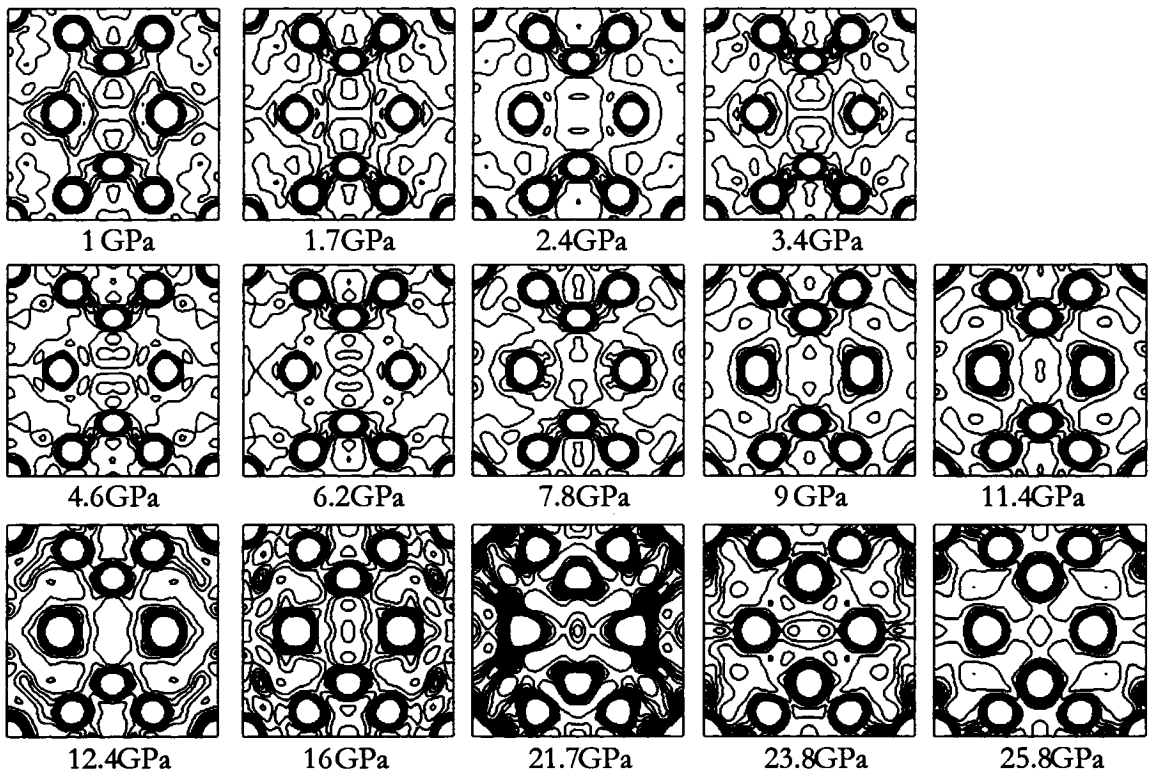

Figure 5.13. Contour plots of the charge density in the (100) plane, at selected pressures, highlighting the Ba atom in the large cage. Contour lines are drawn from 0.06 to 2.00 *e*/ Å^3 at intervals of 0.10 *e*/ Å^3.

The pressure evolution of the charge density of the Si-Si bonds, both occupying the *16i* sites, can be visualized in Figure 5.15. At 1 GPa, the electron density is found to concentrate between the Si atoms indicating strong genuine σ-covalent bonds. With the increase in pressure, the electron density distribution between the two bonded Si atoms becomes more diffuse and delocalized into the open space.

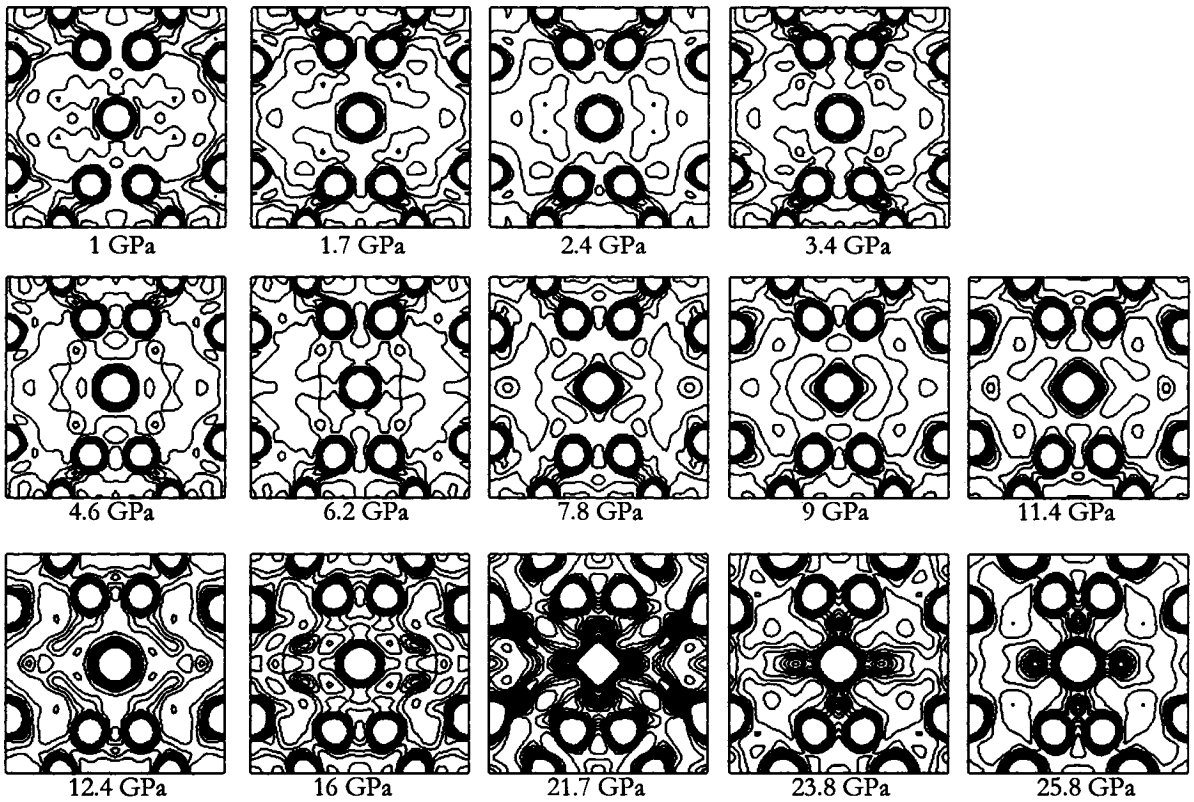

Figure 5.14. Contour plots of the electron density in the (200) plane at selected pressures, highlighting the Ba atom in the small cage. Contour lines are drawn from 0.06 to 2.00 *e*/ Å^3 at intervals of 0.10 *e*/ Å^3.

Based on all these observations, we can conclude that, as pressure is increased to 7 GPa, the initial response of the system is to bring the Ba atoms closer to the Si. As a result there is some enhancement of charge transfer from the Ba to the Si framework. This results in a small charge depletion in Ba located in small cages and slight charge

accumulation on the Si. This conclusion is in accord with the previous experimental observations. It was shown, from an EXAFS study [9], that the energy of the Ba L_{III} absorption edge first increase with pressure and then decrease suddenly showing a discontinuity at 5 GPa. The increase in the energy of the inflection point of the absorption peak, "white line", can be rationalized as the result of charge transfer of Ba atoms to the Si framework. Examination of the electron density maps in the (100) plane indeed revealed that Ba atoms in large cages start to change the almost spherical electron distribution at 6.2 GPa, becoming more anisotropic and "spread-out" at higher pressures. A more positively charged Ba atom is expected to increase the excitation energies into the empty states. As suggested previously [10], a tighter Ba ion will be less polarizable thus reducing the intensity of the Raman bands.

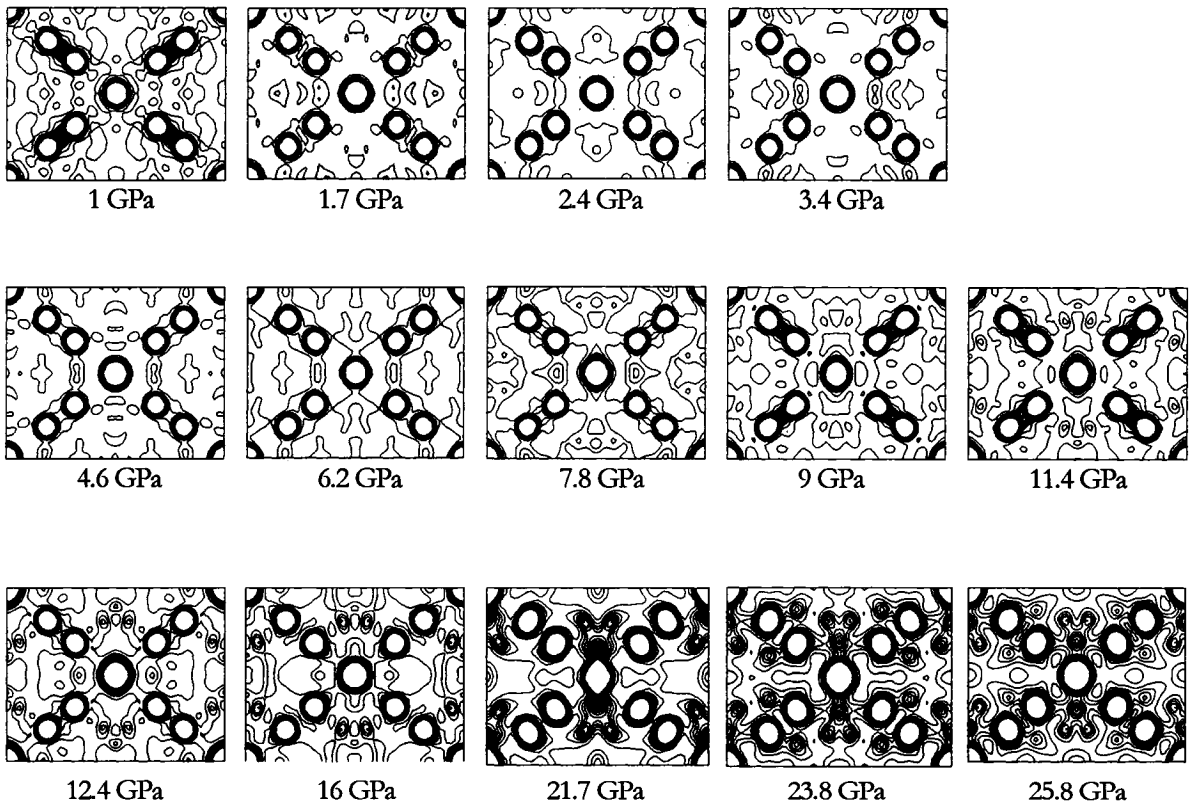

Figure 5.15. Contour plots of the electron density in the (110) plane at selected pressures, highlighting the Ba atom in the small cage. Contour lines are drawn from 0.06 to 2.00 *e*/ Å^3 at intervals of 0.10 *e*/ Å^3.

5.5.3.2 Proposed Mechanism for the 17 GPa Transition

When Ba_8Si_{46} is compressed beyond 16 GPa, a dramatic change in the electron topology around the Ba atoms takes place. The electron density around the Ba atoms, both in the small and large cages, distorts from the atomic-like spherical distribution. In the (200) plane, electrons around the Ba-*S* atom extend towards the Si atoms and to the nearest neighbor Ba-*L* atoms in adjacent cages. There are signs of significant overlap of the valence electrons from the Si and both types of Ba atoms. This is a consequence of the valence electrons from these atoms are being "squeezed" into the interstitial space. A very similar electron density topology is also observed for the Ba atom in the large cage although this shows to a lesser extent.

A significant change was also observed in the Si-Si bonding charge density at pressure above 16 GPa. The electron density is no longer concentrated between the Si atoms but is "squeezed" into the interstitial space. The electron topology clearly shows that the σ-character of the Si-Si bond is replaced by a strong participation of π-bonding like interactions. Under very high pressure, the Si atoms utilize the more diffuse *d*-states to redistribute the bonding electrons into the more open but less repulsive space. At the same time, the Si-Si bonds weaken, resulting in a volume contraction during this electron topological homothetic phase transition.

In a previous study [10], two explanations were proposed to rationalize the volume reduction associated with the iso-structural transition at 17 GPa. The observed phase transition in Ba_8Si_{46} is first correlated to a similar pressure induced transition observed in pure FCC Si to Si-V [20]. A sudden change in compressibility and volume contraction during the phase transition due to the creation of Si vacancies was invoked as another possible explanation [10]. The apparent good agreement between experimental and theoretical equations of state on a Ba_8Si_{43} model with Si vacancies in the Si 6*c* sites at pressures over 16 GPa lend support to the latter explanation [10]. There are however several weaknesses to that proposal. First of all, Rietveld refinements led to the conclusion that anomalies in the thermal parameters were observed in all Si positions and consequently were not restricted to Si at 6*c* sites. The proposed mechanism required the

formation of "excess" Si that was excluded from the sample. As far as we can tell, there was no significant evidence from the XRD data to support this suggestion. Furthermore, there is no sudden change in the background of the powder x-ray diffraction patterns that might be attributed to the formation of amorphous silicon nor are there any additional Bragg peaks that otherwise could be assigned to any high-pressure phase of Si. The refined atom positions also do not show any anomaly close to the transition pressure.

In the next section, the question of the reliability of MEM in reconstructing charge density distribution form the X-ray diffraction data, in the particular case of our study on Ba_8Si_{46} clathrate, is addressed.

5.6 The Accuracy of Charge Density Distributions as Constructed by MEM

The analysis of errors that affect the charge density distributions derived by MEM from XRD data is a complex problem, as different sources of uncertainties reflect into the accuracy of these distributions: experimental errors, errors related to the ability of Rietveld and MPF methods to extract the "observed" structure factors from the diffraction data, errors in MEM calculation method (primarily influenced by the completeness of the observed structure factors set). Even though the estimation of uncertainties is a very important aspect for a full understanding and correct interpretation of the MEM charge densities, only a few studies of this problem have been reported so far in the literature [21-23], and charge density maps obtained by MEM are usually presented without discussion of errors.

In this section, the accuracy by which the reported MEM calculated charge density distributions reproduce the observed X-ray diffraction is analyzed. The quantities taken into account for this study are:

$F_{MEM}(\mathbf{k})$ - structure factor of the **k** reflection, as calculated by MEM,

$F_{obs}(\mathbf{k})$ - structure factor of the **k** reflection extracted by MPF from the XRD data, used as the observed data in the MEM analysis,

$\sigma_{obs}(\mathbf{k})$ - standard deviation in the $F_{obs}(\mathbf{k})$,

$\sin(\theta)/\lambda$ - the range, in the reciprocal space, of structure factors considered in the MEM analysis; this will also be referred to as the "cut-off" on the observed structure factors.

An error analysis was performed for two different pressure points discussed in our study, a low and a high pressure, 0.3 and 21.8 GPa. Figure 5.16, (a) and (b), presents the histograms of the number of reflections versus $[F_{MEM}(\mathbf{k})- F_{obs}(\mathbf{k})]/\sigma_{obs}(\mathbf{k})$ for 0.3 and 21.8 GPa, respectively. The number of reflections included in the MEM calculations and MEM reliability factors, as reported by PRIMA, are listed for each pressure point. The fact that both histograms follow a Gaussian-like distribution centered on zero is an indicator of a good agreement between the structure factors calculated by MEM and the structure factors extracted from the X-ray diffraction data using the MPF analysis. Also, most of the structure factors reconstructed by the Rietveld/MEM analysis fall within about 1.5σ, as compared to the observed structure factors.

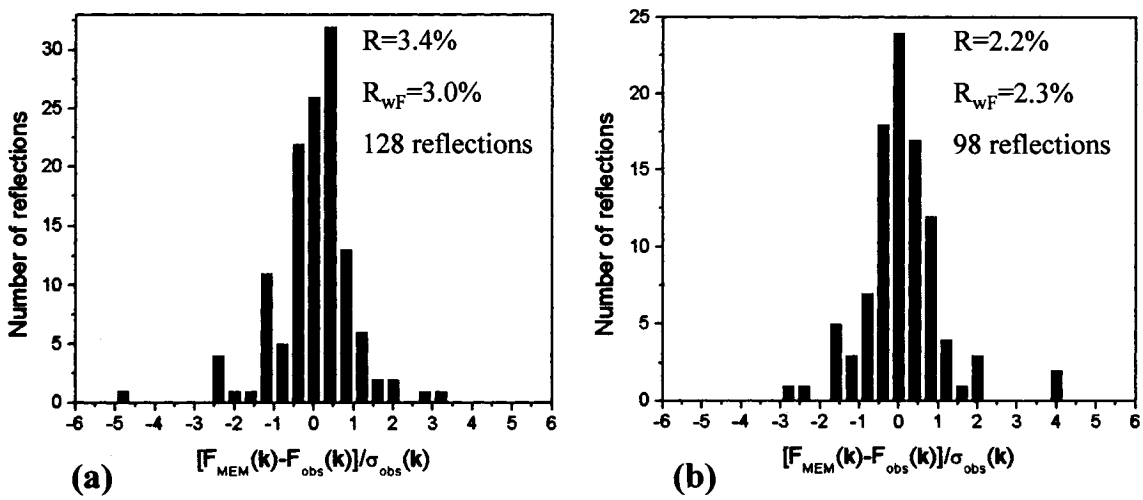

Figure 5.16. Histogram of number of reflections versus $[F_{MEM}(\mathbf{k})- F_{obs}(\mathbf{k})]/\sigma_{obs}(\mathbf{k})$ for X-ray diffraction data collected at (a) 0.3 GPa and (b) 21.8 GPa.

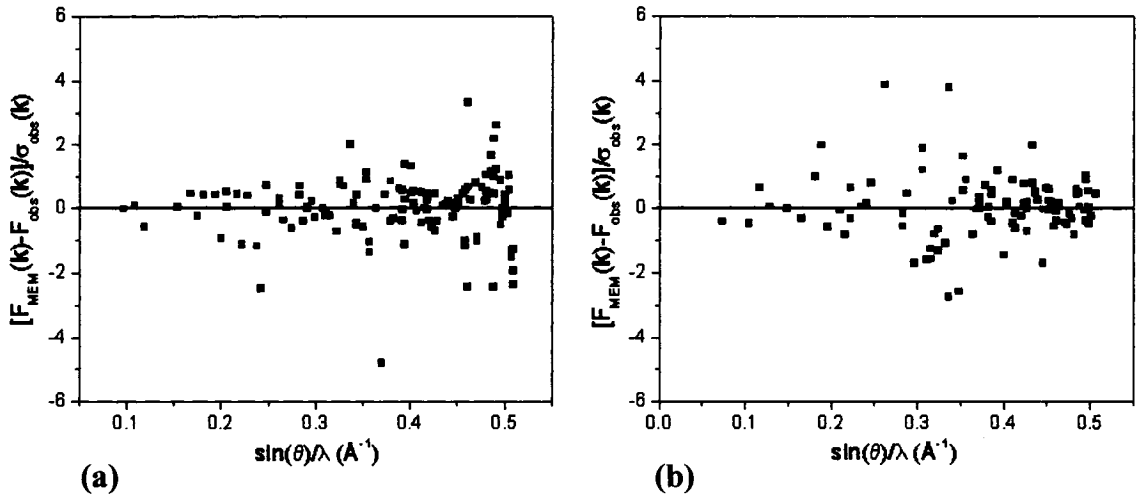

Figure 5.17. Distribution of the structure factor errors over the reciprocal space in which the X-ray diffraction data were collected at (a) 0.3 GPa and (b) 21.8 GPa.

Another informative form of representation of the data is the distribution of the error function over the reciprocal space in which the X-ray diffraction data were collected. A large cut-off on the observed structure factors is mostly reflected in the fine details of the charge density distribution maps, as the information on valence electron distributions is contained in the high angle diffraction peaks. As it can be observed in Figure 5.17, the errors are fairly uniformly distributed over the entire $\sin(\theta)/\lambda$ range. This is a positive finding, leading to the conclusion that the core and bond electron densities are both affected by small errors and the fine details in our electron density maps are not artifacts from MEM calculations.

Moreover, the error of the MEM calculated structure factors, relative to the observed ones, is plotted in the reciprocal space for both low- and high-pressure X-ray diffraction patterns (Figure 5.18). While the vast majority of points have an associated error less then 10%, there are a few reflections with structure factors carrying extremely big errors, even up to about 80%. In Tables 5.1 and 5.2 these reflections, corresponding to the labeled points in Figure 5.18, will be listed.

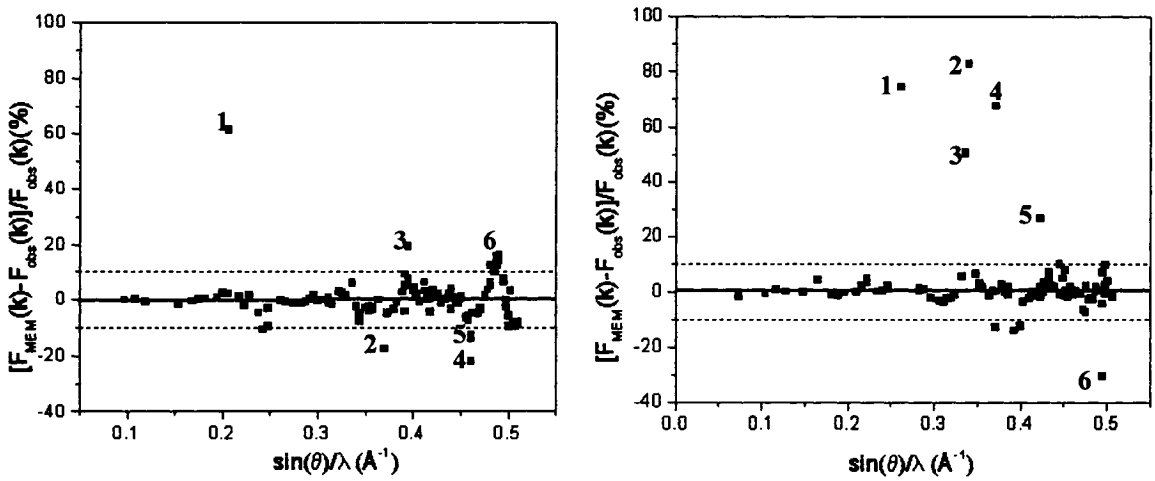

Figure 5.18. Distribution of error of the MEM calculated structure factors, relative to the observed ones, over the experimental reciprocal space for X-ray diffraction patterns recorded at (a) 0.3 GPa and (b) 21.8 GPa. Dotted lines mark the ±10% error range were the majority of reflections are found.

Point Label	Single or Set of Completely Overlapping X-ray Diffraction Lines
1	(330) **(411)**
2	**(730)**
3	(811) (554) (741)
4	(930) (851) **(754)**
5	(930) **(851)** (754)
6	(942) (861) (10 1 0) **(764)**

Table 5.1. (hkl)'s for single or set of completely overlapping X-ray diffraction lines. (hkl)'s in bold represent the X-ray diffraction lines corresponding to the points labeled in Figure 5.18a.

Point Label	Single or Set of Completely Overlapping X-ray Diffraction Lines
1	**(430)**
2	**(541)**
3	**(540) (621)**
4	(710) (543) **(550)**
5	**(810)** (652) (740)
6	**(762)** (843) (850)

Table 5.2. (hkl)'s for single or set of completely overlapping X-ray diffraction lines. The bold (hkl)'s represent the diffraction lines corresponding to the points labeled in Figure 5.18b.

As it can be observed in Tables 5.1 and 5.2, with 3 exceptions, all reflections for which the MEM calculated structure factors show large deviations with respect to the observed value, are part of completely overlapping sets of reflections. Moreover, all reflections carrying the large errors have very weak intensities (small structure factors). These facts can lead to the conclusion that the large discrepancies between the MEM calculated and the observed structure factors are not necessary due to errors in the MEM calculation procedure, but, more probably, due to incorrect estimation of the "observed" structure factors by MPF.

In the following, the influence of the peaks listed in Table 5.2, having MEM calculated structure factors very different than the observed ones, on the charge density distribution is tested. For this purpose, charge density distribution is derived using a set of structure data from which the reflections carrying large errors are excluded. Figures 5.19, 5.20, and 5.21 present the charge density distributions maps obtained from the incomplete (a) and complete (b) set of structure factors in (100), (200), and (110) planes, respectively. No significant differences, relevant for our discussion on changes induced by pressure in Ba_8Si_{46} electron density distribution, can be observed.

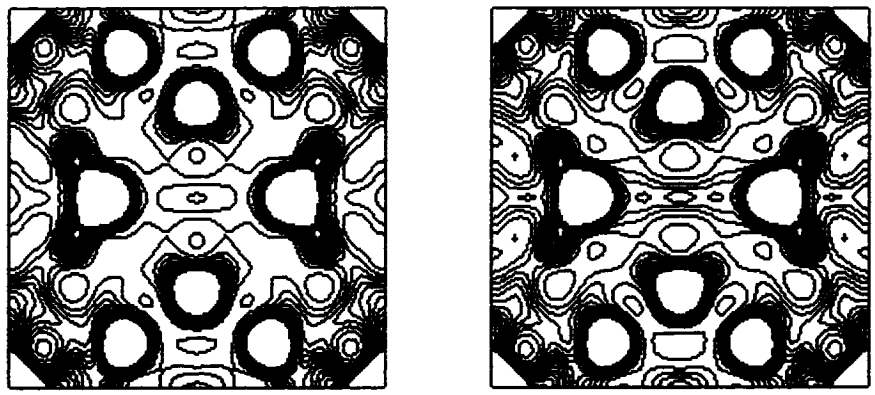

Figure 5.19. Contour plots of the electron density in the (100) plane at 21.8 GPa, calculated using the complete (a) and incomplete (b) sets of structure factors. Contour lines are drawn from 0.06 to 2.00 *e*/ Å^3 at intervals of 0.10 *e*/ Å^3.

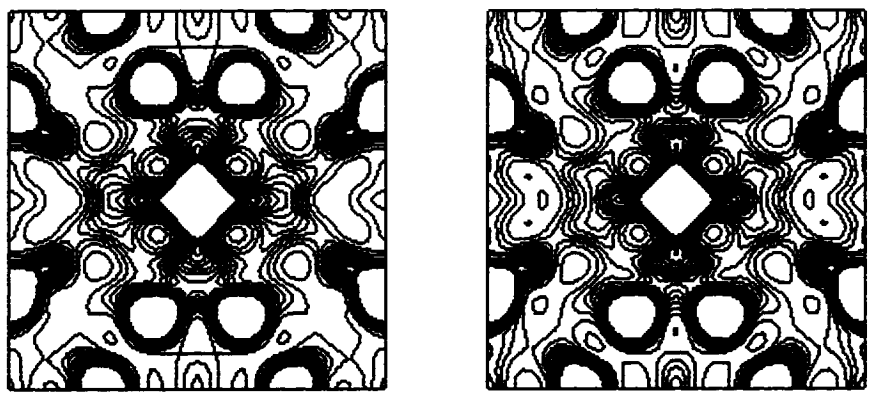

Figure 5.20. Contour plots of the electron density in the (200) plane at 21.8 GPa, calculated using the complete (a) and incomplete (b) sets of structure factors. Contour lines are drawn from 0.06 to 2.00 *e*/ Å^3 at intervals of 0.10 *e*/ Å^3

The difference charge density distribution ($\rho_{complete}$-$\rho_{incomplete}$) was calculated for an accurate evaluation of the differences between the two MEM results (Figure 5.22).

Figure 5.21. Contour plots of the electron density in the (110) plane at 21.8 GPa, calculated using the complete (a) and incomplete (b) sets of structure factors. Contour lines are drawn from 0.06 to 2.00 *e*/ Å^3 at intervals of 0.10 *e*/ Å^3

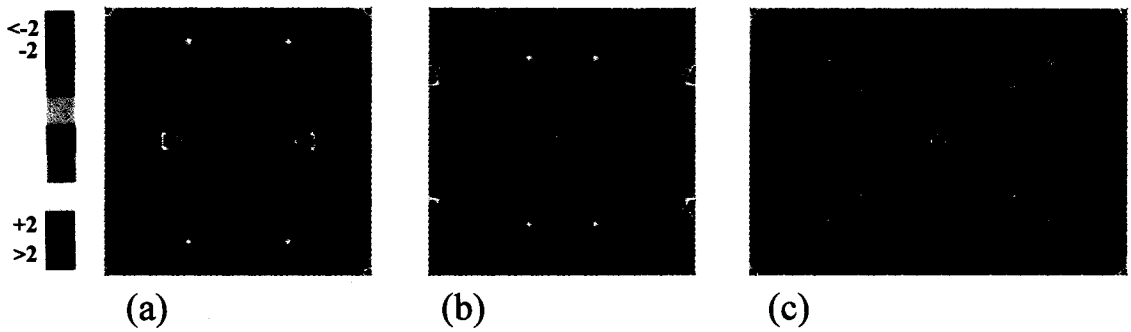

Figure 5.22. Difference charge density distribution contour plots in the (100) (a), (200) (b), and (110) (c) planes. Contour lines are drawn from –2.00 to 2.00 *e*/ Å^3 at intervals of 0.10 *e*/ Å^3

The largest difference between the electron density distributions derived using the complete and an incomplete set of structure factors is +10.4 $e/Å^3$, and can be observed in the core region of the Ba atom (calculated density 555.4 $e/Å^3$). The examination of the difference charge density distribution maps shown in Figure 5.22 reveals the small influence that the diffraction lines listed in Table 5.2 have on the MEM calculated charge density distribution.

5.7 Summary and Conclusions

Rietveld analysis of X-ray diffraction patterns of type-I Ba_8Si_{46} clathrate recorded at pressures increasing from 0.3 to 26 GPa was pursued for the purpose of studying structural changes induced by pressure. The unit cell volume showed a sudden and significant decrease at about 17 GPa. Furthermore, no changes were found in the system symmetry or in the atom positions. All these results are in very good agreement with the previous reports [9-11].

To get more insights on the structural changes that Ba_8Si_{46} undergoes with pressure, electron density distribution maps were derived from MEM analysis and closely examined. It has been concluded that their variations with pressure are in relation to structural transitions reported in the three earlier studies mentioned before. The explanation proposed for the low pressure transition (around 7 GPa), that this is the result of charge transfer from Ba atoms to Si framework, is in good agreement with the observations from the EXAFS and Raman studies. As for the high pressure transition (16-17 GPa), the direct analysis of experimental electron density distributions indicates that the observed volume collapse is driven by a sudden change in the electron density topology due to a substantial rearrangement of the distribution of the valence electrons. The mechanism for this transition may be classified as a special case of the more general electron topological transition (ETT) [24]. An ETT transition is often referred to as the change in the topology of the Fermi surface due to changes in the occupations of the

filled and empty bands at the vicinity of the Fermi level without a structural transformation. The observed redistribution of the electron density is consistent with the trend in the variation of the atomic thermal parameters with pressure reported recently [10].

To evaluate the reliability of the calculated charge density distributions, the differences between the MEM calculated structure factors and the observed structure factors extracted from the X-ray diffraction data using MPF were analyzed. The relative error of the MEM calculated structure factors, relative to the observed ones, was found to be less than 10%, with a few exceptions. Those exceptions proved not to influence significantly the final charge density distributions. Also, and very importantly, the errors were equally distributed over the reciprocal space in which the X-ray diffraction data were collected.

The Rietveld/Maximum Entropy analysis reported in this chapter is not only important in the specific case of Ba_8Si_{46} clathrate, but also in the much broader field of structural characterization of materials subject to high pressure. This is, to our knowledge, the first reported study of structural changes and phase transitions in dense materials based on Rietveld/MEM. Its success in detecting and characterizing even very subtle structural transitions, for instance ETT transitions, proves the method to be a potentially very important tool for analysis of diffraction data (both neutron and X-ray) recorded at high pressures. Moreover, our successful high pressure X-ray diffraction study of sI xenon and krypton hydrates by MEM, presented in Chapter IV, supports this conclusion.

References

1. J. S. Kasper, P Hagenmüller, M. Pouchard, and C. Cros, Science **150**, 1713 (1965).
2. E. Reny, S. Yamanaka, C. Cros, and M. Pouchard, Chem. Commun. **2000**, 2505 (2000).

3. J. L. Cohn, G.S. Nolas, V. Fessatidis, T.H. Metcalf, and G.A. Slack, *Phys. Rev. Lett.* **82**, 779 (1995).
4. J. S. Tse, K. Uehara, R. Rousseau, A. Ker, C. I. Ratcliffe, M. A. White and G. MacKay *Phys. Rev. Lett.* **85**, 114 (2000).
5. J. Gryko, P. F. McMillan, R. F. Marzke, G. K. Ramachandran, D. Patton, S. K. Deb, and O.F. Sankey, *Phys. Rev.* B **62**, 7707 (2000).
6. D. Connetable, V. Timoshevskii, E. Artacho, and X. Blase, *Phys. Rev. Lett.* **87**, 206405 (2001).
7. H. Kawaji, H. Horie, S. Yamanaka, and M. Ishikawa, *Phys. Rev. Lett.* **74**, 1427 (1995).
8. S. Yamanaka, E. Enishi, H. Fukuoka, and M. Yasukawa, *Inorg. Chem.* **39**, 56 (2000).
9. A. San Miguel, A. Merlen, P. Toulemonde, T. Kume, S. Le Floch, A. Aouizerat, S. Paskarelli, G. Aquilanti, O. Mathon, T. Le Bihan, J.P. Itié, S. Yamanaka, *Europhys. Lett.* **69**, 556 (2005).
10. L. Yang, Y. M. Ma, T. Iitaka, J. S. Tse, K. Stahl, Y. Ohishi, Y. Wang, R. W. Zhang, J.F. Liu, H.-K. Mao and J. Z. Jiang, *Phys. Rev. B* **74**, 245209 (2006).
11. T. Kume, H. Fukuoka, T. Koda, S. Sasaki, H. Shimizu, and S. Yamanaka., *Phys. Rev. Lett.* **90**, 155503 (2003).
12. F. Izumi and T. Ikeda, *Mater. Sci. Forum* **321-324,** 198 (2000).
13. J. P. Poirier, *Introduction to the Physics of the Earth's Interior* (Cambridge University Press, 1991).
14. J. S. Tse, S. Desgreniers, Z. Q. Li, M. R. Ferguson, and Y. Kawazoe, *Phys. Rev. Lett.* **89**, 195507 (2002).
15. F. Izumi and R. A. Dilanian, "Recent Research Developments in Physics," **3**, Part II, *Transworld Research Network*, Trivandrum, 699 (2002).
16. Y. Shimizu and H. Tanaka, *private communication.*
17. S. Saito and A. Oshuyama, *Phys. Rev. B* **51**, 2628 (1995).
18. K. Moriguchi, M. Yonemura, A. Shintani and S. Yamanaka, *Phys. Rev. B* **61**, 9859 (2000).

19. J. S. Tse, T. Iitaka, T. Kume, H. Shimizu, K. Parlinski, H. Fukuoka and S. Yamanaka, *Phys. Rev.* B **72**, 155441 (2005).
20. J. S. Tse, *Z. Krist.* **220**, 521 (2005).
21. M. Takata and M. Sakata, *Acta Cryst.* A **52**, 287 (1996).
22. L. Dobrzynski and J. Waliszewski, *J. Phys. Soc. Japan* **72**, 2203 (2003).
23. M. Merli and A. Pavese, *Z. Kristallogr.* **221**, 613 (2006).
24. I. M. Lifshitz, *Sov. Phys. JETP* **11**, 1130 (1960).

Summary and Outlook

In the present work, changes induced by pressure in the structural parameters and charge density distributions of two classes of materials, crystallizing in similar structure, namely gas clathrate hydrates and silicon clathrates, were investigated by means of powder X-ray diffraction. All experiments were carried out using synchrotron radiation and at room temperature. The experimental data were analyzed in detail using the Rietveld method for structure refinements and determination of precise structural parameters, and the recently developed Rietveld/MEM method for reconstructing charge density distributions from X-ray diffraction data.

A detailed high pressure study of structural properties and charge density topology of dense sI xenon and krypton clathrate hydrates has been presented in Chapter IV. At first, the sequence of phase transitions that both compounds undergo with pressure was investigated. For the case of Xe hydrate, sI was observed at the lowest pressure in the experiment, 0.16 GPa, and it remained stable up to 1.98 GPa, when X-ray diffraction lines arising from the sH phase started to develop. In contrast with Xe hydrate, the sII phase was found to form at low pressures (0.05 GPa) in the case of Kr hydrate. Two other phases, sI (up to 0.58 GPa) and sH (0.74 GPa) were observed as the pressure increased. Our findings are in agreement with previously reported studies.

Then, we focused on a detailed study of sI Xe and Kr under high pressure conditions, as this a common phase for both hydrates analyzed in this study and high quality experimental X-ray diffraction data were available. The Rietveld analysis revealed consistent changes in the lattice parameter and cage geometry of sI Xe hydrate, as pressure increased. An increasing trend was observed in the relative atom position of O*(16i)*, leading to a substantial decrease of the O*(16i)*-O*(16i)* bond length. On the other hand, no significant changes were determined for the atom position of O*(6c)* and O*(24k)*. The largest changes in the cage geometry were observed in the case of the large cages,

partially formed by O*(16i)*-O*(16i)* bond. This led us to the conclusion that the framework of small cages is less affected by pressure than that of the large cages. As the 5^{12} cavity (referred to as the "small cage" of sI) is common to all three high pressure phases presented in this thesis, our finding is not unexpected. No significant changes were found in the cage geometry or atom positions in the case of Kr hydrate, probably due to the small pressure range over which the X-ray diffraction data were collected for structure I.

The examination of the MEM derived charge density distributions for all pressure points available, in both Xe and Kr hydrates, confirmed the structural changes assessed from Rietveld refinements. Moreover, it gave us access to important information regarding the behavior of the guest atoms: spherical charge density distributions were found for both Xe and Kr atoms in the small cages, while significant distortions from the spherical symmetry, interpreted as preferential direction of thermal vibration, were observed for guest atoms of the large cages. Based on those observations, we advanced the idea that the phase transition to the next denser phase, structure H, is induced by the combined effect of decreasing cage dimensions, with the increasing pressure, and large translational vibrations of the guest atoms encaged in the large cavities.

The iterative Rietveld/MEM method was also applied to the case of dense Ba_8Si_{46} clathrate, which is structurally similar to sI gas clathrate hydrates. The most probable electron density distributions were derived from X-ray diffraction data collected in the 0.3 to 25.8 GPa pressure range, with the goal to study the structural transformations induced by pressure in Ba_8Si_{46}, as reflected in the changes of the electron distribution topology. Our study was motivated by previous X-ray diffraction, Raman, and EXAFS studies which reported the occurrence of two iso-structural phase transitions, around 5 and 16 GPa, but could not fully explain the origin of those transitions. The detailed examination of the MEM calculated charge density distributions allowed us to propose plausible transition mechanisms, in agreement with all previously reported observations: the low pressure transition was considered to be the result of an enhanced charge transfer from the guest Ba atoms to the Si framework. As for the high pressure transition, it was observed that the valence electrons of the Si atoms, initially forming strong σ-covalent bonds at low pressure, were becoming delocalized, weakening the Si-Si bonds, which

resulted in a sudden collapse of the unit cell volume. Significant distortions from the spherical distribution were also observed for the Ba atoms charge density distribution at pressure above 17 GPa, leading to the conclusion that high pressure phase transition observed in Ba_8Si_{46} can be characterized as an ETT transition.

The study of structural transformations in dense Ba_8Si_{46} clathrate is, to our knowledge, the first reported study of pressure-induced structural phase transitions by means of Rietveld/MEM analysis of X-ray diffraction data. It proves the ability of this method to extract the maximum amount of information from experimental powder X-ray diffraction data, and it shows its potential to detect and characterize very subtle structural changes in dense compounds. As was previously described, we have successfully applied this method in another high pressure study, i.e., on sI Xe and Kr clathrates.

Outlook

In order to achieve a broader view of the interactions between the guest atoms/molecules and the water framework in the dense phases of gas clathrate hydrates, further experimental and computational efforts are required for detailed studies of structural and lattice dynamical properties, along with charge density topology, for each high-pressure phase. Such studies can also address unanswered points regarding phase stability conditions related to the size of the guest species in dense structures and pressure induced transition mechanisms.

Although we consider our study on dense sI Xe and Kr hydrates as a significant step forward in understanding guest-host coupling mechanisms and the influence of pressure on the structural characteristics of this phase, further experimental and theoretical studies would be needed to confirm our findings. Single crystal diffraction experiments would be needed to obtain accurate information regarding changes in oxygen atom positions and cage occupancies. Also, neutron diffraction experiments would be the proper experimental method to probe the influence of increasing pressure on the H-H and H-O bonds forming the cage frameworks.

More detailed theoretical studies would be needed to validate our observations and conclusions presented in the electron density topology study of dense Ba_8Si_{46}.

Further, more in-depth analyses of the errors associated with the charge density distribution maps derived using the Rietveld/MEM method should be carried out for the case of imperfect X-ray diffraction datasets (as are those obtained from experiments). A systematic study of the influence of the "cut-off" in the *d*-spacing range of X-ray diffraction peaks on the calculated charge density distribution, along with an estimation of the way the quality of X-ray diffraction pattern is reflected in the accuracy of the derived distributions, would be needed.